Mission Design and Trajectory Analysis for Inspection of a Host Spacecraft by a Microsatellite

by

Susan C. Kim
S.B., Aerospace Engineering
Massachusetts Institute of Technology (2002)

Submitted to the Department of Aeronautics and Astronautics
in partial fulfillment of the requirements for the degree of
Master of Science in Aeronautics and Astronautics
at the
MASSACHUSETTS INSTITUTE OF TECHNOLOGY
June 2006

Author .....
Department of Aeronautics and Astronautics
May 26, 2006

Certified by .....
Stanley W. Shepperd
Principal Member of the Technical Staff
The Charles Stark Draper Laboratory, Inc.
Thesis Supervisor

Certified by .....
David W. Miller
Professor of Aeronautics and Astronautics
Thesis Advisor

Accepted by .....
Jaime Peraire
Professor of Aeronautics and Astronautics
Chair, Committee on Graduate Students

Mission Design and Trajectory Analysis for Inspection of a Host Spacecraft by a Microsatellite

by

Susan C. Kim

Submitted to the Department of Aeronautics and Astronautics
on May 26, 2006, in partial fulfillment of the
requirements for the degree of
Master of Science in Aeronautics and Astronautics

Abstract

The trajectory analysis and mission design for inspection of a host spacecraft by a microsatellite is motivated by the current developments in designing and building prototypes of a microsatellite inspector vehicle. Two different mission scenarios are covered in this thesis – a host spacecraft in orbit about Earth and in deep space. Some of the key factors that affect the design of an inspection mission are presented and discussed. For the Earth orbiting case, the range of available trajectories – natural and forced – is analyzed using the solution to the Clohessy-Wiltshire (CW) differential equations. Utilizing the natural dynamics for inspection minimizes fuel costs, while still providing excellent opportunities to inspect and image the surface of the host spacecraft. The accessible natural motions are compiled to form a toolset, which may be employed in planning an inspection mission. A baseline mission concept for a microsatellite inspector is presented in this thesis. The mission is composed of four primary modes: deployment mode, global inspection mode, point inspection mode, and disposal mode. Some figures of merit that may be used to rate the success of the inspection mission are also presented. A simulation of the baseline mission concept for the Earth orbiting scenario is developed from the trajectory toolset. The hardware simulation is based on the current microinspector hardware developments at the Jet Propulsion Laboratory. Through the figures of merit, the quality of the inspection mission is shown to be excellent, when the natural dynamics are utilized for trajectory design. The baseline inspection mission is also extended to the deep space case.

Thesis Supervisor: Stanley W. Shepperd
Title: Principal Member of the Technical Staff
The Charles Stark Draper Laboratory, Inc.

Thesis Advisor: David W. Miller
Title: Professor of Aeronautics and Astronautics

Acknowledgments

Had it not been for the support of the Charles Stark Draper Laboratory (CSDL) and the Jet Propulsion Laboratory (JPL), this thesis would not have been possible. First, I would like to thank Stan Shepperd, for his willingness to spend valuable time as my thesis supervisor, as well as being a great mentor and friend. I thank Lee Norris for all the guidance, support, and advice he has provided during my Draper fellowship. I also thank Linda R. Fuhrman, who alerted me to this research opportunity and gave me a running start with her input and advice. Hannah Goldberg at JPL was a valuable source of information and technical advice. I thank her for her guidance throughout the research process and for her dedication in providing me with answers to all my questions. I would also like to thank Professor David Miller for his counseling during my undergraduate years, as well as being an excellent faculty and thesis advisor during my graduate years.

Finally, I would like to thank my family. I thank my loving parents and sister, who have been sources of inspiration and pride all my life. I thank my husband for his wide-ranging expertise, love, support, and patience. I would not have been able to accomplish this work without the support of my family.

This research was carried out at the Charles Stark Draper Laboratory for the Jet Propulsion Laboratory, California Institute of Technology, under a contract with the National Aeronautics and Space Administration and funded through the Director's Research and Development Fund program.

Publication of this thesis does not constitute approval by Draper or the sponsoring agency of the findings or conclusions contained herein. It is published for the exchange and stimulation of ideas.

5/26/2006

Susan C. Kim Date

(This Page Intentionally Left Blank)

Contents

List of Figures

List of Tables

(This Page Intentionally Left Blank)

Chapter 1

Introduction

Since the inception of the space age, there have been considerable advancements to the design, reliability, and fault management of a space vehicle. However, to this day, ground operators still lack an inexpensive method of visually observing on-orbit spacecraft operations in real-time. This is a problem that has been amplified with losses such as that of the Space Shuttle, Columbia, which might have been preventable, had it been possible to inspect the surface thoroughly before re-entry.

Due to the improvements in the miniaturization of spacecraft components in recent years, microsatellites on the order of $100\,kg$ and under have become increasingly popular [1]. Lately, there has been interest in a cost-effective, small-mass ($< 10\,kg$), and deployable microsatellite inspector (or microinspector), as a viable solution for visually inspecting a host spacecraft. The microsatellite inspector could be launched attached to the host spacecraft and released to observe instrument deployments, examine possible mechanical malfunctions, or look for physical damage on the host. The maneuvers, during the inspection process, can either be accomplished autonomously or under human supervision. At end of the inspection, the microsatellite would then retreat to an area safe from damaging the host, either maneuvering to a dock or being disposed of in a safe orbit, depending on the design. Macke et al. points out that "inspection" suggests a range of external observations, such as visual inspection for damage or creating field maps of the host vehicle's RF, magnetic or nuclear emissions [2]. Further potential applications include aiding deployment or monitoring the

environment of the host vehicle to provide space situational awareness [3].

Such a vehicle has applicability to an extensive range of host vehicle types. A microsatellite inspector could externally inspect manned space vehicles, such as the Space Shuttle, International Space Station (ISS), or the Crew Exploration Vehicle (CEV) for anomalies, minimizing the potential risks to human life on board. In addition, a microinspector could support unmanned spacecraft including commercial communications satellites, scientific satellites, and the deployment of solar sails on sailcrafts. Future space vehicles may include many inspector-like vehicles, throughout the lifetime of their missions, providing on-orbit management when needed.

Much of the published efforts exploring the microsatellite inspector concept have been on developing the spacecraft hardware. An analysis of the feasible trajectories would provide a valuable set of constraints and requirements on the hardware design of a microsatellite inspection vehicle. However, very little work has been conducted and released to the community examining this aspect of the microinspector. Therefore, the context of this thesis is to analyze trajectories and design a baseline mission concept for the visual inspection of a host spacecraft by a microsatellite inspector. The actual Guidance, Navigation, and Control (GN&C) of the microinspector are not considered.

1.1 Background

Recently, there have been a few successful demonstrations of inspector spacecraft technologies. In June 2000, the Surrey Space Centre (SSC) and Surrey Satellite Technology Limited (SSTL) launched a $6.5\,kg$ remote inspection demonstrator vehicle, SNAP-1 (Surrey Nanosatellite Applications Platform), with its companion microsatellite, Tsinghua-1, on a Cosmos launch. SNAP-1 achieved its primary mission objective of imaging Tsinghua-1, during the deployment phase of the launch [4, 5, 6, 7]. The Air Force Research Laboratory (AFRL) launched the $31\,kg$ microsatellite XSS-10 in January 2003 and succeeded in operating an autonomous inspection sequence and optical navigation [8, 9]. As a follow up, in April 2005, AFRL launched XSS-11

which is approximately $100\,kg$ in mass. Among the mission objectives of XSS-11 is a close-up inspection of satellites to prove inspection capability [10].

In light of these on-going achievements in inspector spacecraft related technologies, a number of microsatellite inspector design concepts are being developed. The Jet Propulsion Laboratory (JPL) has been developing a microsatellite inspector based around the miniaturization of sensors and highly efficient low power electronics [11]. The JPL design is an autonomous 3–5 kg vehicle powered by a solar array and guided by celestial navigation to extend operation beyond Earth orbit.

The first small inspection vehicle built specifically for human spaceflight was AERCam "Sprint." A $16\,kg$ flyer, the AERCam was remotely piloted during a December 1997 Shuttle flight experiment. As an enhancement to the AERCam, the Mini-AERcam (Miniature Autonomous Extravehicular Robotic Camera) is being developed at NASA Johnson Space Center (JSC). In addition to having less than 20 % of the Sprint volume, the Mini AERCAM will demonstrate expanded capabilities including automatic station-keeping and point-to-point maneuvering [1, 12].

AeroAstro is designing an autonomous microsatellite, which would function as a companion satellite to larger and more costly spacecraft. Potentially, this microsatellite will aid in on-orbit inspection and technology validation among many other roles [3].

At the university level, there have also been projects exploring the use of microsatellites for inspection. CUSat is a project that is currently being run by the Space Systems Laboratory at Cornell University. The ultimate goal of CUSat is to design and build an autonomous inspection satellite system, while demonstrating hardware and navigation technologies [13]. The Bandit is a prototype inspector spacecraft that was designed and built by researchers and students at Washington University in St. Louis. A general mission overview for the Bandit vehicle, which includes a docking phase, is provided in Ref. [14]. Some of the issues involved with a visual inspection mission are discussed in Ref. [2], also in the context of the Bandit.

Although there have not been many published studies on trajectory design specifically for microsatellite inspectors, the literature database abounds with studies on

optimal trajectory design given a set of constraints. For instance, Richards et al. shows how mixed-integer linear programming can be used to develop trajectories that account for collision and plume impingement avoidance [15]. Many of these published results are directly applicable to a microsatellite inspector, when trajectory designs are refined and optimized for implementation.

1.2 Motivation

Most of the current activities on inspection spacecrafts have focused on demonstrating visual inspection feasibility, autonomous maneuvering, and hardware development. Furthermore, current rendezvous and inspection spacecraft are being designed for Low Earth Orbit (LEO), where they utilize relative GPS for navigation. Although some work has been done on forming a preliminary mission concept by the Bandit team, there is a discernible need to analyze the key issues involving a general mission for visual inspection and the impact on the overall mission design [2, 14]. Some important problems to evaluate are collision avoidance, fuel and power expenditure, lighting, and image quality. Considering the numerous applications to various types of host spacecrafts and the different environmental conditions, a trajectory analysis for the design of a robust mission concept would be invaluable during the hardware and mission design process of a microinspector.

1.3 Scope

There are two types of missions that affect the dynamics of a microsatellite inspector operation: An orbiting mission (Earth, Mars, or other planet) where gravity plays a large part in orbital dynamics, and deep space in which the effects come primarily from the Sun. The scope of this thesis covers orbiting and deep space missions. The limited mass, power, and fuel for a microsatellite inspector suggest that an analysis be performed on the possible host-relative trajectories to ensure safe proximity operations while using minimal system resources.

The focus of this thesis is on trajectory planning for an inspection mission by a microsatellite inspector. Thus, the instruments employed for a detailed inspection will not be addressed, nor will exact methods for navigation and control be discussed.

Emphasis is placed on trajectory work utilizing natural trajectories to save propellant. For an orbiting mission, the well-known *inclined football* trajectory is explored for collision avoidance mitigation. The inclined football trajectory places the microinspector out of the orbital path of the host spacecraft, allowing it to be close enough to inspect, yet minimizing the risk of collision. In generating these trajectories, this thesis uses simplified avoidance constraints.

Trajectory analysis will be conducted using the *Clohessy-Wiltshire*, or *CW* equations, which proceed from a first-order linearization of the equations of motion [16]. In this study, all trajectory simulations of a microsatellite inspector are based on the solution to these equations. Utilizing the *CW* equations is not as accurate as numerically integrating the equations of motion. However, they are adequate for analyzing the relative motion of a secondary spacecraft about the primary orbiting spacecraft. Additionally, the solution is analytic and exact, whereas numerical integration of the nonlinear equations of motion is computationally costly and prone to numerical errors. The smaller the deviation from the host spacecraft — the point of linearization — the more accurate the *CW* equations become. Since the inspection process entails close proximity operations by the microinspector, using the *CW* equations to analyze the natural relative dynamics near the host is more than acceptable within the scope of this thesis.

There is also a need to define what figures of merit constitute a "meaningful" inspection. Obtaining good image quality and complete coverage is a necessity for a microinspector mission. This thesis shows the results of such an analysis and describes candidate figures of merit that may be used to evaluate a baseline mission concept.

Attitude control of the microsatellite inspector is beyond the scope of this study. The attitude motion of the microsatellite inspector is not explicitly simulated in this thesis. Though, the mission simulation is primarily 3DOF, the effects of attitude maneuvering are included in the fuel usage estimates. Fuel estimates for orbit main-

tenance due to disturbances such as atmospheric drag are also included.

The mission design includes the disposal of the microinspector at the end of the inspection mission. Docking will not be considered as an option for the vehicle, and as such, will not be addressed in this thesis.

Chapter 2 presents the specific microsatellite inspector problem that is addressed in this thesis. Also, some of the basic problems associated with designing trajectories for an inspection mission are introduced and discussed. Chapter 3 presents design strategies that are considered and used to create these trajectories and the inspection mission. Chapter 4 describes the various natural motion trajectories that are possible, which are used to create a baseline mission for a microsatellite inspector for an Earth orbiting case. The simulation results of this baseline mission and other mission scenarios are presented and analyzed in Chapter 5. Chapter 6 extends the problem of a microsatellite inspection mission to the deep space case. Finally, a conclusion of the problem analysis and future work based on this study are given in Chapter 7.

Chapter 2

Statement of Problem

The lack of a low-cost method of visually inspecting a spacecraft on-orbit has been an inconvenience to ground operators for decades. Only recently has there been a significant reduction in size and cost to spacecraft components to make the free-flying microsatellite inspector concept realizable. Due to the current developments in designing and building prototypes of a microsatellite inspector, interest has been expressed in designing a mission concept for inspection.

The objective of this thesis is to analyze the range of natural and forced trajectories that may be utilized to form a mission for a visual inspection vehicle, in the face of various constraints and conditions. A baseline mission concept for an orbiting mission and a deep space scenario will be presented based on the trajectory study. Two mission scenarios will be created and presented through simulations: a microinspector mission concept for an Earth orbiting host, and a deep space scenario, which will be considered in the context of forced motion only. In order to rate the quality of the inspection mission, some of the possible figures of merit are discussed. The general spacecraft configuration and requirements for the simulation will be based on current microinspector developments at JPL. In the simulation and results section, this thesis will include recommendations for a microinspector mission, mission performance criteria (both for Earth orbiting and deep space), and general hardware requirements.

2.1 JPL

JPL has been developing and evolving a microsatellite design for the purpose of remote vehicle inspection for a number of years. The mission design analysis is based on current work at JPL pertaining to the Microinspector project. In conjunction with JPL, a set of general specifications on the GN&C sensor performance and constraints (field of view, sun angle constraints, resolution, drift rates, etc.) have been determined for this study. JPL also provided leadership in selecting mission scenarios. The mission simulation for this thesis will be loosely based on JPL's hardware design for a microsatellite inspector, shown in Figure 2-1. As for the host spacecraft, the hardware specifications will proceed from the CEV.

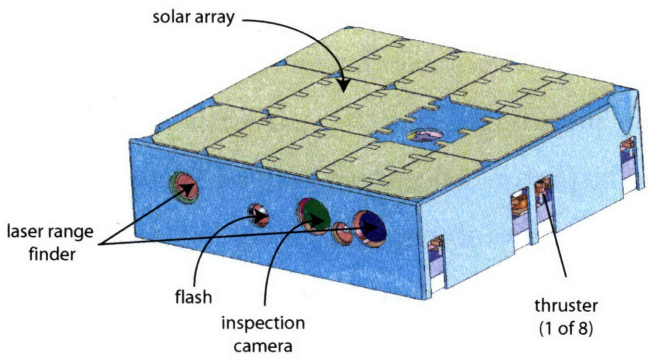

Figure 2-1: Microspacecraft Hardware Design by JPL

2.2 Requirements and Considerations

This section presents some of the mission and hardware requirements for a microsatellite inspector. The research, examples, and simulations in this thesis have been conducted with regards to the following requirements:

1. The following mission scenarios will be analyzed:
   (a) Earth orbiting
   (b) Deep space

2. For orbiting missions, mission design will primarily incorporate natural trajectory motion. Forced motion will only be used for loitering at some particular relative position.

3. Figures of merit for a visual inspection mission will be defined and used to identify mission success.

4. Based on the trajectory analysis, recommendations for a robust microinspector mission concept will be given.

5. Simulations of a baseline inspection mission will be developed and analyzed with the defined figures of merit.

6. Keep-out constraints will be utilized in generating trajectories. A $10\,m$ minimum distance constraint will be imposed in the simulations.

7. The host spacecraft has the following physical characteristics:

   - Dimension: length $= 30\,m$, diameter $= 5\,m$
   - Mass: $30\,t$

8. The microsatellite inspector has the following hardware, sensor, and actuator requirements for the simulation:

   - Dimension: $8\times8\times2\,in^3$
   - Mass: $3\,kg$
   - Sensors: Single camera (25° angle of view, 512 square pixel array), 2-axis sun sensor, 3-axis inertial measurement unit (IMU), star tracker, and laser range finder
   - Propulsion System: 8 cold-gas thrusters in pairs, each with a maximum thrust of $10\,mN$. The specific impulse is $I_{sp} = 50\,s$. The maximum total Δv available for trajectory (translational) and ACS (Attitude Control System) maneuvers is $15\,m/s$.

- Battery Power: The total capacity is $45\,W{\cdot}hr$. The average power consumption of the microinspector is $14\,W$.
- Solar Array: Produces $25\,W$ at $0°$ sun angle.

9. Image Requirements and Camera Specifications:

   - Resolution: $< 1\,cm$
   - 10 rows of pixel overlap between consecutive images
   - Pixel smear: < 1 pixel

There are several issues that must be taken into consideration when formulating a mission concept for the microinspector. The key issues associated with close proximity operations about the host are primarily collision avoidance and plume impingement by the microinspector. For near-circular orbiting missions, the natural dynamics of a secondary vehicle relative to the host vehicle are described by the *CW* equations. A detailed discussion of the *CW* equations and its analytic solution will be given in Section 3.1. Trajectories that take advantage of the natural motion can be designed using this analytic solution. Knowledge of generalized avoidance constraints can easily be incorporated into trajectory designs. Section 3.2 discusses the types of avoidance constraints.

Another important issue is imaging the host in natural lighting conditions. Without active cooperation of the host vehicle, complete coverage of the surface may be impossible, depending on the host's orientation and orbit. The light from the Sun may not be sufficient enough for image capture, due to various reasons: an improper sun angle*, not being in line of sight with the Sun, or being in the planet's shadow. This problem is also present in the deep space mission scenario. However, an artificial light source or flash illuminator on the microsatellite inspector may mitigate these problems. Section 2.4 introduces and discusses the problem of lighting for orbiting missions.

*For the definition of *sun angle* used in this thesis, refer to Section 3.6

In LEO, the effect of atmospheric drag on spacecraft motion cannot be ignored. In the context of relative motion, only the differential drag needs to be considered. The effect of differential drag on the mission design for orbiting cases and the resolution to the problem will be further elaborated under Section 3.3.

If the main source of power is derived from solar energy, the microinspector will be required to reorient itself every so often throughout its mission, such that the solar arrays face the Sun. The frequency of these maneuvers and the impact on the overall mission must be evaluated when examining the possible mission concepts. Section 3.6 gives the reader a more detailed description of this problem.

In order to rate a particular visual inspection mission, a set of figures of merit have been selected to score the mission. In qualitative terms, it is desired to image the entirety of the host vehicle's surface at various angles. The image quality is also a key factor in determining the success of a visual inspection mission. The figures of merit used for the baseline mission in this thesis are presented in Section 3.7.

2.3 Constraints

The constraints imposed by the microinspector hardware and mission directly impact the trajectory design for a microsatellite inspection mission. This section introduces some of the up-front constraints that must be considered during the mission design phase.

2.3.1 Avoidance Constraints

Collision avoidance and circumventing plume impingement are crucial in designing trajectories for a mission concept that includes close proximity operations. As one of the most important challenges, collision avoidance will require the microinspector to have a model of the host vehicle residing on board for autonomous trajectory planning. With the host vehicle's cooperation, it may be possible to utilize the host's processors for more position feedback or intensive computations. Additionally, plumes from a cold-gas thruster can adversely affect the panels and instruments. By utiliz-

ing the natural *2×1 ellipse* or so-called *inclined football* trajectory during orbiting missions, the risk of collision and plume impingement can be minimized. This type of motion is predictable and well behaved, and thus is suitable for a microinspector mission. Figure 2-2 shows one possible relative trajectory about the host vehicle, which is represented by the cylinder at the origin. The *2×1 ellipse* description of this relative motion is derived from the size of the relative "orbit" about the host vehicle. Section 3.1 gives a detailed explanation of the *CW* equations and natural trajectories.

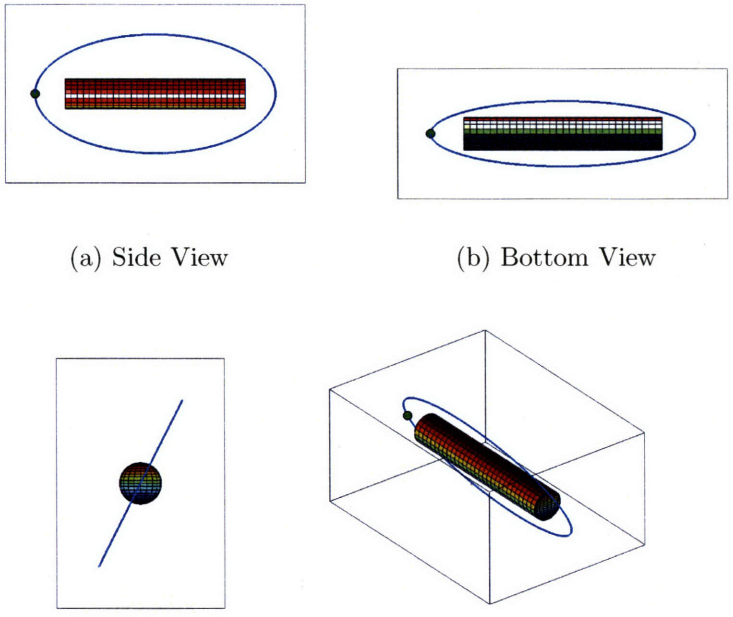

(a) Side View (b) Bottom View

(c) Front View (d) 3D View

Figure 2-2: Inclined 2×1 Elliptical Orbit

To further reduce the possibility of collision or plume impingement, it is necessary to have a *keep-out* constraint. This constraint describes a zone that encompasses the host spacecraft that cannot be impinged upon during the mission. The zone will act as a margin of error, during trajectory formation. It will account for the minimum allowable distance from the host surface due to plume impingement. The minimum distance requirement for the mission concept in this thesis is $10\,m$ from the surface of the host. The method used will be further elaborated in Section 3.2.

2.3.2 Fuel Constraints

A micropropulsion system that a microsatellite would operate on has limited fuel. There is very little margin to recover from mistakes that may danger the host mission. In this thesis, the fuel constraint imposed on the complete mission is a total Δv of 15 m/s. During the course of the mission, the Δv expended for each maneuver (translational and rotational) will be accumulated and used to rate the mission concept. The use of the CW solution to design trajectories will minimize the fuel expenditure for the mission, once again emphasizing the advantages of utilizing this analytic solution.

2.3.3 Time Constraints

Since a visual inspection by a microinspector is not considered to be time-critical, the CW solution is used in this thesis, to design the appropriate trajectories, without resorting to trajectory optimization methods. However, if ground operators foresee a need for time-minimal maneuvers, the forced motion method of generating trajectories can be employed with fuel penalty.

2.3.4 Camera and Image Constraints

The camera specifications and image requirements directly affect the trajectory planning process. For example, a maximum resolution for an image constrains the allowable distance of the microinspector from the host vehicle. The desired pixel smear determines the maximum velocity of the microinspector relative to the host. Also, there should be some pixel overlap between the images, to make sure the host surface is completely covered. It is apparent that these constraints and specifications must be accounted for in the mission planning.

2.4 Lighting

In order to obtain images of the host, present day methods require sufficient illumination. Utilizing the natural light from the Sun is preferred, since an artificial source of light would use up valuable energy resources. For an orbiting host mission, suitable lighting becomes a problem when the host vehicle is in the planet's shadow. If the surface being viewed is not appropriately illuminated, the camera on board the microinspector cannot take the image. Also, when the microinspector is in line of sight with the Sun, the sun angle becomes an issue when there are solar cells aboard, because of the rate of power consumption versus the rate of recharging. This section presents two simplified examples of Sun position vectors to illustrate the problems associated with lighting conditions. In both examples, the host vehicle is in a circular orbit about Earth, and rotating at the orbital rate, ω, in the inertial reference frame. Additionally, three different microinspector relative motions will be analyzed using the lighting conditions illustrated in the first example. For all examples, there will be a small box attached to the cylindrical host model to depict the orientation of the spacecraft. The inertial Sun direction can be assumed fixed, since the Sun motion is minimal during the time frame of an inspection mission. For the shadow analysis, the light rays from the Sun are assumed to be parallel, and the shadow forms a cylinder behind the Earth. Figure 2-3 illustrates this geometry of Earth's shadow.

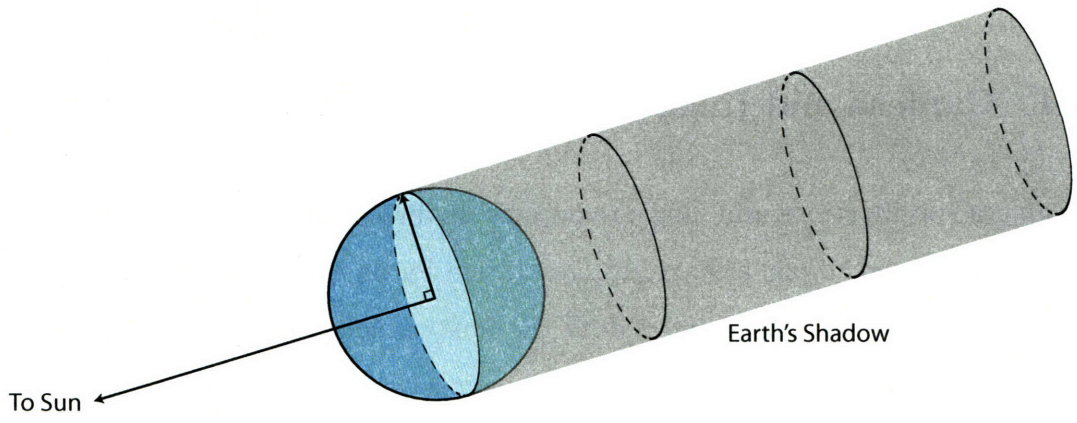

Figure 2-3: Earth's Shadow

Example 1, in Figure 2-4, portrays a case in which the Sun lies in the host vehicle orbital plane. For a portion of the host's orbit, the host will be in Earth's shadow. During this time, no part of the host's surface will be illuminated by sunlight and consequently, the microinspector cannot take images of the host vehicle without an artificial light source. For a circular orbit that is $500\,km$ above the surface of the Earth, the orbital period is about 95 minutes. If the Sun vector is oriented as in Example 1, the host vehicle will be in Earth's shadow for about 36 minutes, nearly a third of the time.

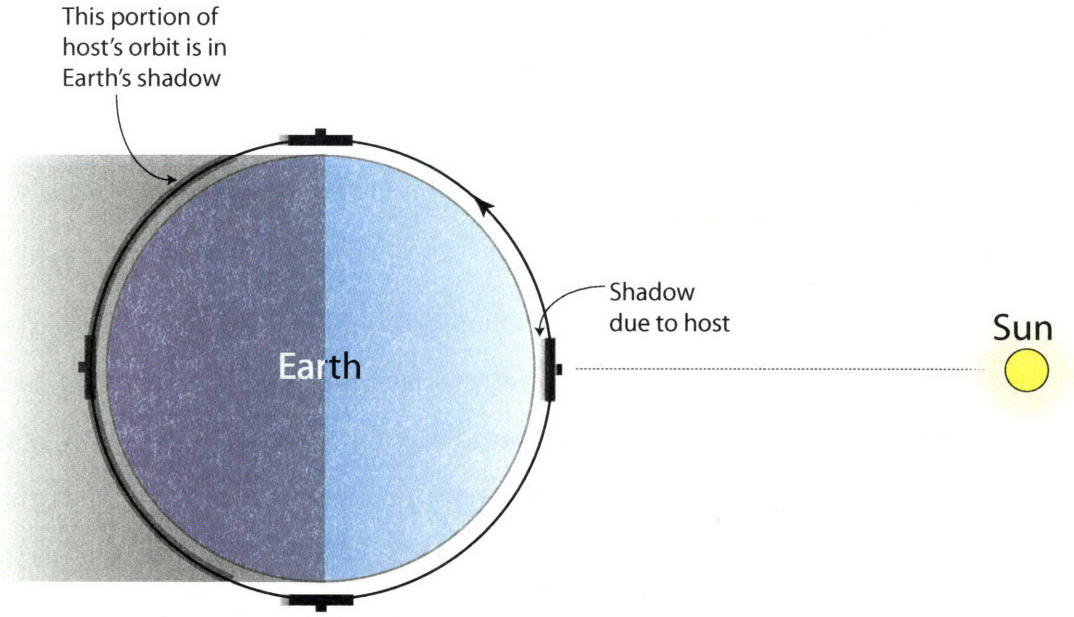

Figure 2-4: Lighting Example 1: The Sun is in the host vehicle orbital plane. The view is from above the orbital plane.

Example 2, shown in Figure 2-5, is a case in which the Sun is perpendicular to the orbit plane. In this case, the host vehicle always has line of sight to the Sun and is continuously illuminated. It should be pointed out that if not spinning, only one side of the host's surface is lit throughout the orbit. Therefore, the microinspector will not be able to take images of the opposite side using natural light. The view in Figure 2-5 is from the orbit's edge.

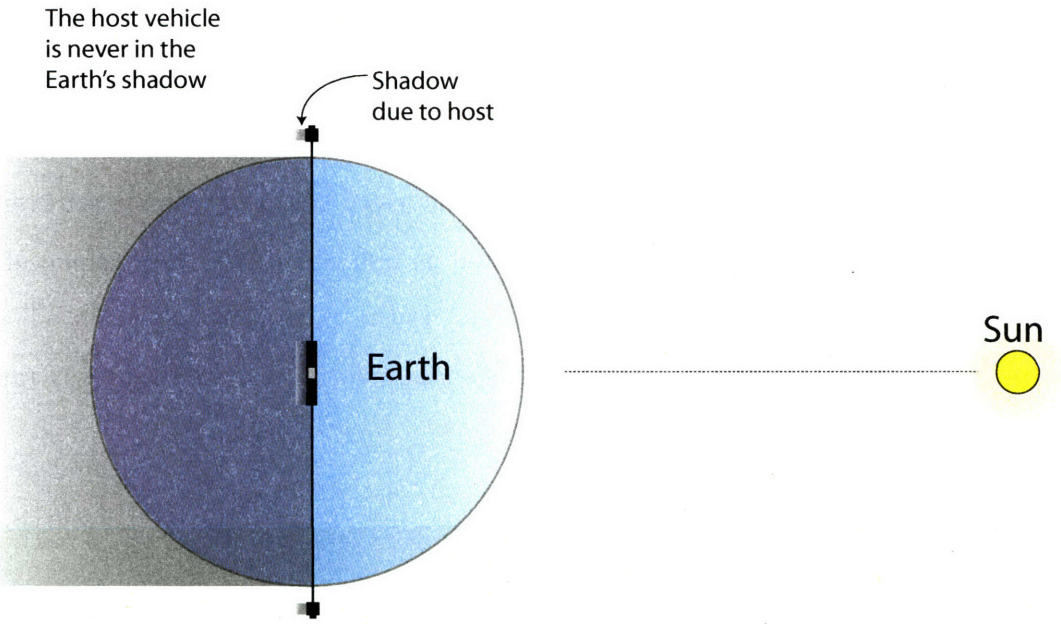

Figure 2-5: Lighting Example 2: The Sun is perpendicular to the host vehicle orbit plane. The view is edge on.

The next three cases demonstrate the difficulties encountered with lighting and utilizing natural relative motion to design trajectories for the microinspector mission concept. In all three cases, the geocentric Sun direction is in the host's orbit plane. The host vehicle is rotating in a circular orbit about Earth, and rotating at the orbital rate, ω, in the inertial reference frame as in Figure 2-4, maintaining a local-vertical local-horizontal (LVLH) attitude. Like the previous examples, the host vehicle needs to be sunlit. Beyond that, the point of interest must be illuminated and in the view of the microinspector, in order for image taking. Figure 2-6 illustrates an example, in which the image of the center segment can be captured. The segment is illuminated by sunlight and in the view of the camera on board the microinspector.

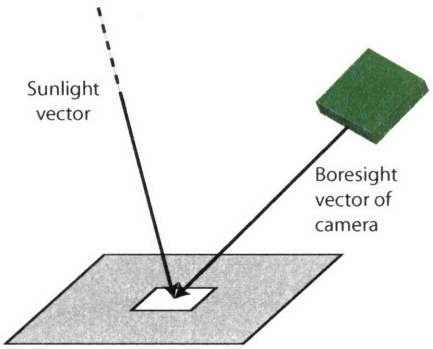

Figure 2-6: Lighting Condition and Camera View for Image Taking

As mentioned in Section 2.3, the 2×1 stationary ellipse is a possible relative trajectory for a microsatellite inspector about the host vehicle in an orbiting mission. The period of this relative motion is the same as the host vehicle's orbital period. The Sun is assumed to be in the host vehicle orbit plane in the following cases, as well as in the simulations. Figure 2-7a shows an in-plane 2×1 stationary ellipse in the relative frame of reference. In the relative reference frame, the $\hat{\boldsymbol{r}}$-axis lies along the radial vector and the $\hat{\boldsymbol{v}}$-axis lies along the velocity vector. Figure 2-7b depicts this type of motion in the geocentric inertial frame of reference, facing down on the orbital plane. The microinspector's orbit about the Earth is slightly eccentric, which causes the well known 2×1 ellipse in the relative reference frame. If the boresight vector does not rotate in the inertial reference frame, as in Figure 2-7b, it appears to rotate in the relative reference frame. The four numbered positions and boresight vector orientations defined in Figure 2-7a correlate with the four numbers in Figure 2-7b. As can be seen in this figure, apart from the time spent in Earth's shadow, the microinspector will always have sufficient light to acquire good images, since the angle between the sunlight vector and the boresight vector is 0° throughout the orbit. Besides the perfect lighting condition, the microinspector will have opportunities to take images of a large percentage of the host's surface. If, however, the microinspector was initially below the host vehicle at ① in Figure 2-7b, the lighting would never be acceptable for capturing photographs of the host vehicle. Hence, the importance of choosing the initial position and time on the relative natural trajectories is emphasized by this example.

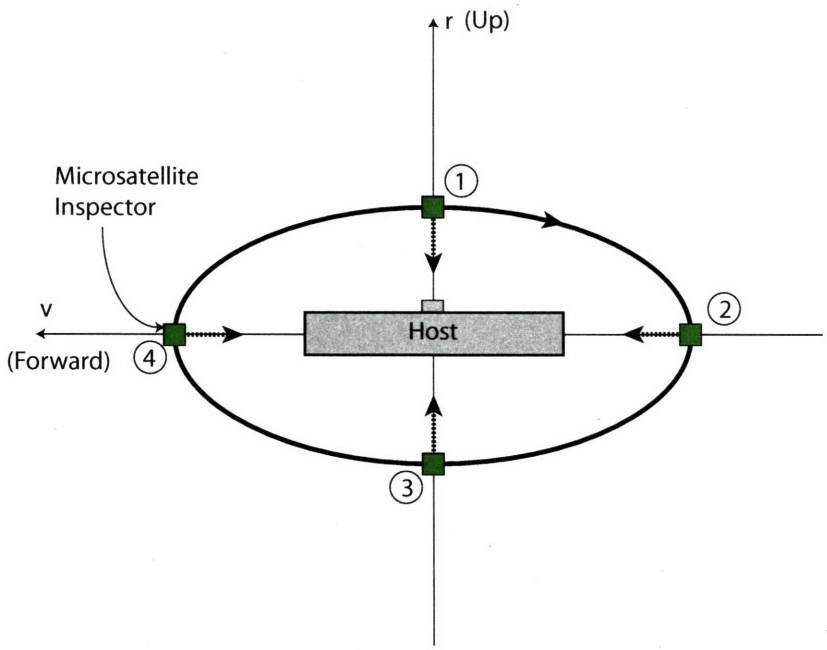

(a) In-plane 2×1 Stationary Ellipse in Relative Reference Frame

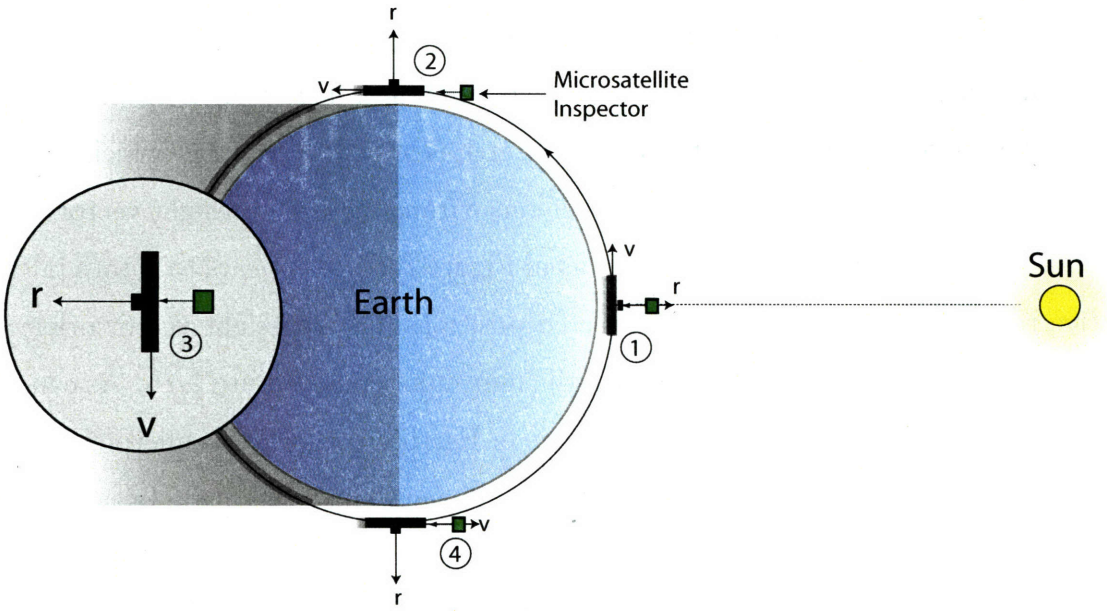

(b) In-plane 2×1 Stationary Ellipse in Geocentric Inertial Reference Frame

Figure 2-7: Lighting Case with Microinspector in In-plane 2×1 Stationary Ellipse: The Sun is in the host vehicle orbital plane. The camera's boresight vector does not rotate in the geocentric inertial reference frame.

Another possible case is illustrated in Figure 2-8. In this case, the microinspector is in the same orbit as the host vehicle, but closely behind the host, as shown in the geocentric inertial reference frame in Figure 2-8b. The view in this figure looks down on the orbital plane. In the relative reference frame, the microinspector appears to be stationary on the V-bar behind the host spacecraft vehicle, as displayed in Figure 2-8a. For this particular trajectory, the boresight vector is rotating at the orbital rate, ω, in the inertial reference frame. In the relative frame, the boresight vector is pointed toward the host vehicle and nearly parallel to the microinspector's velocity vector. The lighting condition is suitable for acquiring images for about one-third of the orbital period. In part, this is due to the time, in which the host vehicle is inside Earth's shadow. Even when the host vehicle is in line of sight with the Sun, the available time to take images is further reduced because there is not always enough sunlight illuminating the host's surface that is in the field of view of the camera. Positioning the microinspector on the V-bar and pointing the camera toward the host vehicle throughout the orbit allows images of the same point to be taken without expending any additional fuel, since the microinspector is spinning at a constant angular rate about the out-of-plane body-fixed axis.

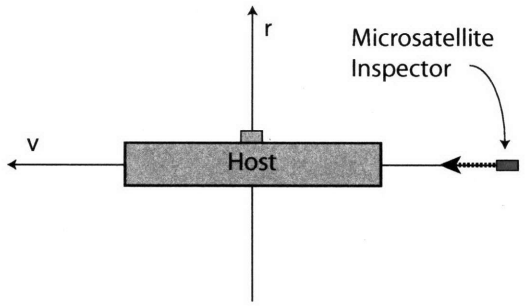

(a) Stationary on V-bar in Relative Reference Frame

Figure 2-8

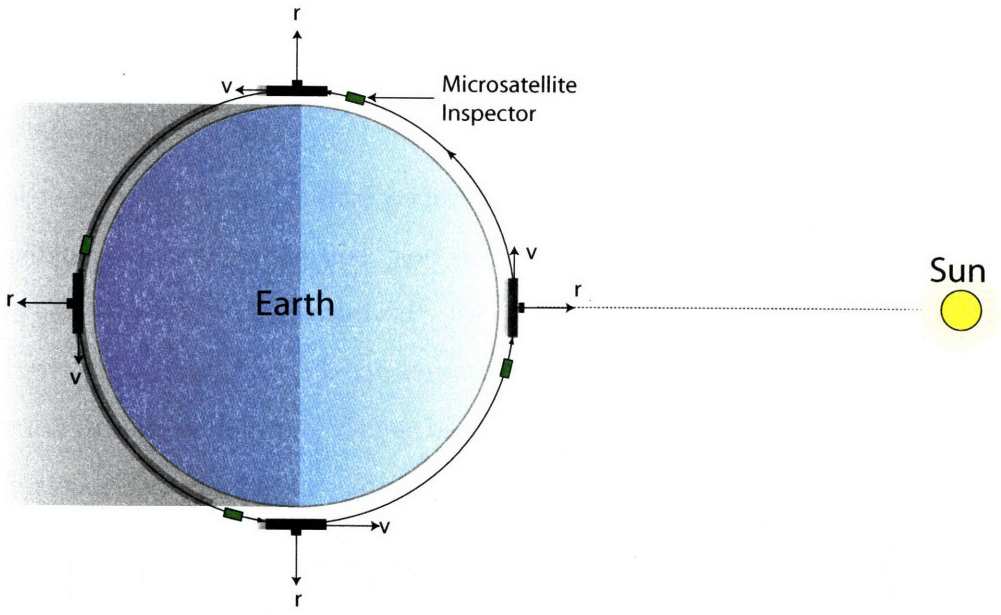

(b) Stationary on V-bar in Geocentric Inertial Reference Frame

Figure 2-8: Lighting Case with Microinspector Behind Host Vehicle: The Sun is in the host vehicle orbital plane. The camera's boresight vector rotates in the geocentric inertial reference frame at the orbital rate, ω.

The final example highlights a case where the microinspector travels in an out-of-plane 2×1 stationary ellipse about the host vehicle in the relative frame of reference. Figure 2-9a depicts this type of natural trajectory. The boresight vector is normal to the V-bar throughout the orbit. The four numbered positions and boresight orientations chosen in this figure correspond to the same numbers and boresight vector orientations in Figure 2-9b. As in the first case, the microinspector will have the chance to take images of various parts of the host's surface, with this lighting condition and choice of boresight vector orientations. Again, the importance of choosing the initial position and time carefully, in order to maximize the lighting advantages is highlighted here. Depending on the altitude of the host's orbit, there may not be enough sunlight when taking images of the bottom view of the host's surface.

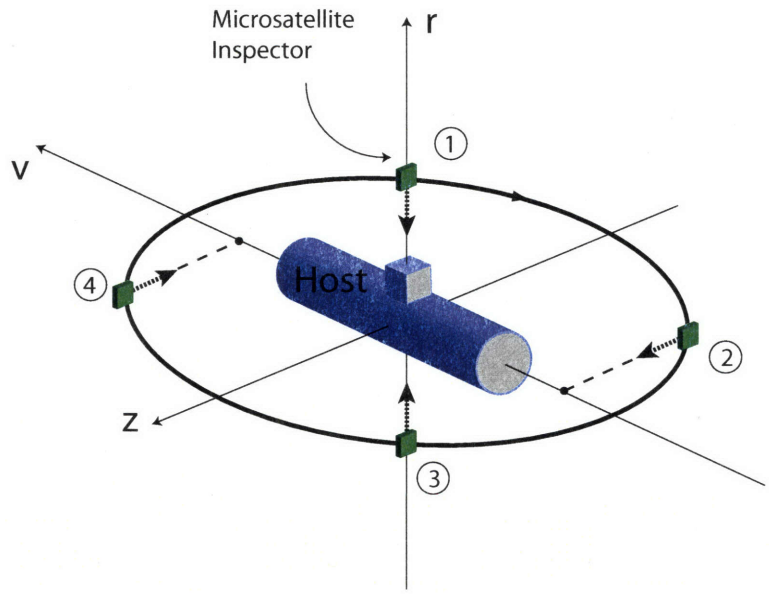

(a) Inclined 2×1 Stationary Ellipse in Relative Reference Frame

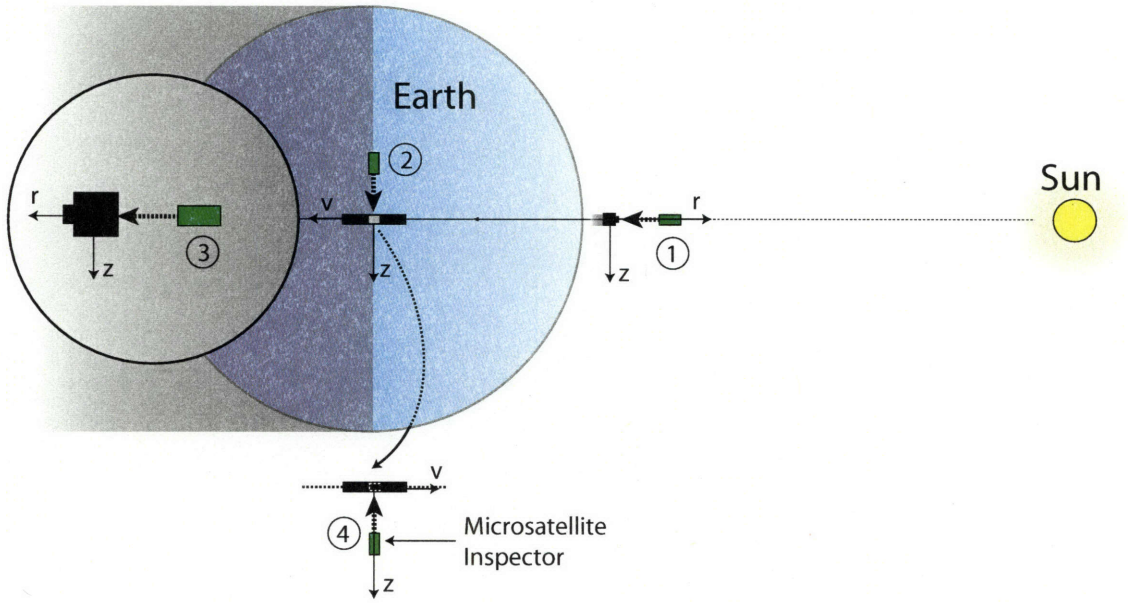

(b) Inclined 2×1 Stationary Ellipse in Geocentric Inertial Reference Frame

Figure 2-9: Lighting Case with Microinspector in Inclined 2×1 Stationary Ellipse: The Sun is in the host vehicle orbital plane. The camera's boresight vector rotates in the geocentric inertial reference frame.

For orbiting missions, the previous three cases underline the problems associated with using natural light from the Sun for capturing images using a microinspector. If the host vehicle is rotating at the orbital rate, ω, in the inertial reference frame as in the examples, there may be specific parts of the host's surface that can never be imaged, due to the Earth's shadow. In this situation, image capturing would be made possible by the host vehicle's cooperation or an artificial source of light. The three natural relative trajectories shown in the examples indicate that with careful choice of initial conditions, one can obtain sufficient lighting conditions for imaging much of the host's surface.

Chapter 3

Mission Design Strategy

This chapter highlights the strategies used to create the trajectories of a mission concept for a microsatellite inspector.

3.1 Natural Motion

The trajectory development for the microinspector mission concept will be based on the solution to the *Clohessy-Wiltshire* or *CW* equations, which are also known as the *Hill's* equations. These linearized differential equations describe the relative motion between two satellites that are in near-circular orbits about a planet and within a few kilometers of each other [17]. In Figure 3-1[†], the local-vertical rotating coordinate system (LVRCS) that is used for the *CW* solution is depicted. This coordinate system rotates at the orbital rate, ω. The position deviations ($\mathbf{x}$, $\mathbf{y}$, and $\mathbf{z}$) in this coordinate system denote the location of the secondary vehicle in the LVRCS with the target vehicle placed at the origin [18]. The positive y-axis is lined up with the V-bar – the velocity vector of the host spacecraft. The positive x-axis lies along the R-bar – the radial axis. The orbital position vector is depicted by $\boldsymbol{r}$.

[†]The image of Earth in Figure 3-1 was adapted from an online source, "3-D view of the Earth", http://atlas.geo.cornell.edu/people/weldon/earth-3d.gif, accessed 3/27/2006.

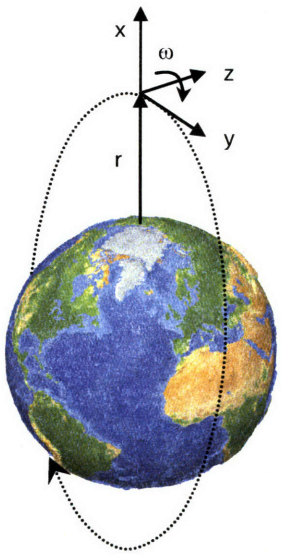

Figure 3-1: Local-vertical Rotating Coordinate System (*LVRCS*)

3.1.1 Clohessy-Wiltshire Equations

The *CW* differential equations are obtained by linearizing the orbital dynamics about a circular orbit. These equations, shown below, demonstrate the position deviation of the secondary vehicle from a nominally circular orbit, where d_x, d_y, d_z represent any disturbing accelerations in the LVRCS frame. It is important to note that this is a rotating frame of reference.

$$\ddot{x} - 2\omega\dot{y} - 3\omega^2 x = d_x \tag{3.1}$$

$$\ddot{y} + 2\omega\dot{x} = d_y \tag{3.2}$$

$$\ddot{z} + \omega^2 z = d_z \tag{3.3}$$

In this thesis, the host vehicle's orbit about Earth is assumed to be near-circular. The *CW* differential equations and their solution can thus be applied to describe the microsatellite inspector's motion about the host.

If the differential accelerations (d_x, d_y, d_z) are assumed to be constant, the solution to the *CW* differential equations are given by:

$$\begin{bmatrix} \boldsymbol{r}(t) \\ \boldsymbol{v}(t) \\ \boldsymbol{a}(t) \end{bmatrix} = \Phi(t_0, t) \begin{bmatrix} \boldsymbol{r}_0 \\ \boldsymbol{v}_0 \end{bmatrix} + A(t)\boldsymbol{d} \tag{3.4}$$

where,

$$\boldsymbol{r}(t) = \begin{bmatrix} x(t) \\ y(t) \\ z(t) \end{bmatrix} \text{ and } \boldsymbol{v}(t) = \begin{bmatrix} \dot{x}(t) \\ \dot{y}(t) \\ \dot{z}(t) \end{bmatrix} \text{ and } \boldsymbol{a}(t) = \begin{bmatrix} \ddot{x}(t) \\ \ddot{y}(t) \\ \ddot{z}(t) \end{bmatrix} \text{ and } \boldsymbol{d} = \begin{bmatrix} d_x \\ d_y \\ d_z \end{bmatrix} \tag{3.5}$$

$\begin{bmatrix} \boldsymbol{r}_0 \\ \boldsymbol{v}_0 \end{bmatrix}$ is the position and velocity at $t = t_0$.

$$\Phi(t_0, t) = \begin{bmatrix} 4 - 3\cos(\omega t) & 0 & 0 & \frac{\sin(\omega t)}{\omega} & \frac{2}{\omega} - \frac{2\cos(\omega t)}{\omega} & 0 \\ 6\sin(\omega t) - 6\omega t & 1 & 0 & \frac{2\cos(\omega t)}{\omega} - \frac{2}{\omega} & \frac{4\sin(\omega t)}{\omega} - 3t & 0 \\ 0 & 0 & \cos(\omega t) & 0 & 0 & \frac{\sin(\omega t)}{\omega} \\ 3\omega\sin(\omega t) & 0 & 0 & \cos(\omega t) & 2\sin(\omega t) & 0 \\ 6\omega\cos(\omega t) - 6\omega & 0 & 0 & -2\sin(\omega t) & 4\cos(\omega t) - 3 & 0 \\ 0 & 0 & -\omega\sin(\omega t) & 0 & 0 & \cos(\omega t) \\ 3\omega^2\cos(\omega t) & 0 & 0 & -\omega\sin(\omega t) & 2\omega\cos(\omega t) & 0 \\ -6\omega^2\sin(\omega t) & 0 & 0 & -2\omega\cos(\omega t) & -4\omega\sin(\omega t) & 0 \\ 0 & 0 & -\omega^2\cos(\omega t) & 0 & 0 & -\omega\sin(\omega t) \end{bmatrix} \tag{3.6}$$

$$A(t) = \left[\begin{array}{c} A_1(t) \\ \hline A_2(t) \\ \hline A_3(t) \end{array}\right] = \left[\begin{array}{ccc} \frac{1}{\omega^2} - \frac{\cos(\omega t)}{\omega^2} & \frac{2t}{\omega} - \frac{2\sin(\omega t)}{\omega^2} & 0 \\ \frac{2\sin(\omega t)}{\omega^2} - \frac{2t}{\omega} & -\frac{4\cos(\omega t)}{\omega^2} - \frac{3t^2}{2} + \frac{4}{\omega^2} & 0 \\ 0 & 0 & \frac{1}{\omega^2} - \frac{\cos(\omega t)}{\omega^2} \\ \hline \frac{\sin(\omega t)}{\omega} & -\frac{2\cos(\omega t)}{\omega} + \frac{2}{\omega} & 0 \\ \frac{2\cos(\omega t)}{\omega} - \frac{2}{\omega} & \frac{4\sin(\omega t)}{\omega} - 3t & 0 \\ 0 & 0 & \frac{\sin(\omega t)}{\omega} \\ \hline \cos(\omega t) & 2\sin(\omega t) & 0 \\ -2\sin(\omega t) & 4\cos(\omega t) - 3 & 0 \\ 0 & 0 & \cos(\omega t) \end{array}\right] \tag{3.7}$$

The out-of-plane (z) motion is completely decoupled from the in-plane (x,y) motion as can be attested by the solution in Eqn 3.6. The matrix $A(t)$ in Eqn 3.7 describes the motion of the secondary vehicle with respect to differential accelerations, such as atmospheric drag and thrust, assuming that the forces are modeled as constants. The secondary vehicle in this case would be the microsatellite inspector. Given the initial position and velocity of the microinspector, the *CW* solution characterizes the subsequent motion about the host vehicle in the LVRCF. The sinusoidal nature of the solution suggests that with the appropriate initial conditions, the microinspector can settle into a relative "orbit" around or near the host vehicle, without spending fuel on constant orbit maintenance. Fuel would only be expended at the beginning to insert the microinspector into the desired relative trajectory. Hence, it is desirable to exploit this quality of the natural dynamics, and use the *CW* solution during the mission design process. In addition, the operations of the microinspector that arise from an inspection mission will be in close proximity to the host vehicle, which validate the application of this analytic solution. Furthermore, utilizing the *CW* solution enormously simplifies the simulation of the mission concept, compared to numerically integrating the equations of motion.

3.1.2 Traveling Ellipse Formulation

The *CW* solution can also be written in a more intuitive form, known as the *traveling ellipse formulation* [18]. This form of the solution presents some advantageous geometric interpretations that facilitate trajectory design for the microinspector mission concept. The traveling ellipse form of the solution is as follows:

$$\boldsymbol{r}(t) = \begin{bmatrix} x(t) \\ y(t) \\ z(t) \end{bmatrix} = \begin{bmatrix} X_0 + b\sin(\omega t + \phi) \\ Y_0 - \frac{3}{2}\omega t X_0 + 2b\cos(\omega t + \phi) \\ c\sin(\omega t + \psi) \end{bmatrix} + A_1(t)\boldsymbol{d} \tag{3.8}$$

$$\boldsymbol{v}(t) = \begin{bmatrix} \dot{x}(t) \\ \dot{y}(t) \\ \dot{z}(t) \end{bmatrix} = \begin{bmatrix} b\omega\cos(\omega t + \phi) \\ -\frac{3}{2}\omega X_0 - 2b\omega\sin(\omega t + \phi) \\ c\omega\cos(\omega t + \psi) \end{bmatrix} + A_2(t)\boldsymbol{d} \tag{3.9}$$

$$\boldsymbol{a}(t) = \begin{bmatrix} \ddot{x}(t) \\ \ddot{y}(t) \\ \ddot{z}(t) \end{bmatrix} = \begin{bmatrix} -b\omega^2\sin(\omega t + \phi) \\ -2b\omega^2\cos(\omega t + \phi) \\ -c\omega^2\sin(\omega t + \psi) \end{bmatrix} + A_3(t)\boldsymbol{d} \tag{3.10}$$

where,

$$\begin{aligned} X_0 &= 4x_0 + \tfrac{2\dot{y}_0}{\omega} & Y_0 &= y_0 - \tfrac{2\dot{x}_0}{\omega} \\ \tfrac{\dot{x}_0}{\omega} &= b\cos(\phi) & -3x_0 - \tfrac{2\dot{y}_0}{\omega} &= b\sin(\phi) \\ z_0 &= c\sin(\psi) & \tfrac{\dot{z}_0}{\omega} &= c\cos(\psi) \end{aligned} \tag{3.11}$$

and $A_1(t)$, $A_2(t)$, and $A_3(t)$ are as before in Eqn 3.7.

The in-plane position equations in Eqn 3.8 imply that the state deviations trace out a 2×1 ellipse, with b as the semiminor axis if X_0 is zero. The semimajor axis of the ellipse is twice the length of b, hence the name given to the ellipse. In Eqn 3.11, the quantities b and c are parameters that describe the size; and, X_0 and Y_0 represent the center of the relative motion. The parameters ϕ and ψ are phase angles describing where the actual state is located. The values for these parameters can be obtained from the initial conditions, as shown in Eqn 3.11. The traveling ellipse parameters are detailed in Table 3.1 below.

Table 3.1: Traveling Ellipse Parameters

Parameter	Description
b	Semiminor axis on 2×1 ellipse in x-y plane (in-plane)
c	Magnitude of the simple oscillating out-of-plane motion
X_0	Denotes the deviation in the orbital semimajor axis (r); Ellipse moves forwards or backwards relative to the origin and depending on the sign
Y_0	Determines the location of the 2×1 ellipse along the trajectory
ϕ	Phase angle for the in-plane motion
ψ	Phase angle for the out-of-plane motion

Figure 3-2 illustrates some of the traveling ellipse parameters for an inclined 2×1 ellipse. The angle $\theta = \psi - \phi$ is constant for each stationary football orbit. For example, a relative trajectory with $\psi - \phi = 0°$ produces a relative orbit that intersects the V-bar. $\psi - \phi = 90°$ describes a relative orbit that intersects the R-bar. ψ describes the location where the inclined 2×1 ellipse intersects the in-plane.

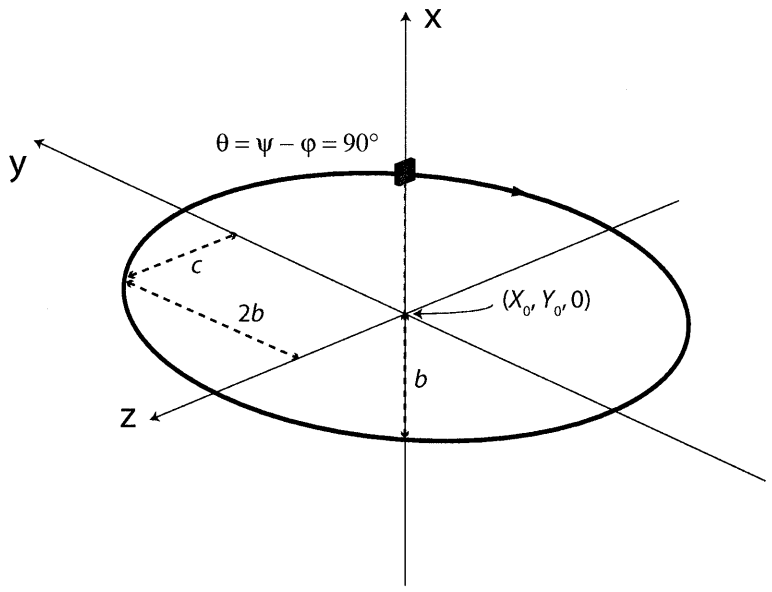

Figure 3-2: Traveling Ellipse Parameters

The secondary vehicle does not actually "orbit" the host vehicle, but the instantaneous parameters result in an elliptical orbit-like motion. The $-\frac{3}{2}\omega t X_0$ term in Eqn 3.8 explains why the motion is not truly elliptical when X_0 is non-zero. This

term accounts for the drift that occurs in the elliptical "orbit".

A 2×1 elliptical "orbit" of the microinspector about the host has the same period as the orbital period of the host about the Earth. Figure 3-3a shows the state deviations when $b = c = 10\,m$, with the 2×1 ellipse centered at the origin ($X_0 = Y_0 = 0$). Figure 3-3b and Figure 3-3c display the in-plane motion and out-of-plane motion, respectively. Assuming that the initial velocity of the microinspector is zero, the Δv to put it into this 2×1 ellipse is $0.011\,m/s$. In this particular example, the non-gravitational forces were set to zero. In Section 2.2, a cold gas thruster capacity of $15\,m/s$ was presented. Comparing the Δv value of $0.011\,m/s$ to this capacity, the advantages to using natural motion to develop the mission becomes obvious. Very little fuel is burned to place the microinspector into these natural "orbits."

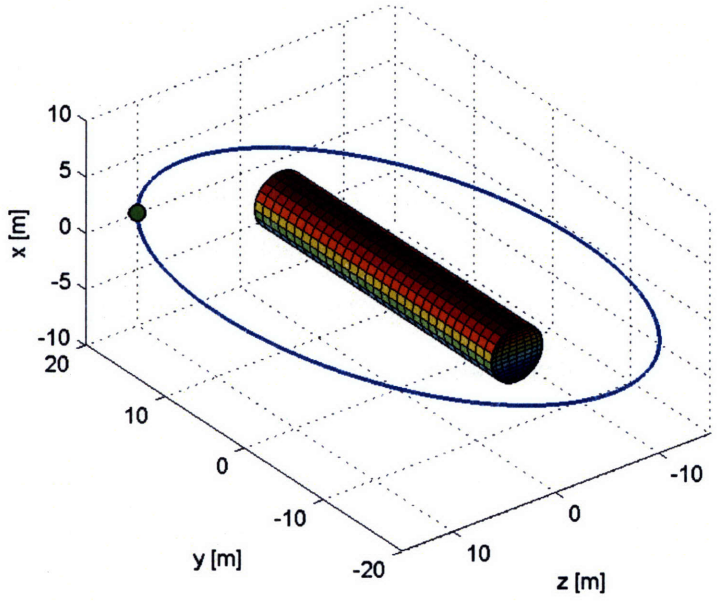

(a) (3D) View

Figure 3-3

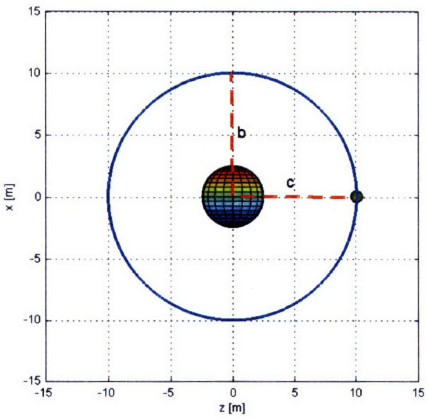

(b) Front View

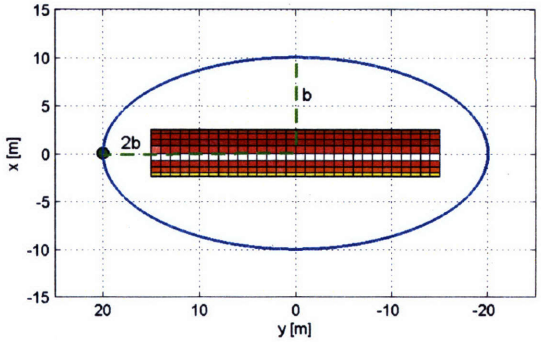

(c) Side View (in-plane)

Figure 3-3: Stationary Inclined 2×1 Elliptical Orbit - $X_0 = Y_0 = 0$, $b = c = 10\,m$, $\phi = 0°$, $\psi = 90°$

For nonzero values of X_0, the 2×1 ellipse drifts horizontally, producing the equally well known traveling ellipse. If the deviation of X_0 is positive (higher than the nominal), the ellipse travels in the negative direction along the V-bar. The microinspector appears to fall behind because its period is larger. Conversely, when the deviation is negative (lower than the nominal), the ellipse travels in the positive direction because its period is shorter. Figure 3-4 portrays the change in motion throughout three orbital periods, due to a nonzero value of X_0.

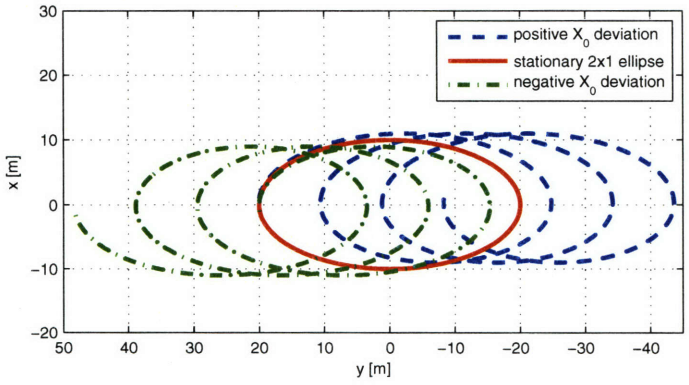

Figure 3-4: Traveling Ellipse

3.2 Avoidance Constraint

A symmetrical, rectangular box constraint is a simple, yet effective keep-out zone that can be applied. Such a constraint may be defined by the mission planner and would account for collision avoidance, as well as plume impingement. Figure 3-5 illustrates the keep-out zone outlined by the box constraint.

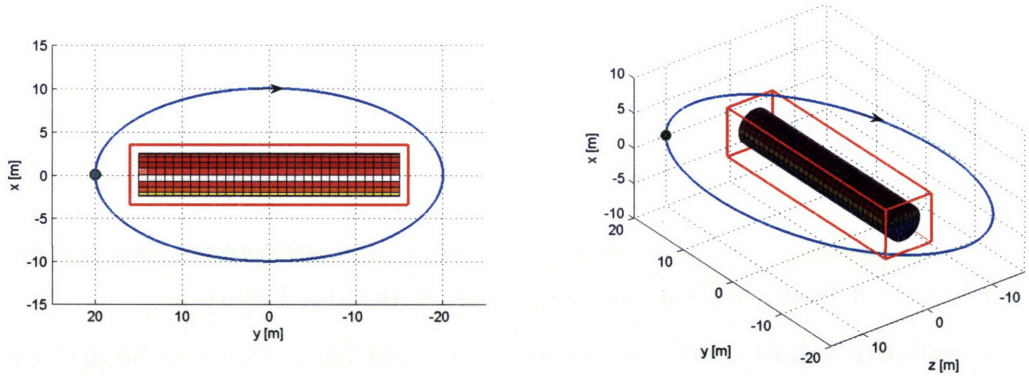

(a) x-y View (in-plane)

(b) 3D View

Figure 3-5: Box Avoidance Constraint

The parameters for a closed relative orbit that does not violate the defined box constraint can be determined analytically. Regardless of the width of the box (along the z-axis), as long as the in-plane 2×1 elliptical shape of the closed relative orbit complies with the constraint, the requirements for the keep-out zone will be satisfied. Thus, it is only necessary to calculate two of the six traveling ellipse parameters of the relative orbit: the semiminor axis, b, and the location of the ellipse's center on the V-bar, Y_0. $X_0 = 0$ since the closed relative orbit does not travel. Given two points on the ellipse, these two parameters may be determined directly from the equation for an ellipse. The ellipse equation in Cartesian coordinates is as follows:

$$\frac{(x - X_0)^2}{a^2} + \frac{(y - Y_0)^2}{b^2} = 1 \tag{3.12}$$

In Eqn 3.12, (X_0, Y_0) locates the center of the ellipse, a is the semimajor axis, b is the semiminor axis, and (x, y) is a point on the ellipse. For a 2×1 ellipse, $a = 2b$

and $X_0 = 0$. Substituting these values into Eqn 3.12 results in:

$$\frac{x^2}{4b^2} + \frac{(y - Y_0)^2}{b^2} = 1 \tag{3.13}$$

Choose two points on the desired 2×1 ellipse: (x_1, y_1) and (x_2, y_2). Then, two equations can be defined using these two points by substituting them into Eqn 3.13. Since there are two unknown variables, b and Y_0, and two equations, the unknowns can be solved for analytically.

By designating both of the two points to be located in the top (+x) or bottom (−x) half of the ellipse, constraint satisfaction of the converse half is assured. In general, for trajectory design in the presence of a box constraint, in this thesis, one point will lie on the V-bar outside of the constraint. The other point will be a corner of the box, furthest from the point on the V-bar, with added margin.

For the cylindrical host model, some other keep-out zones that can be defined are a sphere, elliptical sphere, or a cylinder. The simulation in this thesis will employ the box avoidance constraint, but can be extended to use these other keep-out zones.

3.3 Differential Drag

Differential drag may be defined as the difference in atmospheric drag between two spacecraft vehicles. For the simulations in this thesis, the differential drag is assumed to be constant between the host spacecraft and microsatellite inspector, so that the *CW* solution with the constant differential acceleration in Eqn 3.4 may be utilized for trajectory design. This assumption describes the case in which the orientation of the host vehicle and microinspector do not change in the LVRCS. Nevertheless, in a realistic situation the host vehicle or the microinspector may be rotating in the LVRCS, changing the value for differential drag — which depends on altitude — throughout the orbit. In this case, the differential drag will be somewhat sinusoidal, which could result in a complete or partial cancellation of the effect on the motion. Thus, the case of constant differential drag may be more detrimental to the relative motion than the sinusoidal case over an orbital period. The drag analysis in this

section will show the effect of constant differential drag on a 2×1 ellipse in the LVRCS.

3.3.1 Exponential Atmospheric Model

The atmospheric model used for the drag analysis in this section was taken from Vallado's *Fundamentals of Astrodynamics and Applications* [17]. This model maintains that the density of the atmosphere decays exponentially with increasing altitude. It assumes a spherically symmetric distribution of particles, where the atmospheric density, ρ, varies exponentially according to:

$$\rho = \rho_0 \exp\left(-\frac{h - h_0}{H}\right) \tag{3.14}$$

where, ρ_0 is the reference density, h is the actual altitude, h_0 is the reference altitude, and H is the scale height. The value for ρ_0 and the tabulated values for h_0 and H can be found in Ref. [17]. Figure 3-6 shows the density from 200 km–700 km.

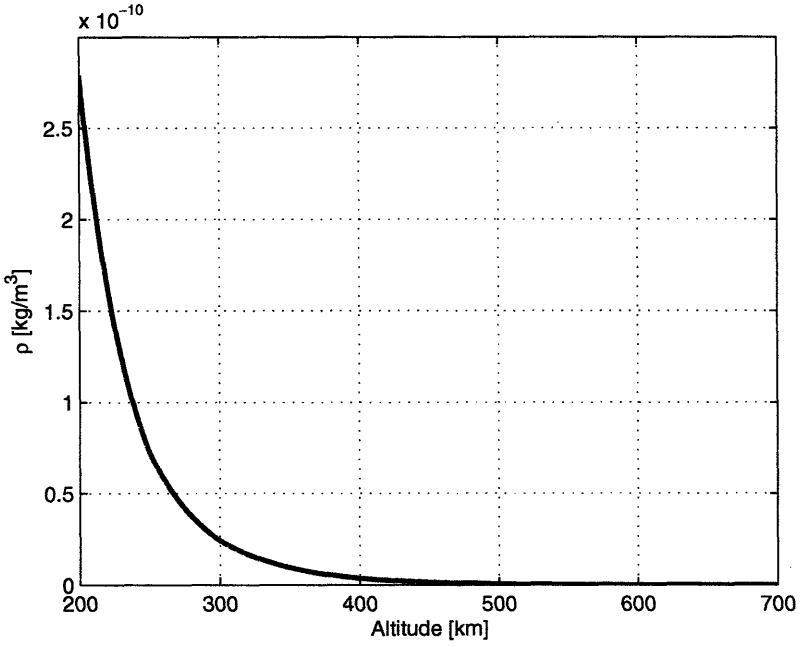

Figure 3-6: Exponential Atmospheric Density Model

3.3.2 Computing Differential Drag

The atmospheric drag force for the microinspector and the host can be calculated by the following formula:

$$\boldsymbol{F}_d = -\frac{1}{2}\rho A C_d v_r \boldsymbol{v}_r \tag{3.15}$$

where ρ is the atmospheric density as before, C_d is the drag coefficient, $\boldsymbol{v}_r$ is the velocity relative to the atmosphere, and A is the reference area.

If $\boldsymbol{F}_{d,h}$ and $\boldsymbol{F}_{d,i}$ represent the drag force of the host vehicle and microinspector, respectively, then the atmospheric drag accelerations of each vehicle are given by:

$$\boldsymbol{a}_{d,h} = \frac{\boldsymbol{F}_{d,h}}{m_h} \tag{3.16}$$

$$\boldsymbol{a}_{d,i} = \frac{\boldsymbol{F}_{d,i}}{m_i} \tag{3.17}$$

where m_h is the mass of the host vehicle and m_i is the mass of the microinspector. The differential acceleration due to drag[§], $\boldsymbol{a}_d$, is the difference in the host and microinspector's acceleration due to drag:

$$\boldsymbol{a}_d = \begin{bmatrix} a_{d,x} \\ a_{d,y} \\ a_{d,z} \end{bmatrix} = \boldsymbol{a}_{d,h} - \boldsymbol{a}_{d,i} \tag{3.18}$$

As discussed in Section B, the total velocity of the microinspector can be interpreted as the orbital velocity of the origin of the LVRCS added to the relative velocity of the microinspector in the LVRCS. The orbital velocity of the LVRCS dominates over the relative velocity of the microinspector. Hence, for the drag analysis in this thesis, the relative velocity is not included in the drag force calculations. Since the greater part of the microinspector's velocity is parallel to the V-bar of the host vehicle, $a_{d,x}$ and $a_{d,z}$ is assumed to be zero. Then, $a_{d,y}$ represents the differential drag, which can be positive, negative, or zero. When the host vehicle has the greater drag,

[§] *differential drag* and *differential acceleration due to drag* are used interchangeably.

$a_{d,y}$ is positive. When the microinspector has the greater drag, $a_{d,y}$ is negative. With equal drag, the value of $a_{d,y}$ is zero. This constant value, $a_{d,y}$, will be part of the d_y component of $\boldsymbol{d}$ in Eqn 3.4. For the remainder of this thesis, the variable a_d will represent the differential drag, with the connotation that it lies along the y-axis of the LVRCS.

The rest of this section examines possible values for differential drag that is attained for the host and microinspector models outlined in Section 2.2. Table 3.2 displays those hardware specifications for the two vehicles.

Table 3.2: Host and Microinspector Models

Specifications	Host Spacecraft	Microinspector
Dimensions	length = $30\,m$ diameter = $5\,m$	$8{\times}8{\times}2\,in^3$ or $0.2{\times}0.2{\times}0.05\,m^3$
Edge Area Face Area	$0.00065\,m^2/kg$ $0.005\,m^2/kg$	$0.00344\,m^2/kg$ $0.01376\,m^2/kg$
Mass	$30{,}000\,kg$	$3\,kg$
Edge Area/mass Face Area/mass	$19.63\,m^2$ $150\,m^2$	$0.01\,m^2$ $0.04\,m^2$

The exponential atmospheric density model in Section 3.3.1 showed that the atmospheric density, ρ, decreases with increasing altitude. Altitudes of $200\,km$ to $700\,km$ from the Earth's surface result in density values ranging from $2.79{\times}10^{-10}\,kg/m^3$ to $3.61{\times}10^{-14}\,kg/m^3$, according to Eqn 3.14. Table 3.3 lists the differential drag values calculated for combinations of two different orientations for the host and microinspector vehicles — the *edge* (minimum reference area) and *face* (maximum reference area) — at varying altitudes. In this table, the edge and face orientations are denoted by E and F, respectively. The drag coefficient, C_d, for both vehicles is set to *2* for the calculations in this section and for the simulations. H stands for the host vehicle and MI represents the microinspector.

Table 3.3: Differential Drag Values

$a_d\, m/s^2$		Altitude $[km]$					
H	MI	200	300	400	500	600	700
E	F	-2.0×10^{-4}	-1.7×10^{-5}	-2.5×10^{-6}	-4.7×10^{-7}	-9.6×10^{-8}	-2.3×10^{-8}
E	E	-4.2×10^{-5}	-3.5×10^{-6}	-5.4×10^{-7}	-9.9×10^{-8}	-2.0×10^{-8}	-5.0×10^{-9}
F	F	-1.3×10^{-4}	-1.1×10^{-5}	-1.7×10^{-6}	-3.1×10^{-7}	-6.4×10^{-8}	-1.6×10^{-8}
F	E	2.3×10^{-5}	2.0×10^{-6}	3.0×10^{-7}	5.5×10^{-8}	1.1×10^{-8}	2.8×10^{-9}

Depending on the orientation of the two spacecrafts, the sign of the differential drag may differ. If the microinspector stays edge on during its orbit, but the host vehicle rotates in the LVRCS, then the differential drag will be sinusoidal. In this case, the total effect on the microinspector's motion relative to the host may be mitigated throughout each orbit. For the trajectory analysis and mission design for a microinspector in this thesis, the host vehicle is assumed to be placed edge on in the LVRCS.

3.3.3 Effect of Varying Altitude on Differential Drag

The exponential atmospheric model makes it possible to approximate the change in differential drag due to a change in altitude. In Eqn 3.15, if all the variables, except density, remain constant, then the ratio of the differential drag at two different altitudes is equivalent to the ratio of the densities at those altitudes. That is, for two different altitudes, h_1 and h_2, where $h_2 > h_1$ and $\Delta h = h_2 - h_1$, the following relationship is derived:

$$K = \frac{a_{d2}}{a_{d1}} = \frac{\rho_2}{\rho_1} = \exp\left(-\frac{\Delta h}{H}\right) \tag{3.19}$$

Eqn 3.19 states that if the change in altitude produces a density ratio of K, then the differential drag at h_2 is approximately $K\times$ the differential drag at h_1.

3.3.4 Effect of Differential Drag on Nominal Trajectories

This section characterizes the orbital degradation due to various magnitudes of the differential drag. The degradation can be described by the change in the semimajor axis, a, of the microinspector's orbit, which is essentially the change of the vehicle's position along the x-axis in the LVRCS. Figure 3-7a illustrates the trajectory of a microinspector that is initially placed at the origin, over a time span of ten orbital periods ($\approx 15.7\,hrs$). The host is in orbit about the Earth at an altitude of 500 km and located at the origin in the LVRCS. The differential drag, a_d, is set to -1$\times 10^{-8}\,m/s^2$ for this analysis. To simulate the motion of the microinspector, the CW solution in Section 3.1.1 is used with this particular value of differential drag. The negative value of a_d means that the microinspector has greater drag, which causes the semimajor axis of its orbit to decrease more than the host's. By Eqn B.10, the velocity becomes greater than the host's velocity. Therefore, in the LVRCS, the microinspector appears to drift below and ahead of the host. The microinspector is effectively spiraling inwards toward the Earth, relatively speaking.

Figure 3-7b shows a closer inspection of the orbital degradation over two orbital periods. The change along the x-axis, Δx, is constant per orbital period, but the change along the y-axis, Δy is greater in the second period than in the first. A periodic motion in the degradation can be observed in the x-direction. Δx and Δy per orbital period can be calculated explicitly using the traveling ellipse formulation of the CW solution, Eqn 3.8. Indeed, evaluation of these equations proves that the change in the motion along the x-axis is periodic due to the constant differential drag. Since the differential drag is assumed to exist primarily along the V-bar, only the in-plane motion due to the drag will be analyzed here.

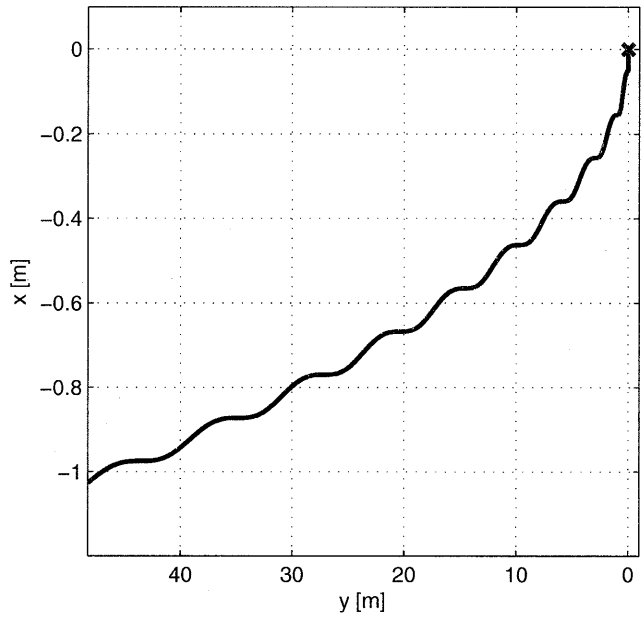

(a) 10 Orbital Periods

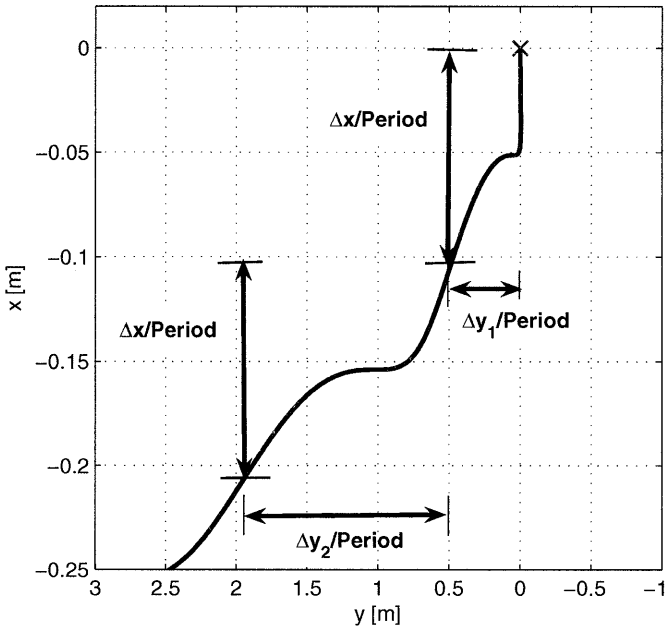

(b) 2 Orbital Periods

Figure 3-7: Orbit Degradation Due to Differential Drag: ($a_d = -1\times10^{-8}\, m/s^2$)

The traveling ellipse equation for the in-plane position of a secondary vehicle due to differential drag in the LVRCS is:

$$x(t) = X_0 + b\sin(\omega t + \phi) + \left(\frac{2t}{\omega} - \frac{2\sin(\omega t)}{\omega^2}\right) a_d \tag{3.20}$$

$$y(t) = Y_0 - \frac{3}{2}\omega t X_0 + 2b\cos(\omega t + \phi) + \left(-\frac{4\cos(\omega t)}{\omega^2} - \frac{3t^2}{2} + \frac{4}{\omega^2}\right) a_d \tag{3.21}$$

At $t = 0$:

$$x(0) = x_0 = X_0 + b\sin(\phi) \tag{3.22}$$

$$y(0) = y_0 = Y_0 + 2b\cos(\phi) \tag{3.23}$$

Then, Δx and Δy are given by:

$$\begin{aligned}\Delta x &= x(t) - x_0 \\ &= b\sin(\omega t + \phi) - b\sin(\phi) + \left(\frac{2t}{\omega} - \frac{2\sin(\omega t)}{\omega^2}\right) a_d \end{aligned} \tag{3.24}$$

$$\begin{aligned}\Delta y &= y(t) - y_0 \\ &= -\frac{3}{2}\omega t X_0 + 2b\cos(\omega t + \phi) - 2b\cos(\phi) + \left(-\frac{4\cos(\omega t)}{\omega^2} - \frac{3t^2}{2} + \frac{4}{\omega^2}\right) a_d \end{aligned} \tag{3.25}$$

If $X_0 = 0$ (microinspector is on the V-bar or in a closed relative orbit), then for $t_k = kP$ and $t_{k-1} = (k-1)P$, where k is an integer and P is the orbital period of the host's orbit, the displacements during one orbital period are given by:

$$\Delta x = x_k - x_{k-1} = \frac{4\pi}{\omega^2} a_d = \frac{P^2}{\pi} a_d \tag{3.26}$$

$$\Delta y = y_k - y_{k-1} = -3P^2 a_d \left(k - \frac{1}{2}\right) \tag{3.27}$$

As shown in Figure 3-7b and in Eqn 3.26, Δx is constant per orbital period. Δx is essentially the change in the microinspector orbit's semimajor axis, a. In Figure 3-7b, Δy was seen to increase with the orbital period. Eqn 3.27 accounts for this observation — the equation for Δy is linear with respect to P^2. Hence, in time, the constant differential drag tends to affect the motion of the microsatellite inspector more along the V-bar. As the orbit degrades further along the x-axis, these results start to break down, since the density changes with different altitudes and the validity of the CW equations is questionable.

Table 3.4 lays out the orbital degradation in the first one orbital period due to an $a_d = 1\,m/s^2$. Since Δx is linear with respect to a_d, to determine the degradation at other values of differential drag, a_d can be multiplied by the appropriate value in Table 3.4. For example, if $a_d = -1\times10^{-8}\,m/s^2$ at $500\,km$, then $\Delta x = 10^7\times(-1\times10^{-8}) = -0.1\,m$.

Δy depends on both a_d and k. Therefore, to determine the degradation at different values of differential drag for the first orbital period, a_d can be multiplied by the appropriate value in Table 3.4, as in the previous example. For subsequent orbital periods, the value in Table 3.4 must also be multiplied by $k+\frac{1}{2}$. As an example, if $a_d = -1\times10^{-8}\,m/s^2$ at $500\,km$ and $k = 3$, then $\Delta y = (-4.8\times10^7)\times(-1\times10^{-8})\times\left(3-\frac{1}{2}\right) = 0.72\,m$.

Table 3.4: Δx and Δy per Orbital Period Due to $a_d = 1\,m/s^2$ at Varying Altitudes

$a_d = 1\,m/s^2$	Altitude $[km]$					
$k = 1$	200	300	400	500	600	700
$\Delta x\,[m]$	9×10^6	9.4×10^6	9.8×10^6	10^7	1.1×10^7	1.1×10^7
$\Delta y\,[m]$	-4.2×10^7	-4.4×10^7	-4.6×10^7	-4.8×10^7	-5×10^7	-5.3×10^7

Since the mission design for the microinspector is primarily based on the natural dynamics described by the CW solution, it is necessary to analyze the impact of differential drag on possible natural trajectories, such as the 2×1 ellipse in the LVRCS. The effect of realistic differential drag values on a 2×1 ellipse is investigated at two different altitudes — $400\,km$ and $700\,km$. The semiminor axis for the 2×1 ellipse is

$b = 20\,m$ in all figures. The a_d values used for the two cases are from Table 3.3.

Figure 3-8 shows that the 2×1 elliptical motion of the microinspector degrades rapidly at $400\,km$. The orbital period of the host vehicle at $400\,km$ is $1.54\,hrs$. By the second orbital period, the relative motion has shifted drastically away from the original 2×1 ellipse. The microinspector penetrates the avoidance constraint box and collides with the host vehicle. There is a noticeable need for orbit maintenance when utilizing natural orbits at $400\,km$. However, even at this altitude, the desired motion may be achieved if maintenance is applied at least a few times per orbital period. Continuous thrust can be avoided, minimizing the overall fuel usage. The degradation at lower altitudes proves to be much more drastic, as can be inferred by this example.

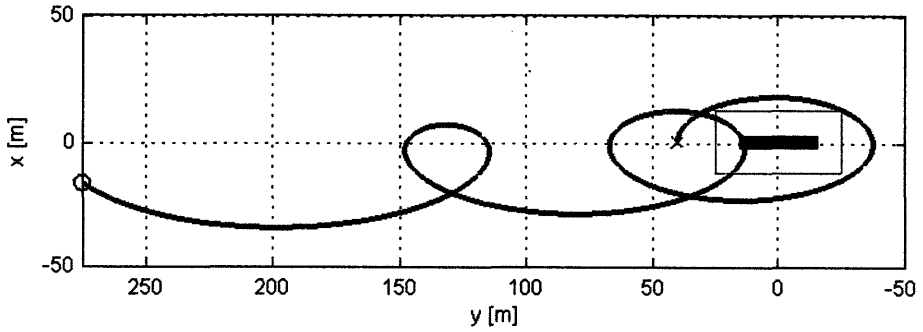

Figure 3-8: 2×1 Ellipse Degradation at $400\,km$ with $a_d = -5.4\times10^{-7}\,m/s^2$ over 3 Orbital Periods

Figure 3-9 illustrates the 2×1 elliptical motion affected by differential drag at an altitude of $700\,km$. The orbital period of the host vehicle at $700\,km$ is $1.64\,hrs$. In contrast from the previous case, the relative motion drifts by a small amount over three orbital periods, due to the decrease in atmospheric density. During the lifetime of the mission, orbital maintenance is still necessary for close proximity operations. However, the frequency of these maintenance maneuvers is much less.

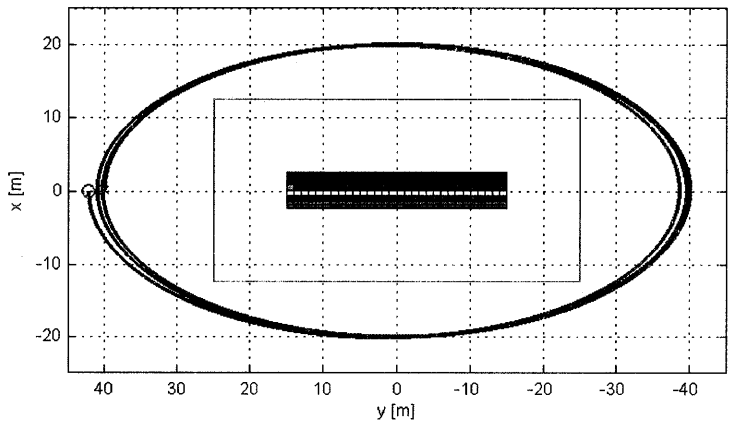

Figure 3-9: 2×1 Ellipse Degradation at $700\,km$ with $a_d = -5.0\times10^{-9}\,m/s^2$ over 3 Orbital Periods

This thesis does not include a specific method or an analysis of methods for orbit maintenance. Rather, the mission design simulations include estimates of the fuel expended per orbital period for orbit maintenance. Fuel estimation for maintenance due to differential drag is covered in Section 4.3.1.

3.4 Forced Motion in Orbit

It was stated in Section 2.3.3, that most visual inspection missions are not considered to be time-critical. However, for those missions that are constrained by time, designing the trajectories based solely on natural motion may not be adequate. It is conceivable that such a mission would be designed to include forced motion maneuvers, in addition to natural motion segments. In essence, for orbiting missions, the forced motion maneuvers are akin to targeting in the presence of disturbances. Given the initial position, $\boldsymbol{r}_i$, final position, $\boldsymbol{r}_f$, and the amount of time to reach the final position, Δt, the velocity vector to reach $\boldsymbol{r}_f$ in Δt can be determined by inverting the *CW* solution. These targeting equations are similar to the Lambert targeting solution. The *CW* solution for position from Eqns 3.4–3.7 can be reformulated as

follows:

$$\begin{aligned}
\boldsymbol{r}_f &= \Phi_r(\Delta t)\boldsymbol{r}_i + \Phi_v(\Delta t)\boldsymbol{v}_i + A_1(\Delta t)\boldsymbol{d} \\
\Phi_v(\Delta t)\boldsymbol{v}_i &= \boldsymbol{r}_f - \Phi_r(\Delta t)\boldsymbol{r}_i - A_1(\Delta t)\boldsymbol{d} \\
\boldsymbol{v}_i &= {\Phi_v}^{-1}(\Delta t)\left[\boldsymbol{r}_f - \Phi_r(\Delta t)\boldsymbol{r}_i - A_1(\Delta t)\boldsymbol{d}\right]
\end{aligned} \tag{3.28}$$

where,

$$\Phi_r(\Delta t) = \begin{bmatrix} 4-3\cos(\omega\Delta t) & 0 & 0 \\ 6\sin(\omega\Delta t) - 6\omega\Delta t & 1 & 0 \\ 0 & 0 & \cos(\omega\Delta t) \end{bmatrix} \tag{3.29}$$

$$\Phi_v(\Delta t) = \begin{bmatrix} \frac{\sin(\omega\Delta t)}{\omega} & \frac{2}{\omega} - \frac{2\cos(\omega\Delta t)}{\omega} & 0 \\ \frac{2\cos(\omega\Delta t)}{\omega} - \frac{2}{\omega} & \frac{4\sin(\omega\Delta t)}{\omega} - 3\Delta t & 0 \\ 0 & 0 & \frac{\sin(\omega\Delta t)}{\omega} \end{bmatrix} \tag{3.30}$$

$$A_1(\Delta t) = \begin{bmatrix} \frac{1}{\omega^2} - \frac{\cos(\omega\Delta t)}{\omega^2} & \frac{2\Delta t}{\omega} - \frac{2\sin(\omega\Delta t)}{\omega^2} & 0 \\ \frac{2\sin(\omega\Delta t)}{\omega^2} - \frac{2\Delta t}{\omega} & -\frac{4\cos(\omega\Delta t)}{\omega^2} - \frac{3\Delta t^2}{2} + \frac{4}{\omega^2} & 0 \\ 0 & 0 & \frac{1}{\omega^2} - \frac{\cos(\omega\Delta t)}{\omega^2} \end{bmatrix} \tag{3.31}$$

$${\Phi_v}^{-1}(\Delta t) = \begin{bmatrix} \frac{3\omega^2\Delta t - 4\omega\sin(\omega\Delta t)}{q} & \frac{2\omega - 2\omega\cos(\omega\Delta t)}{q} & 0 \\ \frac{2\omega\cos(\omega\Delta t) - 2\omega}{q} & \frac{-\omega\sin(\omega\Delta t)}{q} & 0 \\ 0 & 0 & \frac{\omega}{\sin(\omega\Delta t)} \end{bmatrix} \tag{3.32}$$

$$q = -8 + 3\omega\Delta t\sin(\omega\Delta t) + 8\cos(\omega\Delta t) \tag{3.33}$$

In practice, the value of Δt needs to be chosen with care. Since the algorithm takes the inverse of $\Phi_v(\Delta t)$, this matrix must not be singular or close to singular. This implies that the orbital period, P, and integer multiples of P cannot be used as

Δt. In addition, the computed $\Delta \boldsymbol{v}$ may cause the microinspector to collide with the host — another negative aspect of the forced motion method.

3.5 Boresight Vector

In Section 3.1, the advantages of using natural motion via the *CW* solution to develop the mission were discussed. Not only does the *CW* solution present a simple, predictive, and effective method of designing trajectories, it is also extremely fuel efficient. The microinspector can easily be placed in a relative closed orbit about the host, giving ample opportunities for viewing many parts of the host's surface. Once in a relative closed orbit or another type of natural motion, the attitude of the microinspector must be directed and controlled so that the camera's boresight vector is pointed properly at the host. Continuous control of the vehicle's attitude can take up a large percentage of the fuel budget. However, there are some aspects of the relative closed orbits that may be utilized to acquire excellent coverage of the host vehicle, while minimizing fuel usage due to attitude control. This section explores and presents these possible boresight vector trajectories for some of the natural motions.

3.5.1 Boresight: Case 1 with In-plane 2×1 Stationary Ellipse

Assume that the vehicle is in a 2×1 stationary ellipse about the host vehicle, and the camera's boresight vector is initially pointed normal to the host's surface at ϕ = 0°, 90°, 180°, or 270°. Then, during its translational motion about the host, the boresight vector will rotate in the LVRCS, all the while pointing toward the host, as shown in Figure 3-10a. With the appropriate 2×1 ellipse size, the microinspector can take images of the edges, top, and bottom of the host vehicle. Figure 3-10b illustrates the position of the microinspector in the inertial frame and the direction of the boresight vector. The attitude of the microinspector does not actually change in the inertial reference frame. No extra fuel is needed to achieve this motion of the boresight vector in the LVRCS.

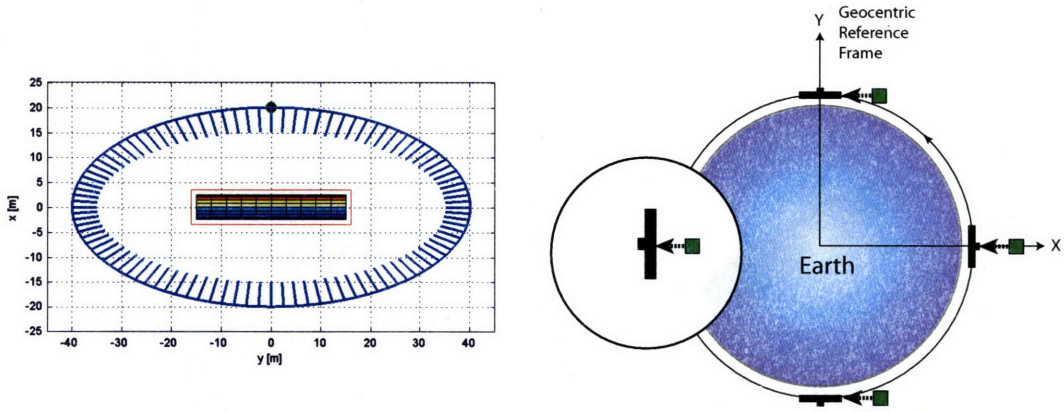

(a) LVRCS (b) Inertial Reference Frame

Figure 3-10: Boresight Case 1 with In-plane 2×1 Stationary Ellipse: The camera's boresight vector is in fixed inertial direction

3.5.2 Boresight: Case 2 with Stationary on V-bar

Placing the microinspector in front of or behind the host vehicle in the LVRCS on the V-bar is another position for easy observation. The camera's boresight vector can be controlled to point toward the host during the orbit. In the LVRCS, the boresight vector appears to be stationary, as shown in Figure 3-11a. However, in the inertial reference frame, the boresight vector is rotating at the orbital rate. This constant rotation is shown in Figure 3-11b. Instead of controlling the attitude of the microsatellite inspector precisely, with proper pointing initialization, the constant rotation may be achieved by spinning up the vehicle to the orbital rate of the host vehicle about a specified body-fixed axis. Thus, fuel can be minimized, while still achieving the pointing requirements. Section 4.3.2 presents a method for estimating the Δv used in the spin-up of a satellite.

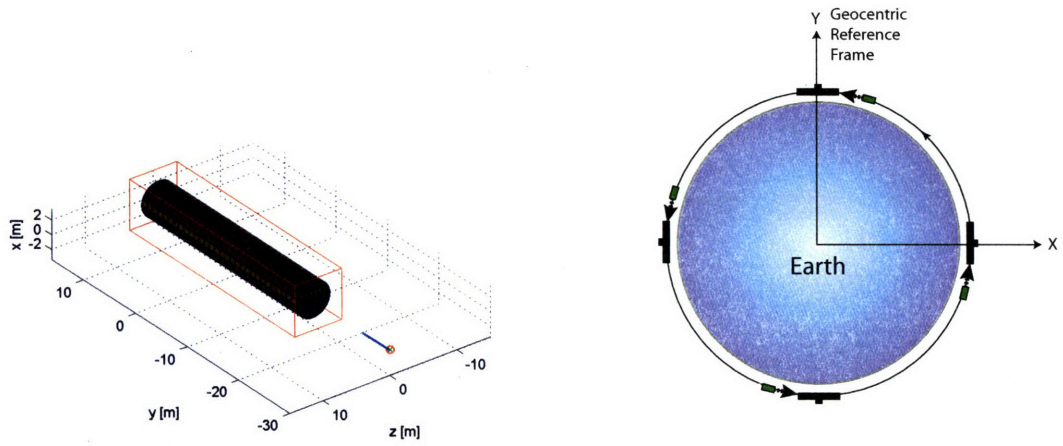

(a) LVRCS

(b) Inertial Reference Frame

Figure 3-11: Boresight Case 2 with Stationary on V-bar: The camera's boresight vector is rotating at the orbital rate.

3.5.3 Boresight: Case 3 with Inclined 2×1 Stationary Ellipse

For an inclined 2×1 ellipse about the host vehicle, a natural choice of motion for the camera's boresight vector is to rotate it at the orbital rate about a vector normal to the ellipse. In this case, the boresight vector will always lie in the plane of the ellipse. As in the first case, with proper initialization, the camera's boresight vector will point inwards throughout the orbit. Again, the microinspector can capture an encircling view of the host's surface at different angles, as shown in Figures 3-12a–3-12b. Figures 3-12c–3-12d depict the corresponding position and attitude of the microinspector in the geocentric inertial coordinate system. The attitude control needed in the inertial frame of reference in order to achieve this type of camera maneuvering in the LVRCS is more complex than the previous cases. Figure 3-12e shows the motion of the boresight vector in inertial space that is required to achieve the constant rotation in the LVRCS. Note that explicit control of the rotational motion about the boresight vector is not necessary, apart from keeping the angular rates below a specified level. This is an extra degree-of-freedom which may be used to maximize Sun exposure to the solar array.

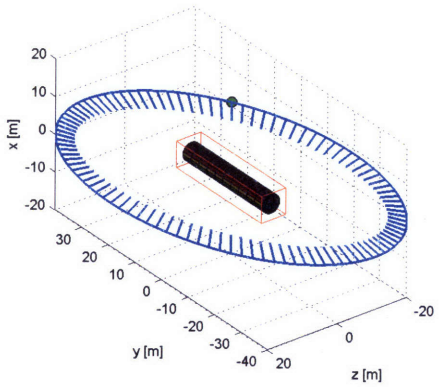

(a) LVRCS (3D)

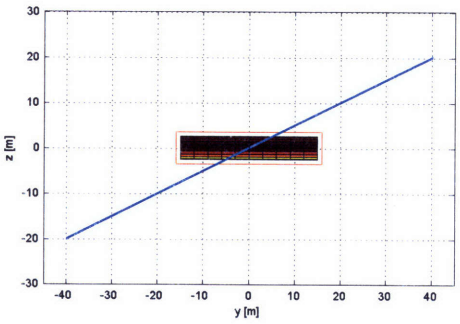

(b) Top View

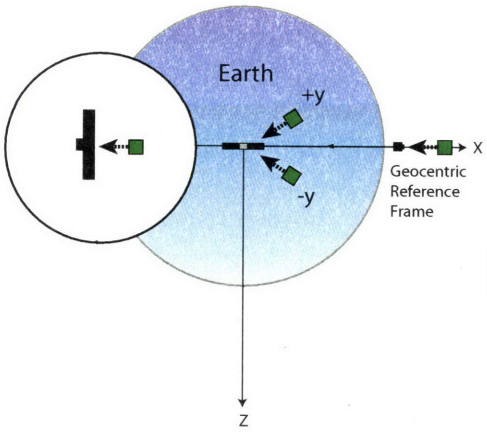

(c) Inertial Edge View

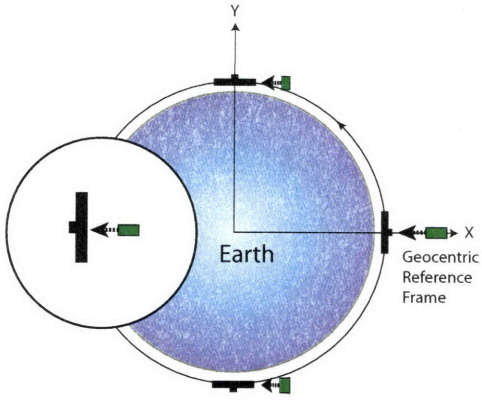

(d) Inertial Side View

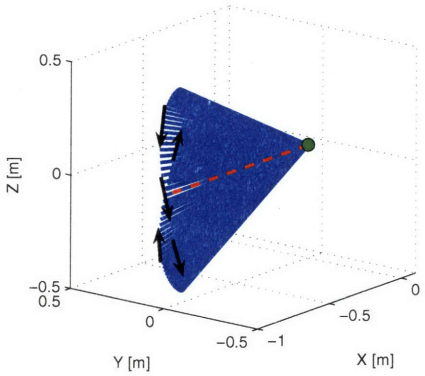

(e) Camera's Boresight Vector in Inertial Reference Frame

Figure 3-12: Boresight Case 3 with Inclined 2×1 Stationary Ellipse: The microinspector in an inclined 2×1 stationary ellipse about the host.

3.5.4 Boresight: Case 4 with Inclined 2×1 Stationary Ellipse

The last example is similar to the previous one, except for the pointing of the camera as the microinspector travels about the host vehicle in an inclined 2×1 ellipse. If the inclined 2×1 ellipse is nearly circular in the x-z plane, then a practical pointing solution is to have the camera's boresight vector rotate in the x-z plane, such that the boresight vector stays normal to the V-bar (y-axis). This type of pointing motion is shown in Figures 3-13a–3-13b. One can immediately see the implications of achieving this type of boresight vector motion in the LVRCS. Assume a succession of these inclined 2×1 ellipses at different locations on the V-bar. With the rotation of the boresight vector in the x-z plane, the microinspector can capture images of most of the host's surface, if the length of the host lies on the V-bar. The position and attitude of the microinspector is shown in Figure 3-13c, and the motion of the boresight vector in inertial space is displayed in Figure 3-13d.

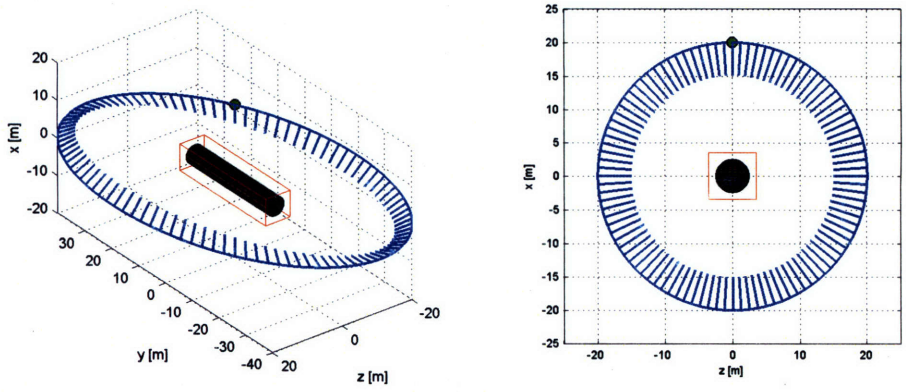

(a) 3D View (b) Front View

Figure 3-13

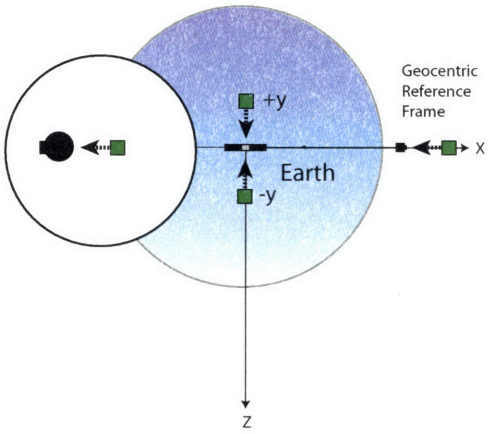

(c) Inertial Reference Frame

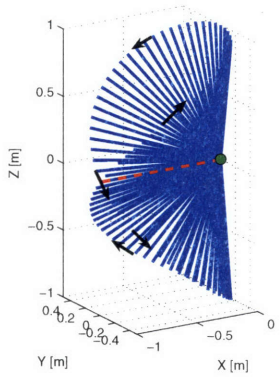

(d) Camera's Boresight Vector in Inertial Reference Frame

Figure 3-13: Boresight Case 4 with Inclined 2×1 Stationary Ellipse: The microinspector in an inclined 2×1 stationary ellipse about the host.

3.6 Sun Angle and Recharging Batteries

Another aspect of the microinspector that must be examined before designing the mission is the power system. This thesis focuses specifically on a microinspector design that is equipped with solar cells for continuous operation in the Sun and batteries when solar energy is not available. The *sun angle*, ϕ_{sa}, is defined here as the angle between the light ray from the Sun and the vector normal to the solar cells on the microsatellite. Figure 3-14 gives a graphical definition. This type of hardware setup for the microsatellite allows operation of all power consuming systems when the sun angle is less than some specified angle, $\phi_{sa,max}$, via the solar cells alone. During this time, if the battery reserves are less than the maximum capacity, these batteries can be recharged by the solar cells. $\phi_{sa,max}$ is less than or equal to 90°, and may be determined by the average power usage by the microsatellite. While $\phi_{sa} > \phi_{sa,max}$, the microinspector can run off the batteries, until the sun angle is once again adequate for solar cell usage. In summary,

- $\phi_{sa} > \phi_{sa,max}$: Batteries are discharging
- $\phi_{sa} < \phi_{sa,max}$: Batteries are charging

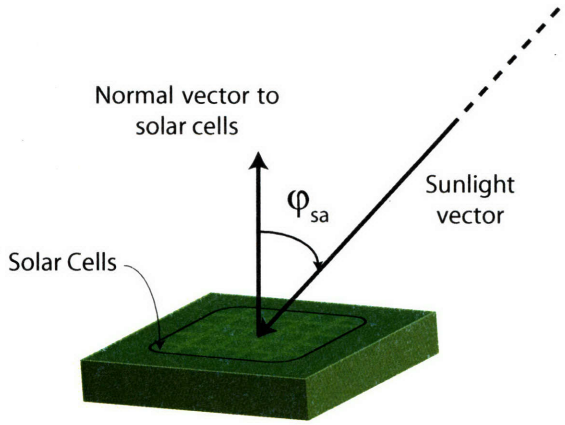

Figure 3-14: Sun Angle, ϕ_{sa}

In this thesis, "solar cell mode" is when the batteries are charging, and "battery mode" is when the batteries are being discharged. In order to determine the proper specifications for the microinspector's power system, the amount of time spent in solar cell mode and battery mode during a typical orbital maneuver needs to be evaluated. One obvious goal in designing a mission for a microinspector with solar cells is to stay in solar cell mode for the majority of the mission time. If the battery's state of charge (SOC) is below the specified minimum SOC, it will become necessary to recharge by pointing the solar cells toward the Sun, during the mission. Since this takes time away from the inspection part of the mission, it is desired to avoid these recharging maneuvers, if possible. While still attaining the desired motion of the camera boresight vector, the orientation of the microinspector that minimizes ϕ_{sa} throughout the mission must be determined. For the following analysis, $\phi_{sa,max}$ is assumed to be 90°. Another assumption is that the solar cells are placed only on one side of the microsatellite, as shown in Figure 3-14. The camera viewpoint is located on one of the edges of this box shaped microinspector model.

Five different cases are discussed to illustrate the problem. The first three cases depict an in-plane 2×1 elliptical motion by the microinspector in the LVRCS, with different lighting and phasing conditions. The boresight vector appears to rotate at the constant orbital rate and is initialized to point at the host's surface, as in Figure 2-7a. In the fourth case, the microinspector is stationary behind the host vehicle on

the V-bar, with the camera's boresight vector pointing at the host. Finally, in the fifth case, the microinspector is placed in an inclined 2×1 ellipse in the LVRCS. The camera's boresight vector appears to rotate at the constant orbital rate in the LVRCS, and is always perpendicular to the V-bar, as in Section 3.5.4. The scales of the vehicles are exaggerated in all figures, in order to present the concept.

3.6.1 Sun Angle: Case 1 with Sun Facing the Orbital Plane of Host

In the first case, the Sun faces the orbital plane of the host and the microinspector is placed in a 2×1 ellipse about the host vehicle. In the inertial reference frame, the microinspector does not rotate about its axes. However, in the LVRCS, this corresponds to constant angular rotation of the boresight vector, which allows the microinspector to capture images of a large portion of the host's surface, as shown in Figure 3-15a. In order to maximize Sun exposure to the solar cells, the microinspector can be initially oriented so that the solar cells face the Sun, as seen in Figure 3-15b. Then, throughout the 2×1 ellipse motion, $\phi_{sa} = 0$, permitting the vehicle to operate solely on solar energy. This case is ideal for power usage, since the reserve batteries are never used.

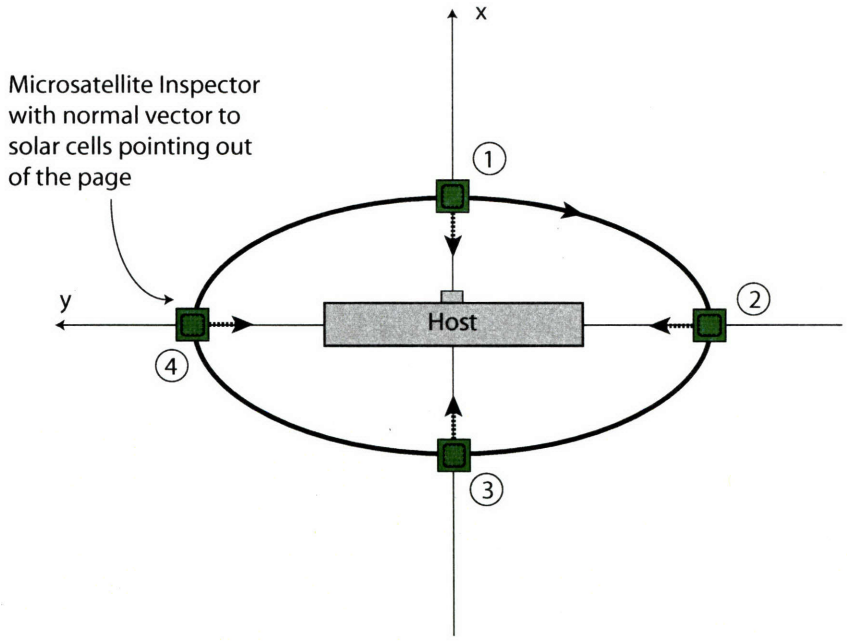

(a) In-plane 2×1 Stationary Ellipse in Relative Reference Frame

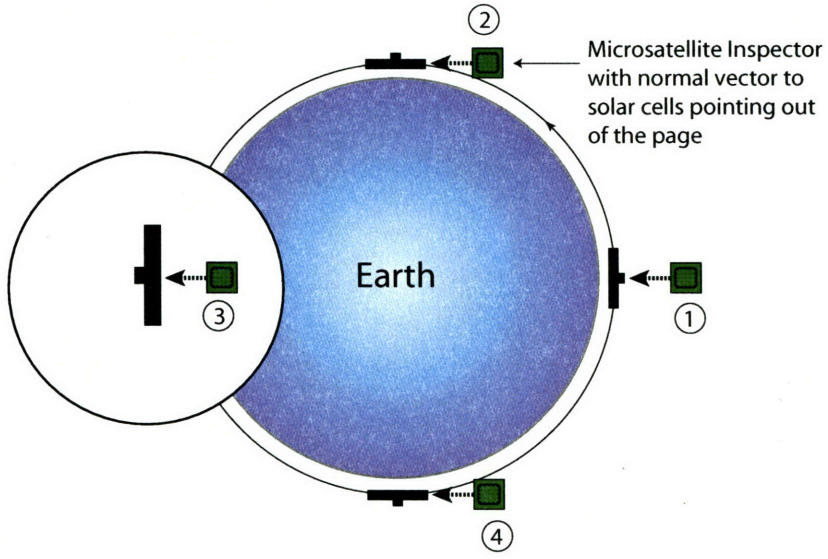

(b) In-plane 2×1 Stationary Ellipse in Geocentric Reference Frame

Figure 3-15: Sun Angle Case 1 with Sun Facing the Orbital Plane of Host: The microinspector is in an in-plane 2×1 stationary ellipse about the host. The Sun is normal to the solar cells on the microsatellite throughout the orbit.

3.6.2 Sun Angle: Case 2 with Sun in Orbital Plane of Host

In contrast, the second case presents the worst possible scenario for power consumption. The Sun is in the same plane as the host's orbital plane, and the microinspector is again in a 2×1 ellipse about the host vehicle. When the top of the host vehicle is normal to the Sun, the microinspector is positioned and oriented, so that the camera has a view normal to the top of the host. In traveling ellipse terms, the in-plane phase angle starts at 90°. This is illustrated in Figure 3-16b. As in the first case, a large percentage of the host's surface may be captured with this setup. However, there is no orientation of the microinspector that will give the proper Sun exposure to the solar cells. Thus, the sun angle can never be less than 90°, which signifies that the batteries are not recharged throughout the 2×1 ellipse motion, the batteries must be used. Upon energy depletion, the batteries must be recharged by pointing the solar cells toward the Sun.

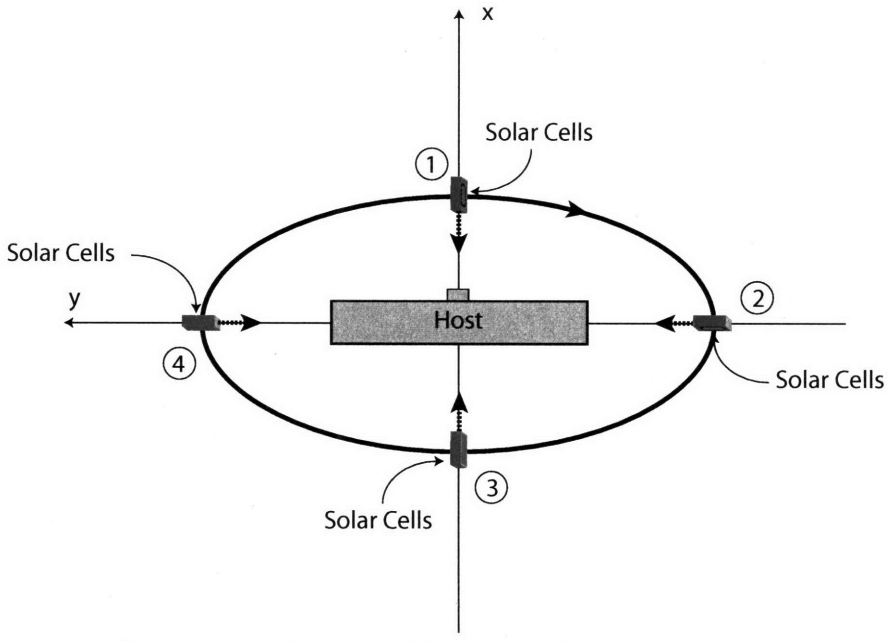

(a) In-plane 2×1 Stationary Ellipse in Relative Reference Frame

Figure 3-16

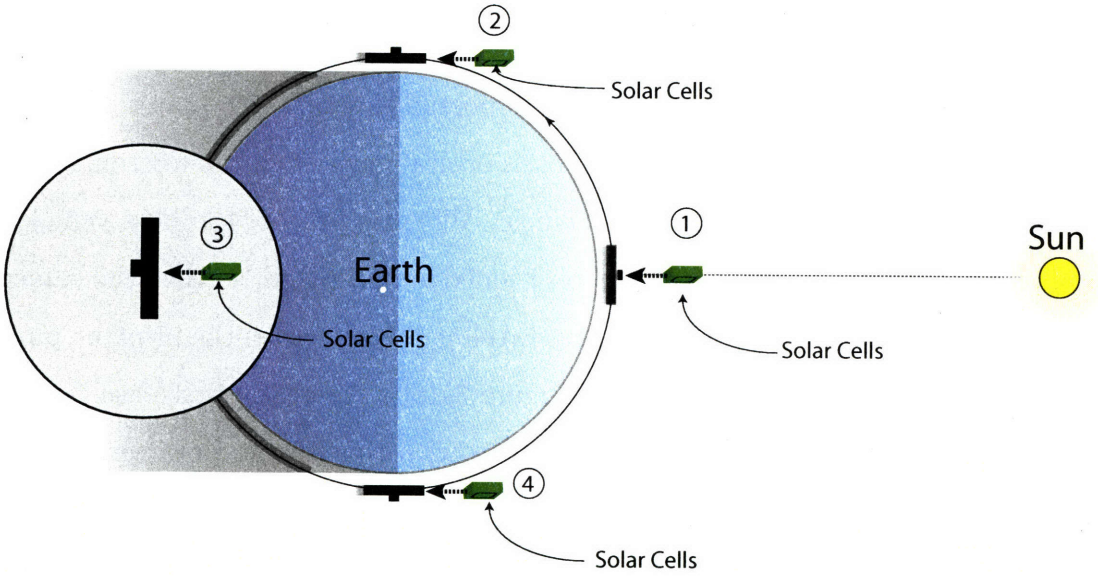

(b) In-plane 2×1 Stationary Ellipse in Geocentric Reference Frame

Figure 3-16: Sun Angle Case 2 with Sun in the Orbital Plane of Host: The microinspector is in an in-plane 2×1 stationary ellipse about the host. When the top of the host vehicle is normal to the Sun, the microinspector is positioned and oriented, so that the camera has a view normal to the top of the host.

3.6.3 Sun Angle: Case 3 with Sun in Orbital Plane of Host

The third case is similar to the previous one in all aspects, aside from the phasing. When the top of the host vehicle is normal to the Sun, the microinspector is positioned at an in-plane phase angle of 45° in the 2×1 ellipse, and oriented so that the boresight vector points toward the host at a 45° angle. If the microinspector is initially oriented so that the sun angle is minimized, then the solar cells have Sun exposure during the orbit, outside of Earth's shadow, as displayed in Figure 3-17. $\phi_{sa} = 45°$ for nearly two-thirds of the orbital period, so the back-up battery need only be used in Earth's shadow, assuming that $\phi_{sa,max}$ is greater than 45°. Depending on the specifications of the battery and solar cells, specific recharging maneuvers may not need to be included in the mission. The battery may be sufficiently recharged during the solar cell mode. This example shows the importance of phasing the relative motion appropriately, to optimize solar cell usage.

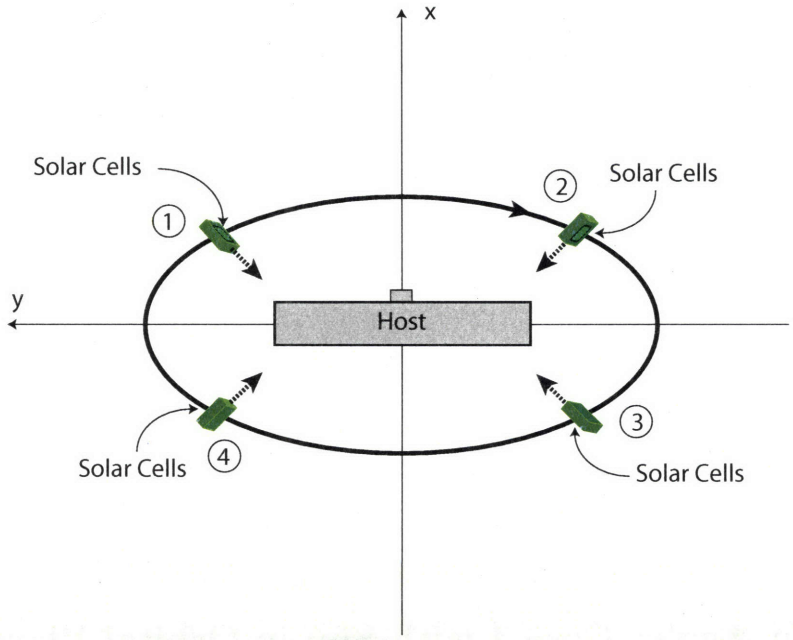

(a) In-plane 2×1 Stationary Ellipse in Relative Reference Frame

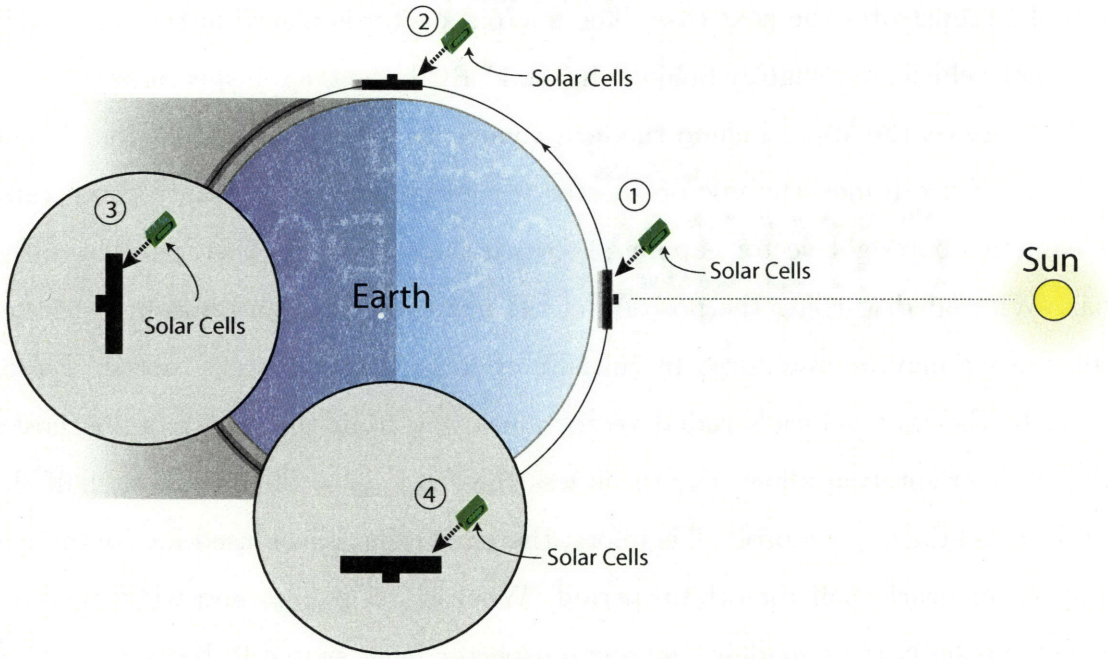

(b) In-plane 2×1 Stationary Ellipse in Geocentric Reference Frame

Figure 3-17: Sun Angle Case 3 with Sun in the Orbital Plane of Host: The microinspector is in an in-plane 2×1 stationary ellipse about the host. The initial in-plane phase angle is 45° in the 2×1 ellipse and oriented so that the boresight vector is pointed toward the host at a 45° angle.

From the lighting cases presented in this section and Section 3.6.2, it can be inferred that if the initial in-plane phase angle is 90°, then the attitude of the microinspector can be initialized to have the solar cells always pointing at the Sun. $\phi_{sa} = 0°$ when not in Earth's shadow, during the orbit. In contrast to the case in Section 3.6.2, the solar cells are ideally positioned; however, the host's surface that is in the FOV of the camera, is never illuminated and no images can be obtained with this setup.

For the microinspector trajectory and attitude setup in this section and Section 3.6.2, some of the limitations in the trade-off between observing the host and charging the batteries may be mitigated if the vector normal to the solar cells is opposite in direction to the camera's boresight vector.

3.6.4 Sun Angle: Case 4 with Sun in Orbital Plane of Host

Figure 3-18 illustrates the next case. The microinspector is placed in the same orbit as the host vehicle, but slightly behind. In the LVRCS, the microinspector appears to be stationary on the V-bar behind the host vehicle, as shown in Figure 3-18a. In the inertial reference frame, the microinspector is rotating at the constant orbital rate. The camera's boresight vector is pointed toward the edge of the host, parallel to the V-bar. Without disturbing the position of the microinspector and boresight vector, battery usage may be minimized by initially orienting the solar cells' normal vector parallel to the host vehicle's radial vector and away from the center of the host's orbit. This orientation allows ϕ_{sa} to be less than $\phi_{sa,max} = 90°$ for about half the orbital period during one orbit. Therefore, the solar cells can be used for continuous operation for nearly half the orbital period. When $\phi_{sa} > \phi_{sa,max}$ and when the host vehicle is in the Earth's shadow, the microinspector must switch to battery mode to continue operating. Once again, specific recharging maneuvers may not be necessary given the specifications of the battery and solar cells.

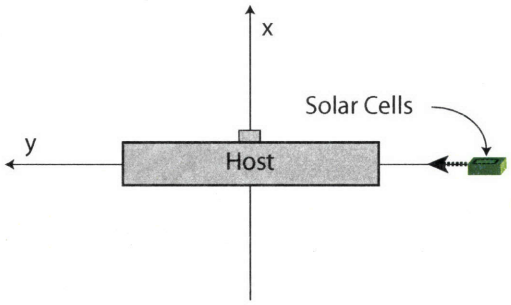

(a) Stationary on V-bar in Relative Reference Frame

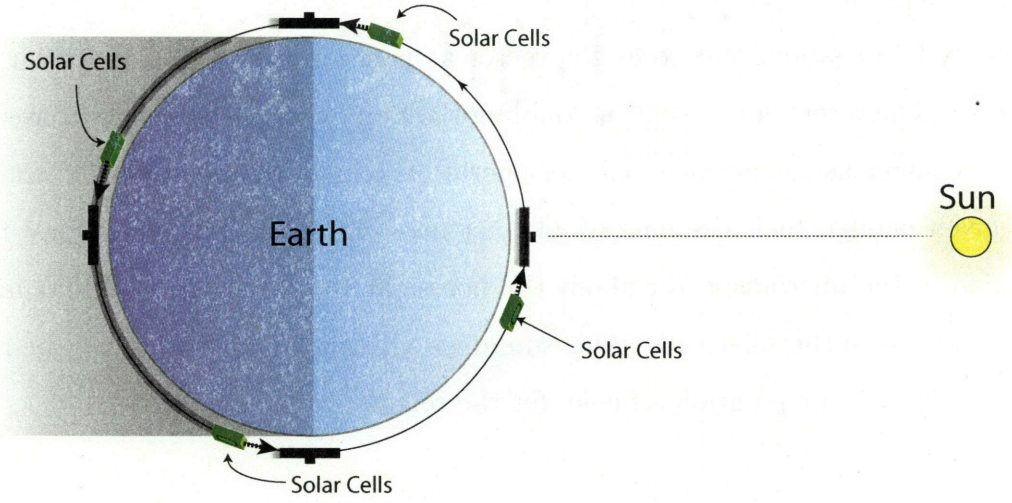

(b) Stationary on V-bar in Relative Reference Frame

Figure 3-18: Sun Angle Case 4 with Sun in the Orbital Plane of Host: The microinspector is stationary on the V-bar behind the host vehicle. The camera's boresight vector is pointed toward the edge of the host.

3.6.5 Sun Angle: Case 5 with Sun in Orbital Plane of Host

Finally, in the last example, the microsatellite inspector is in an inclined 2×1 stationary ellipse about the host vehicle. The camera's boresight vector is pointed toward the host, normal to the surface, as in Section 3.5.4. The view down the V-bar looks circular for this particular case. To achieve this type of relative motion, a rotational Δv must be applied at positions ①–④ to spin-up the attitude to the orbital rate in the directions shown in Figure 3-19b. The camera's boresight vector follows the path illustrated in Figure 3-13d. With no further attitude control maneuvers, the solar cells are exposed to the Sun for less than a third of the orbital period. However, upon closer inspection, this example brings a new possibility to light. There is an extra degree of freedom about the camera's boresight vector, which can be utilized to acquire more Sun exposure to the solar cells. In this example, the microinspector can be rotated 180° about the boresight vector at positions ① and ③, as shown in Figure 3-19. These rotations result in doubling the Sun exposure time, and consequently the time spent using the solar cells for operation. Under different lighting conditions and given enough fuel, the mission planner may choose to actively control the orientation of the microinspector about the boresight vector, in order to maximize the Sun exposure to the solar cells. This sun angle minimizing algorithm will be referred to as the Sun-nadir pointing scheme, for the remainder of this thesis.

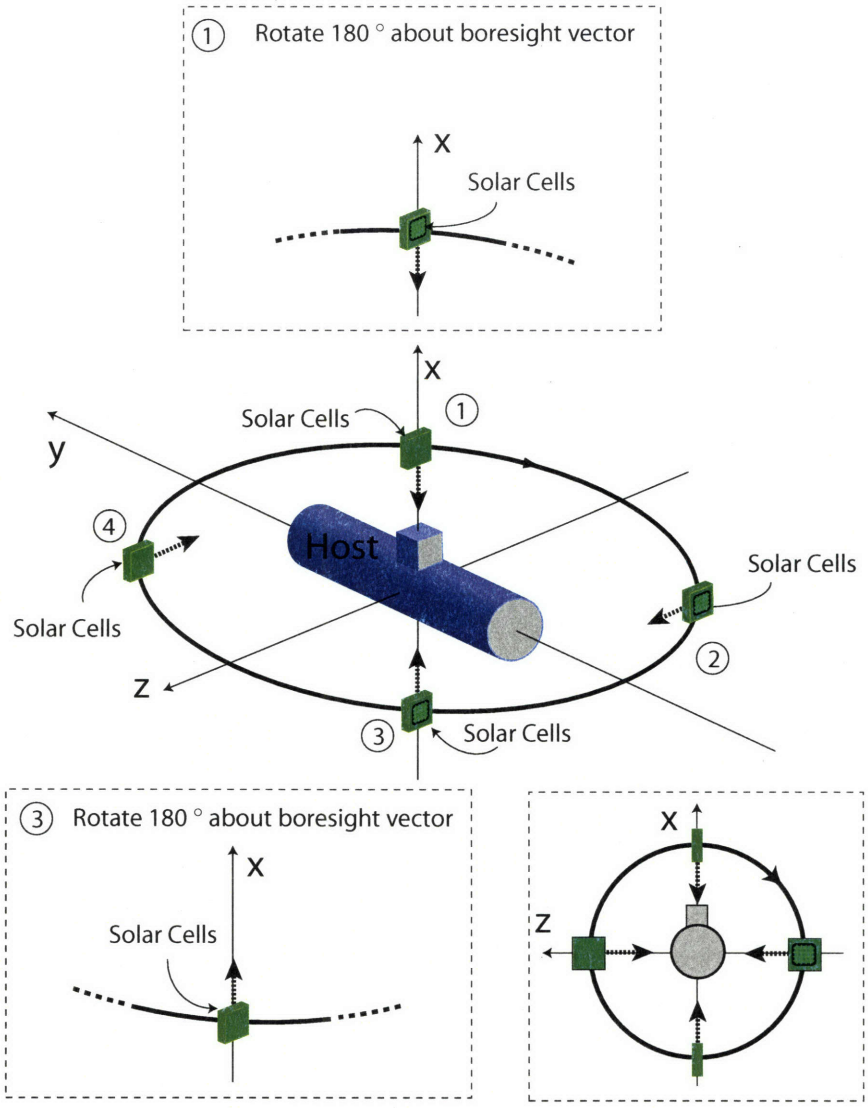

(a) Inclined 2×1 Stationary Ellipse in Relative Reference Frame

Figure 3-19

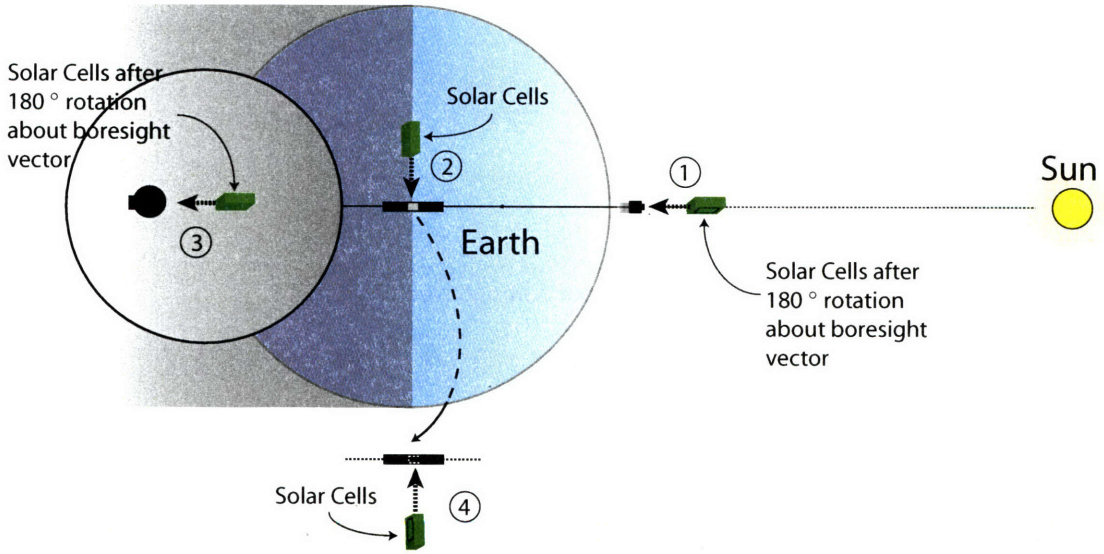

(b) Inclined 2×1 Stationary Ellipse in Relative Reference Frame

Figure 3-19: Sun Angle Case 5 with Sun in the Orbital Plane of Host: The microinspector is in an inclined 2×1 ellipse about the host vehicle. The camera's boresight vector is pointed toward the host, normal to the surface.

3.6.6 Recharging

In reality, $\phi_{sa,max}$ will be much less than 90°, due to the average power needed to continue running all systems on board the microinspector. Additionally, the battery reserves will not be completely depleted before conducting recharging maneuvers. For instance, assume that the maximum power attained from the solar cells is $25\,W$, which corresponds to a sun angle of 0°. The solar array is assumed to have cosine losses; therefore, at sun angles less than 90°, the amount of power that can be obtained from the solar cells is approximately given by Eqn 3.34.

$$\text{Power from solar cells}\,(W) = 25\cos(\phi_{sa}),\ \text{for}\ 0° \leq \phi_{sa} \leq 90° \tag{3.34}$$

Let the peak capacity of the battery be $45\,W{\cdot}hr$. If the average power used for operation of the microinspector is $14\,W$, then continuous usage of the battery will completely drain it in about $3.2\,hrs$. Recharging the battery from this drained state takes about $4\,hrs$ at a 0° sun angle. At sun angles greater than 56°, the solar cells produce less than $14\,W$, so the microinspector must switch to battery mode. Thus,

$\phi_{sa,max}$ is defined to be 56°.

3.7 Mission Assessment through Figures of Merit

Rating the successfulness of an inspection mission by a microinspector depends greatly on the host spacecraft and the type of inspection that is desired. For example, a microsatellite inspector may be used to observe the solar sails unfurl from a sailcraft. This particular mission would probably require the microinspector to be placed afar and point at the host vehicle, in order to capture the entirety of the solar sail deployment. Another use for a microinspector would be to take images of the surface of a manned space vehicle for damage. Unlike the sailcraft mission, the microinspector would need to maneuver about the host vehicle to capture images of the complete surface. The resolution of the images would be considered an important measure of success for this mission. This section presents some figures of merit that would be useful to rate and design an inspection mission. Most likely, no one figure of merit will be adequate in rating the quality of a mission. The mission designer must apply an appropriate weighting factor to each of several possible figures of merit.

3.7.1 Fuel Expenditure

Fuel expenditure is a figure of merit that is key in rating and designing any microsatellite mission. Because of the limited amount of fuel on board a typical microsatellite, trajectory design for a mission that minimizes fuel usage is highly desirable. Fuel expenditure can dramatically reduce the usable mission lifetime of the microinspector when a complex re-docking and re-fueling option is not available. If the actuators for attitude control are the same thrusters used for translational motion, then fuel minimization becomes even more critical. This thesis assumes that the microinspector has no momentum exchange devices on board for attitude control, and that the thrusters are used for both translational and rotational maneuvers.

3.7.2 Host Surface Coverage

For visual inspection missions that survey the total surface area of the host vehicle, a figure of merit is needed to ensure that the microinspector captures images of the entire surface. A simple method is to divide the surface of the host vehicle into segments. When the center point of a segment is in the field of view (FOV) of the camera and the segment is illuminated by sunlight, the complete segment is assumed to be viewed, in this thesis. The smaller the segments are made, the more accurate this assumption. Thus, throughout the course of the mission, the sections of the host that are viewed can be determined by this figure of merit. Figure 3-20 illustrates the points on the surface of the host vehicle model. A vector normal to the surface at each point is drawn in the figure. Figure 3-21 displays the surface area of the cylindrical host model. Each segment is represented by a number. If all the segments are viewed by the microinspector, then this figure of merit affirms that the microinspector successfully captures images of the total surface. The top row in Figure 3-21 represents the top of the host surface in the LVRCS frame when the length is along the V-bar. The fifth row represents the bottom of the host surface.

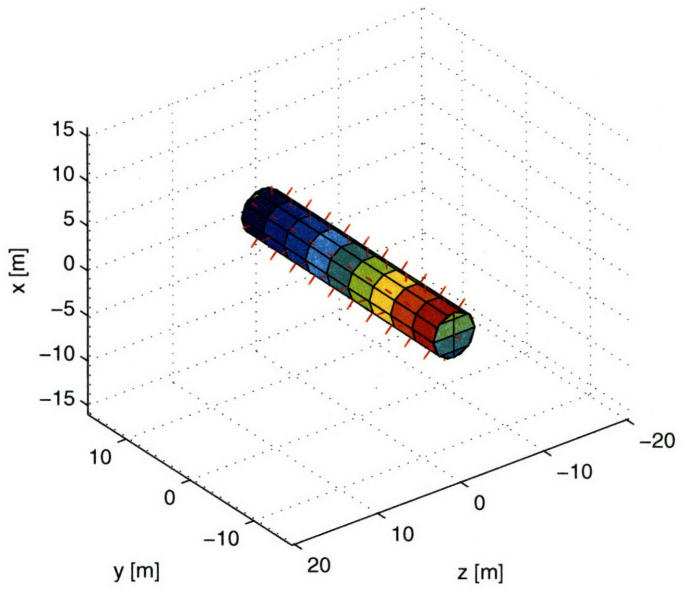

Figure 3-20: Points on Surface of Host Spacecraft

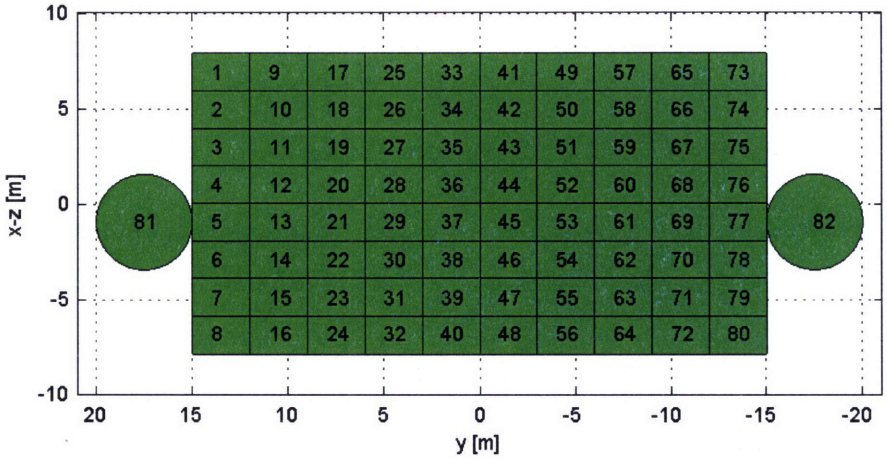

Figure 3-21: Surface Grid Labeling of Host Vehicle Segments

To determine whether or not a point on the surface of the host appears in an image taken by the camera, at least two conditions must be fulfilled. First, the point must be within the conical FOV of the camera. Second, the view must be visable to the camera with no obstruction. Figure 3-22 provides an illustration of the vectors and angles used in the calculations to determine if the conditions are met.

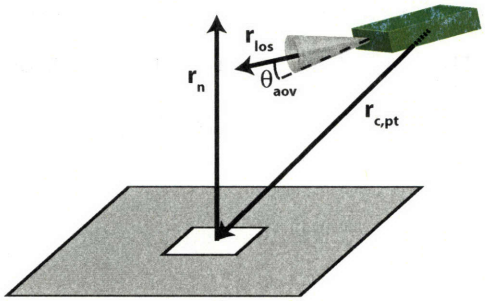

Figure 3-22: Host Surface and Camera Vectors and Angles

With θ_{aov} as the angle of view of the camera, $\hat{\boldsymbol{r}}_{los}$ as the boresight unit vector from the camera, $\boldsymbol{r}_{c,pt}$ as the position vector from the camera to the point on the surface, and $\hat{\boldsymbol{r}}_n$ as the normal vector to the point on the surface, the calculations to demonstrate that the two conditions are met are as follows:

1. Point is contained in FOV: $\cos^{-1}\left(\frac{\hat{\boldsymbol{r}}_{los}\cdot\boldsymbol{r}_{c,pt}}{|\hat{\boldsymbol{r}}_{los}||\boldsymbol{r}_{c,pt}|}\right) \leq \frac{\theta_{aov}}{2}$

2. Point is viewable by the camera: $\boldsymbol{r}_{c,pt}\cdot\hat{\boldsymbol{r}}_n > 0$

If both these conditions are met, then the point on the surface of the host is said to be visible to the camera.

3.7.3 Frequency of Host Surface Coverage

Another figure of merit that is directly correlated with viewing points on the host's surface is the frequency or total time that a point is viewed. In a typical mission, it is foreseen that some sections of the host's surface may be captured more often than others. A figure of merit relating the frequency of the viewed points would provide knowledge on which sections the microinspector has more opportunities to view and image. In mission simulations, the frequency can be determined by summing the number of times the point is in the FOV of the camera per time step.

3.7.4 Angles of Host Surface Coverage

The inspection mission may require the microinspector to take images of the host's surface at different angles. The angle variety provided by the assorted images gives perspective on any possible damage to the surface. If all the images are taken normal to the surface, an object that is loose or raised may not be apparent. For a general overview of the host's surface, it is desirable to acquire a multifaceted portrait of the vehicle through the images taken by the microinspector. A figure of merit that depicts the variety of angle views of the host surface would rate how close the mission is to achieving this goal.

3.7.5 Lighting

Some problems associated with lighting from the Sun were discussed earlier in Section 2.4. Even if the surface of the host vehicle is in the FOV of the camera, without proper lighting, the camera will not be able to take observable images. When available, utilizing sunlight to take photographs is preferable to using a flash illuminator, which would otherwise unnecessarily drain the battery. Additionally, the angle of incidence of the sunlight on the surface of the host must be sufficient.

A figure of merit which falls under the category of lighting is the availability of sunlight for image capturing. The three conditions that must be met to determine this are:

1. Sunlight illuminates the surface being viewed
2. The point is not in the shadow of the host itself
3. The point is not in the shadow of the Earth

Figure 3-23 provides an illustration of the vectors used in the calculation to determine if conditions 1 and 2 are met.

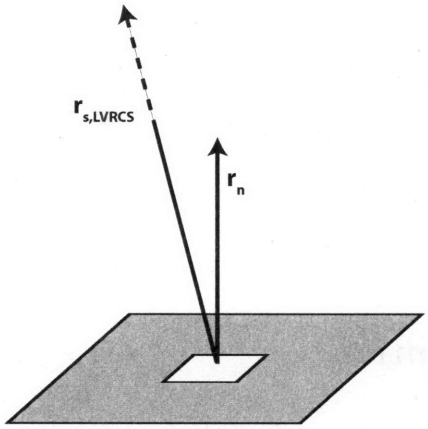

Figure 3-23: Host Surface Normal Vector and Sun Vector

With $\boldsymbol{r}_{s,LVRCS}$ as the Sun vector in the LVRCS, and all other variables as in Section 3.7.2, the calculation to demonstrate that the point is illuminated by the Sun and not in the shadow of the host is as follows:

$$\boldsymbol{r}_{s,LVRCS} \cdot \hat{\boldsymbol{r}}_n > 0$$

Figure 3-24 illustrates Earth's shadow and the position of the point on the surface being imaged. R_e represents the mean radius of the Earth.

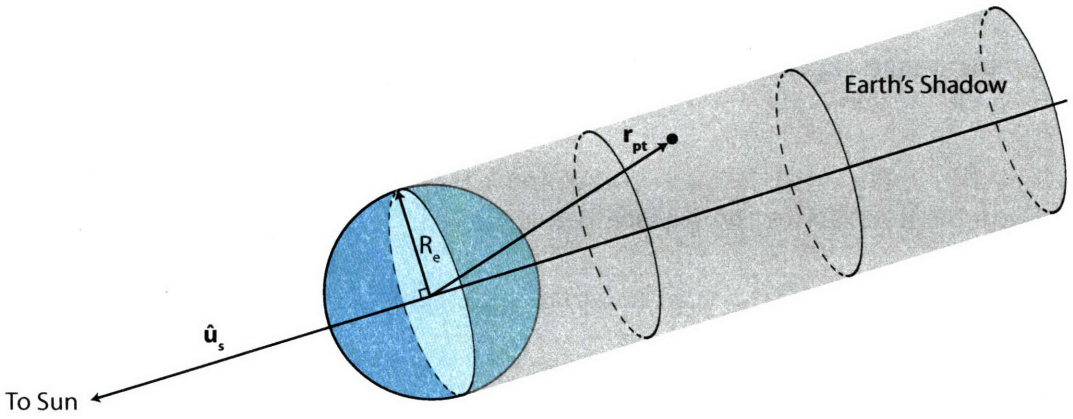

Figure 3-24: Geometry of Earth's Shadow

Based on the variables defined in this figure, the point is in the shadow of the Earth if:

- $\boldsymbol{r}_{pt} \cdot \hat{\boldsymbol{u}}_s < 0$
- $|\boldsymbol{r}_{pt} \cdot \hat{\boldsymbol{u}}_s| < R_e$

3.7.6 Image Resolution

The images taken by the camera on board the microinspector vehicle are beneficial only if the quality is acceptable. Consequently, the resolution of the image is a crucial figure of merit to evaluate the inspection mission. The image resolution for a point on the host's surface can be calculated by:

$$\text{Resolution} = r_{c,pt} \tan\left(\frac{\theta_{aov}}{N}\right) \tag{3.35}$$

$r_{c,pt}$ is the distance from the camera to the point on the host's surface, θ_{aov} is the camera's angle of view, and N is the number of pixels in the array.

3.7.7 Pixel Smear

The requirement on the minimum pixel smear directly impacts the maximum relative velocity of the microinspector. In Section 2.2, a requirement of less than one pixel

was given. This translates to keeping the relative velocity below a certain threshold during the inspection, such that within an exposure time, an image does not spread over more than one pixel.

To achieve this requirement, the maximum tangential relative velocity of the microinspector for a camera exposure time of t_{et} is given by:

$$v_{max} = \frac{r_{c,pt} \tan\left(\frac{\theta_{aov}}{N}\right)}{t_{et}} \tag{3.36}$$

where $r_{c,pt}$, θ_{aov}, and N are as before in Section 3.7.6.

3.7.8 Battery Reserve

The amount of battery power available at any given time is an important figure of merit. If the battery reserves are drained below a certain limit, the microinspector will need to stop its current task and point the solar cells towards the Sun to recharge. This also impacts fuel expenditure, as well as any time constraints. At any given time, the battery reserves can be roughly determined by:

$$\text{Battery Reserves}\,(W \cdot hr) = B_0 + 25 \int_{t_0}^{t} \left[\cos(\phi_{sa}) - \cos(\phi_{sa,max})\right] dt \tag{3.37}$$

where B_0 is the battery reserve at t_0.

(This Page Intentionally Left Blank)

Chapter 4

Design Description

The strategies presented in Chapter 3 allow a straightforward mission design for a microsatellite inspector in a planet orbiting environment. The idea of utilizing natural dynamics in designing the trajectory was found to use extremely minimal fuel. In addition, the *CW* solution provides an easy method for calculating the positions, velocities, and accelerations for natural trajectories. Thus, in this chapter, a list of some of the natural relative trajectories that may be advantageously employed in a visual inspection mission is presented. These trajectories form a toolset that a mission planner can use in building an inspection mission. Methods and fuel usage for transferring from one type of trajectory to another is discussed. Methods used to estimate fuel usage for rotational motion and station-keeping are also examined. Finally, a baseline mission description for a microinspector utilizing the design strategies and the trajectory toolset is presented.

4.1 Toolset

This section recounts some of the natural relative motion presented thus far, as well as introducing a new set of trajectories that may be exploited in designing an inspection mission. An analysis of each trajectory is conducted on the basis of fuel usage, application to imaging, and time span, all in the LVRCS. The velocity magnitude of each of the following trajectories is much less than the maximum Δv that would be

available on a microsatellite inspector.

4.1.1 Stationary on V-bar

One option for inspection is to place the microinspector behind or in front of the host, along the V-bar, as shown in Figure 4-1. Examples of this type of trajectory were already given in Figures 2-8, 3-11, and 3-18. In the LVRCS, the camera can be directed to point toward the host. If the host is equipped with solar arrays or solar sails, the microinspector can capture the deployment phase while in this stationary position, relative to the host. Another application would involve the cooperation of the host vehicle. The host spacecraft can rotate about different axes in the LVRCS allowing the microinspector to take images of the host until complete coverage is achieved. This stationary position may also be utilized as an intermediary point before embarking on the remainder of the inspection mission. In terms of the traveling ellipse parameters from Section 3.1.2, Y_0 defines where the microinspector is located on the V-bar relative to the host. All other parameters are set to a value of zero. Once the microinspector is put on the V-bar near the host vehicle with zero relative velocity, the microinspector stays at the position indefinitely, with fuel being used only for orbit maintenance.

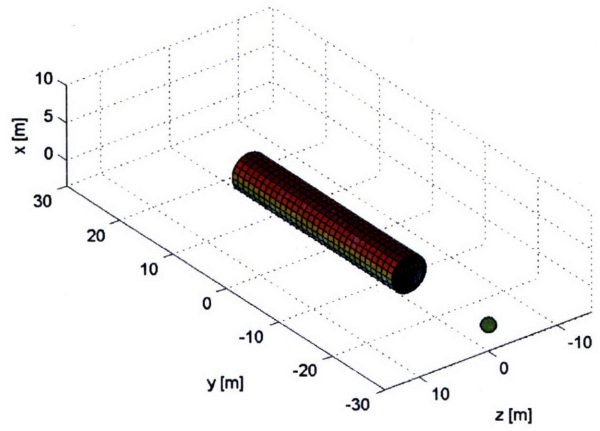

Figure 4-1: Stationary on V-bar

4.1.2 Out-of-plane Oscillation across the V-bar

The microinspector can also be made to oscillate out-of-plane, while positioned on the V-bar. The out-of-plane magnitude is defined by the traveling ellipse parameter, c. As in Section 4.1.1, the position on the V-bar is designated by the value of Y_0. Figure 4-2 portrays an out-of-plane motion, with $c = 10\,m$, which requires a velocity burn of $\Delta v = 0.00996\,m/s$, from a zero-velocity state on the V-bar. An out-of-plane motion with a magnitude of $c = 20\,m$ requires $\Delta v = 0.01992\,m/s$. The larger the magnitude, the greater the initial velocity needs to be to insert the microinspector into this oscillatory motion. If the length of the host spacecraft lies out-of-plane as in the figure, the advantage of the out-of-plane natural motion becomes apparent. Placed in this oscillatory motion, the microinspector can take images of the entire length of the host vehicle.

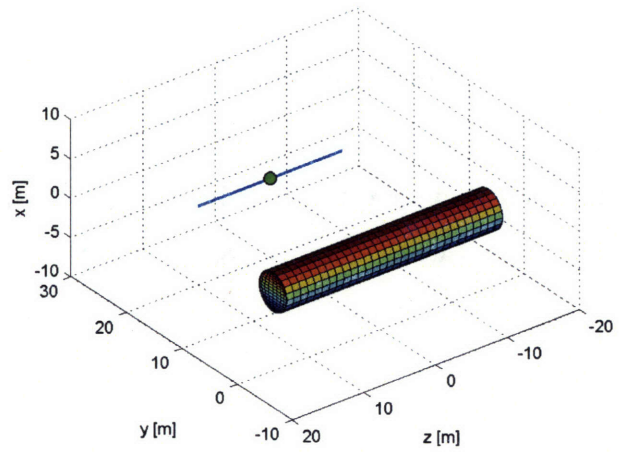

Figure 4-2: Out-of-plane on V-bar

4.1.3 In-plane 2×1 Ellipse

The 2×1 elliptical motion, also known to the GN&C community as a *football orbit*, was introduced in the previous chapters. The in-plane 2×1 ellipse is a stationary relative closed orbit, which was illustrated in Figures 2-7 and 3-10–3-12. The position of an in-plane 2×1 ellipse along the V-bar may vary depending on the mission requirements.

The cases presented next are considered to be basic to the trajectory toolset for an inspection mission.

Center at Origin

An in-plane 2×1 ellipse presents a stable and fuel-minimizing method of traveling about the host vehicle. The attitude of the microinspector can be regulated so that the camera's boresight vector is fixed in the inertial reference frame, as discussed in the example in Section 3.5.1. Once the microinspector is inserted into this stationary ellipse, no further fuel is needed to continue the motion about the host vehicle. Hence, the in-plane 2×1 ellipse is not only an excellent choice for an inspection trajectory, it is also an ideal trajectory to be put into during intervals of non-imaging.

Figure 4-3 illustrates an in-plane 2×1 ellipse, in which $b = 20\,m$ and $Y_0 = 0\,m$. All other traveling ellipse parameters are set to zero. The velocity burn for insertion is $\Delta v = 0.022\,m/s$, from a zero-velocity state at 40 or -40 m on the V-bar. The velocity magnitude during a 2×1 ellipse is minimum where the ellipse intersects the V-bar (y-axis) and maximum where it intersects the R-bar (x-axis). An ellipse that is twice the size of the one in Figure 4-3 would require double the Δv for insertion. The time for one revolution about the host vehicle is the same as the orbital period of the host.

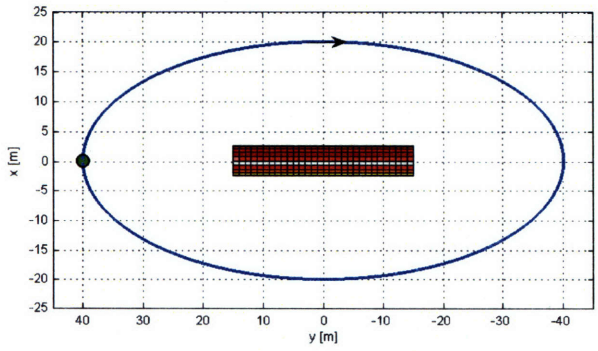

Figure 4-3: In-plane 2×1 Ellipse: Center at Origin

Off-center Ellipse

The center of the in-plane 2×1 ellipse can be offset along the V-bar as shown in Figure 4-4. This type of trajectory has advantages similar to the previous case. It may be utilized for inspection of the host spacecraft or for placing the microinspector in a stable relative motion during intervals of non-imaging. The velocity magnitude needed to insert the microinspector into the trajectory is $\Delta v = 0.012\, m/s$.

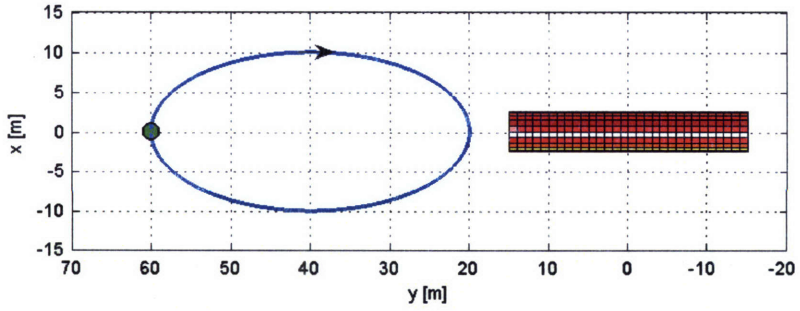

Figure 4-4: In-plane 2×1 Ellipse: Center Not at Origin

Intersecting Ellipse

The center of the in-plane 2×1 ellipse can be offset along the V-bar as shown in Figure 4-5, such that the trajectory intersects with the host vehicle. Although this type of trajectory is not suited for inspection purposes due to the danger of collision, using a portion of the trajectory is certainly a valid method for initially deploying the microinspector. One can envision the microinspector leaving the host, traveling along this trajectory, and stopping once it reaches the V-bar. In the figure, the dot represents the initial position of the microinspector attached to the host. Also, the complete trajectory — when the microinspector is not stopped at the V-bar — is shown. The velocity magnitude needed to insert the microinspector into the trajectory is $\Delta v = 0.012\, m/s$.

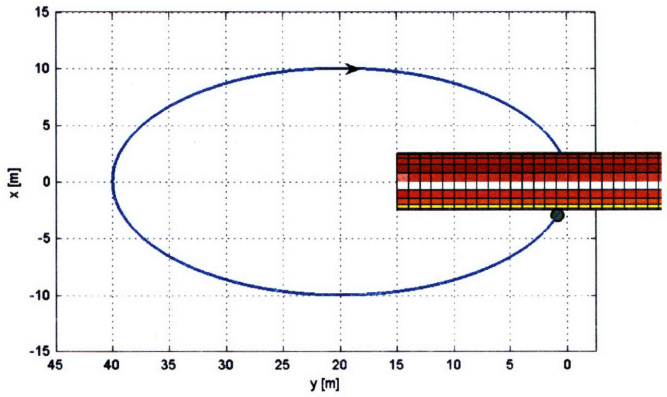

Figure 4-5: In-plane 2×1 Ellipse: Intersecting Ellipse

4.1.4 Inclined 2×1 Ellipse

Examples that involved an inclined 2×1 ellipse were illustrated in Figures 2-9, 3-3, 3-12–3-13, and 3-19. Similar to the in-plane 2×1 ellipse case, this type of trajectory allows for a stable and fuel minimal method of orbiting about or near the host vehicle. The form of the trajectory is still a 2×1 ellipse in-plane. The inclined portion of the trajectory comes directly from the addition of the out-of-plane oscillatory motion to the in-plane 2×1 ellipse. A variety of inclined 2×1 ellipses may be formed specific to the inspection mission, by varying the values for b, c, Y_0, and $\psi - \phi$. X_0 must be zero for the relative orbit to stay stationary. In this study, two distinct forms of the inclined 2×1 ellipse are presented for their natural benefits in visual inspection.

Circular in x-z Plane

Figure 4-6 displays an inclined (about the R-bar) 2×1 ellipse that is circular when viewed along the V-bar, in the x-z plane of the LVRCS. To obtain such a relative orbit, the value for b and c must be equal. Additionally, $\psi - \phi = 90°$. For a host vehicle with its length along the V-bar, this type of trajectory permits the microinspector to get closer to the surface and take images with better resolution, with minimal risk of collision. The size of the inclined ellipse can be made much smaller than an in-plane ellipse, in part because of the out-of-plane factor and also due to the ellipse

intersecting the R-bar instead of the V-bar. In effect, the value for the semiminor axis, b, has more flexibility. The camera's boresight vector can be initiated to rotate in the plane of the ellipse, as in Figure 3-12. Another practical option is to direct the attitude of the microinspector, so that the camera's boresight vector is normal to the V-bar, as in Figure 3-13. The velocity magnitude of this inclined 2×1 ellipse at $\phi = 0°$ and $\phi = 180°$ is the same as its in-plane counterpart: $v = 0.011\, m/s$. At $\phi = 90°$ and $\phi = 270°$, the velocity magnitude of the microinspector is $v = 0.025\, m/s$. Again, the period of the inclined 2×1 ellipse is equal to the orbital period of the host.

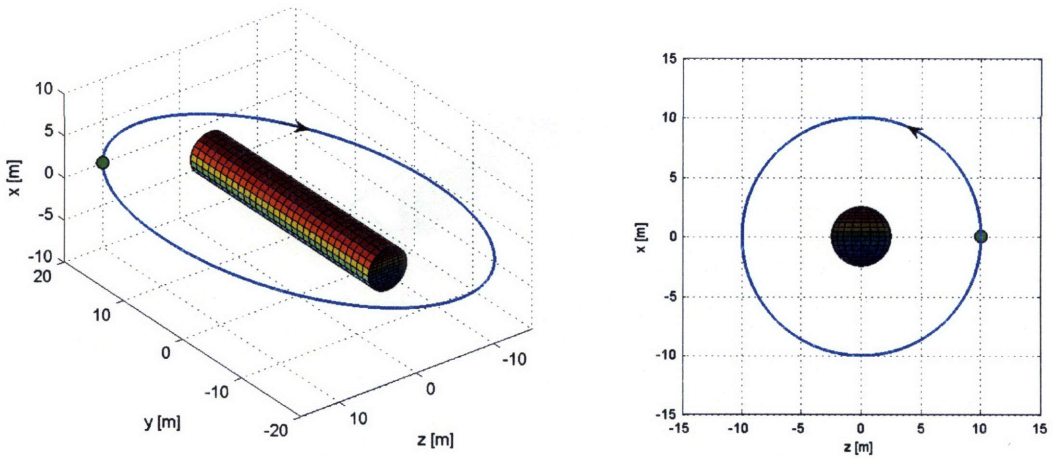

(a) 3D (b) Front View (x-z View)

Figure 4-6: Inclined 2×1 Ellipse: Circular in x-z Plane

Because the trajectory does not intersect the V-bar, even if some drift occurs along the V-bar due to differential perturbing accelerations, there is no chance of collision. Thus, this motion is safe in terms of collision and easy to maintain.

Circular in Orbital Plane

The x-y plane view of an inclined 2×1 ellipse always has the 2×1 form. But in the orbital plane of the relative trajectory, the shape can be varied dramatically. Figure 4-7 illustrates one particular trajectory that can be achieved. The inclined (about the V-bar) ellipse is such that the motion is circular about the center of the relative orbit, and the trajectory intersects the V-bar. For a given value of b, setting $c = \pm b\sqrt{3}$

and $\psi - \phi = 0°$ gives the circular form in the relative orbital plane. The camera's boresight vector can be controlled to rotate in this plane, while pointing toward the center of the circular relative motion. The microinspector is equidistant from this center throughout its motion, which may be beneficial to some inspection missions. These circular relative orbits, however, are always inclined 60° from the in-plane, possibly restricting their use. Since the orbit intersects with the V-bar, the danger of collision is also increased if the microinspector is close to the host.

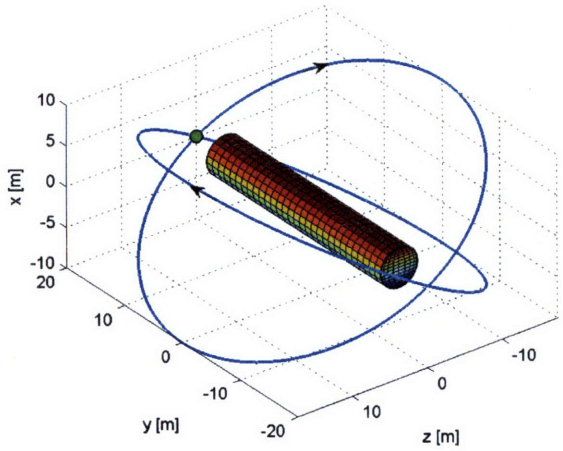

Figure 4-7: Inclined 2×1 Ellipse: Circular in Orbital Plane

4.1.5 Horizontal Above/Below

The *CW* solution shows that the microinspector can be made to move in a relative straight line above or below the host in-plane. This type of motion can be used to view the top or bottom of the host vehicle at a constant distance from the V-bar, if the host is not rotating in the LVRCS. Also, a nonzero value for c will result in an out-of-plane sinusoidal motion. Figure 4-8 shows what this type of motion looks like, relative to the host vehicle, which maintains a LVLH attitude. The velocity magnitude needed to set the microinspector to traverse in a straight line depends on the position deviation along the R-bar (x-axis), and is given by Eqn 4.1. The velocity is applied parallel to the V-bar, which makes the microinspector appear to

move above or below the host vehicle depending on the sign of the radial deviation from the host.

$$v = -\frac{3}{2}x_0\omega \tag{4.1}$$

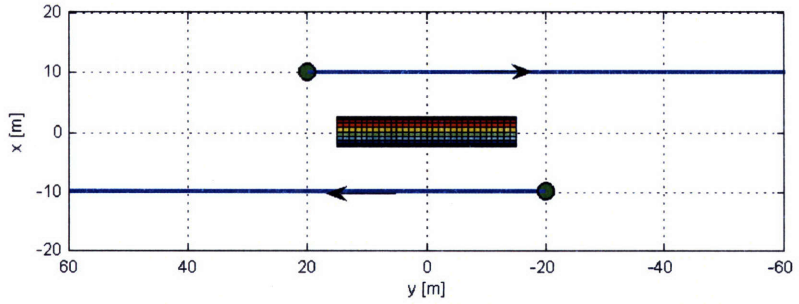

Figure 4-8: Horizontal Motion Above/Below Host Vehicle

4.1.6 In-plane Traveling Ellipse

The traveling ellipse was first introduced in Section 3.1.2, Figure 3-4. This relative motion occurs when the center of the stationary ellipse along the radial vector is not located on the V-bar of the host spacecraft. In traveling ellipse parameters, the value of X_0 is nonzero. By shifting the center of the original 2×1 ellipse up or down along the radial axis, the ellipse appears to move backwards or forwards, respectively. In general, a drifting ellipse in-plane is usually an undesirable phenomenon due to possible collision with the host.

Inserting the microinspector into an in-plane traveling ellipse trajectory is an effective method of disposing the vehicle once the inspection mission is completed. Figure 4-9 illustrates two instances of the microinspector leaving its initial stationary position on the V-bar via a traveling ellipse. The fuel needed to enter such a trajectory is extremely small compared to the total fuel on board a microinspector.

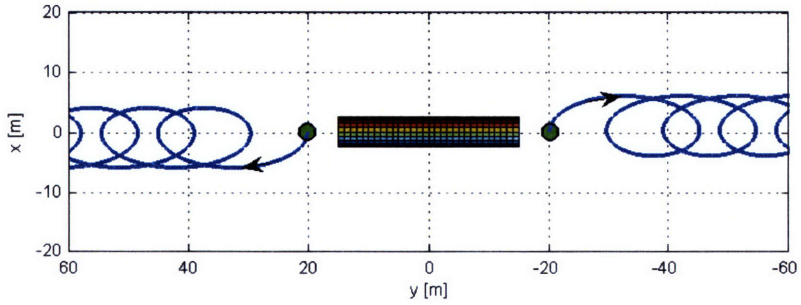

Figure 4-9: In-plane Traveling Ellipse

4.1.7 Spiral Orbit

The spiral orbit is essentially an inclined traveling ellipse. Given the right set of conditions, the microinspector can be made to drift along the V-bar in a spiraling loop with no further use of fuel, as shown in Figure 4-10. In this particular figure, the host is in a circular orbit about the Earth at an altitude of $500\,km$. The initial velocity magnitude of the spiral orbit is $v = 0.011\,m/s$ from a zero velocity state. The spiral orbit can be initiated from a corresponding inclined 2×1 ellipse. By applying a Δv parallel to the V-bar, the microsatellite can be made to spiral forwards or backwards. The effect of applying Δv parallel to the V-bar is elaborated further in Appendix B. The camera's boresight vector can point toward the host's surface, much like in Section 4.1.4, throughout the orbit. This is an excellent method of capturing images of the host's surface, while using very little fuel. For host vehicles, whose length is along the V-bar, this method can be used to inspect most of the host's surface. Similar to the first case (circular in x-z plane) in Section 4.1.3, there is no chance of collision as the microinspector travels along the spiral trajectory. Thus, the motion is safe in the presence of disturbing differential accelerations. While traveling forwards or backwards, there is no possibility of collision. As seen in Figure 4-10b, the spiral trajectory forms a tunnel around the host vehicle. Each loop of the spiral orbit is approximately one orbital period. The values for b, c, X_0 and $\phi - \psi$, which determine the size and shape of the spiral, will depend on the camera specifications and image requirements.

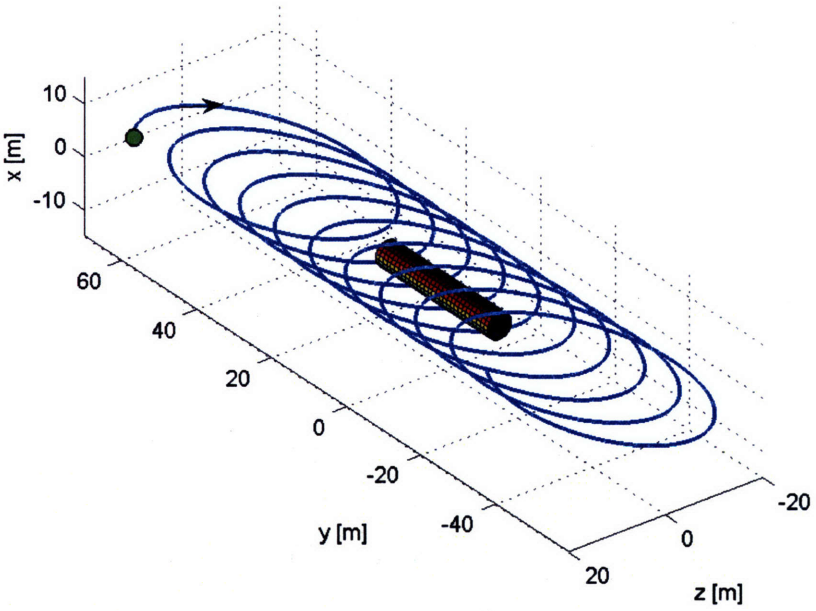

(a) 3D

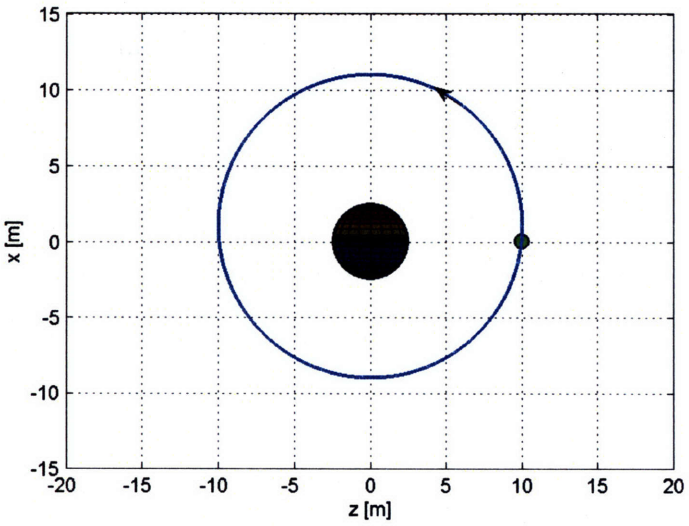

(b) Front View

Figure 4-10: Spiral Orbit

4.1.8 Tear-drop Orbit

This trajectory is so named because of its tear-drop shape. The trajectory is actually just a segment of one revolution of the traveling ellipse; however, the ease in which the tear-drop form can be kept with periodic maintenance makes it a useful trajectory to include in the toolset. The time to traverse a tear-drop orbit is less than one orbital period, since it is a section of the traveling ellipse. Thus for missions that are constrained in time, utilizing tear-drop orbits may be a practical choice, with the trade-off being periodic fuel expenditure.

Tear-drop About Host

The shape and the position of the tear-drop orbit may be chosen to encircle the host vehicle, as illustrated in Figure 4-11. The motion of the microinspector is purely in-plane. Without the Δv burn at the point of intersection of this tear-drop orbit, the microinspector will follow the path of a traveling ellipse. The "period" or Δt_{td} of this tear-drop orbit is about 95% of the orbital period of the host. $\Delta v \cong 0.005\, m/s$, which is applied in the negative x-direction every Δt_{td}. In Section 3.5.1, the camera's boresight vector was rotated in the LVRCS to capture images of the host vehicle. Since Δt_{td} is less than the orbital period, the boresight vector needs to be rotated at a constant angular rate of $\frac{2\pi}{\Delta t_{td}}\, rad/s$. The deviation of the ellipse's center is positive along the radial axis in Figure 4-11. If the deviation is negative, then the microinspector would move along a traveling ellipse path in the opposite direction. The Δv burn would then have to be applied in the positive x-direction to achieve a tear-drop orbit about the host vehicle.

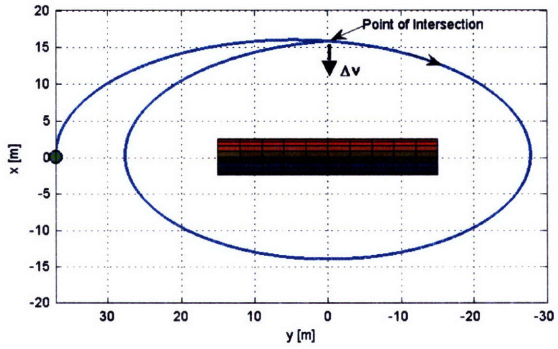

Figure 4-11: Tear-drop Orbit About Host (In-plane)

The tear-drop orbit may also be designed to have an out-of-plane component. Because the out-of-plane motion is sinusoidal with a period equaling the orbital period of the host vehicle and Δt_{td} is less than the orbital period, the out-of-plane location of Δv will vary from burn to burn. Over time, the tear-drop orbits form a set that stays within a band defined by the out-of-plane traveling ellipse component, c. The motion is akin to a lissajous figure in three dimensions. Figure 4-12 displays the same in-plane tear-drop shape from Figure 4-11, but with an out-of-plane component of $c = 3\,m$. The Δv burns are equivalent in magnitude and direction.

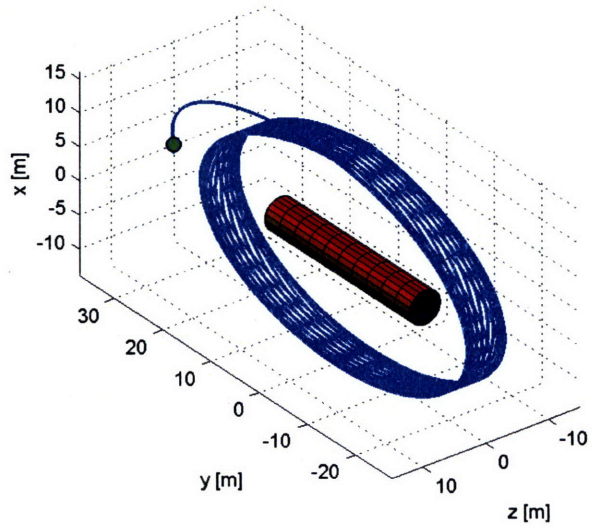

Figure 4-12: Tear-drop Orbit About Host (3D)

Tear-drop Near Host

The tear-drop orbit can also be formed near the host vehicle as in Figure 4-13. This type of trajectory can be utilized to take an image of a particular point on the host vehicle, without resorting to station-keeping. Station-keeping at a position above or below the host would require much more fuel consumption, than this tear-drop orbit. Since only one snapshot of the point on the surface is needed to determine if the vehicle has been damaged, the tear-drop trajectory, such as the one in Figure 4-13 will suffice. It is not necessary to continue traveling about the tear-drop shape, and thus extra burns are not needed. Nevertheless, if it is desired to have the microinspector travel about the tear-drop orbit as in Section 4.1.8, then similarly a Δv burn is required each time the microinspector reaches the point of intersection. The smaller the tear-drop orbit becomes, the closer the total Δv is to the fuel for station-keeping at the limiting point. This is one method for mechanizing the station-keeping method.

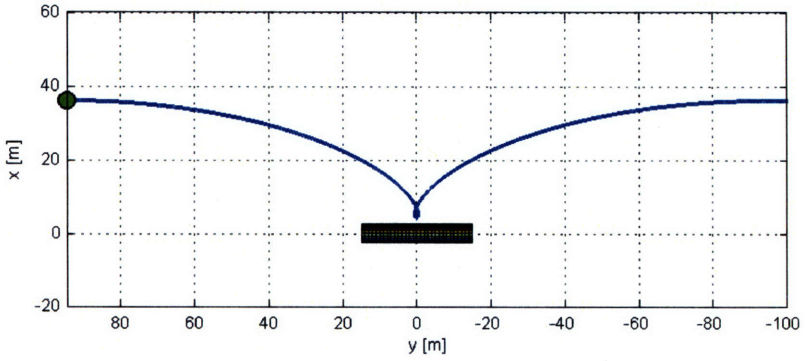

Figure 4-13: Tear-drop Orbit Near Host

Notice that the tear-drop shape can be eliminated altogether, to form a dip in place. Figure 4-14 illustrates this trajectory.

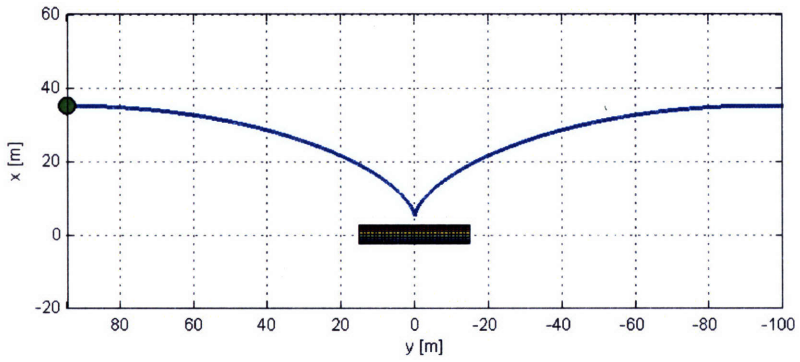

Figure 4-14: Dip Near Host

4.2 Trajectory Transfer and Location of Translational Δv Burns

Before the natural motions presented in the toolset from Section 4.1 can be utilized to piece together a mission, it is necessary to list the possible transfers from one type of motion to another. Figure 4-15 portrays a flowchart of the natural motions from the toolset and the transfers between them. Many of the trajectories listed in the toolset are subsets of the inclined 2×1 ellipse and the inclined traveling ellipse. Thus, in the flowchart, the trajectories that proceed from these categories are shown in the dashed boxes. All of the trajectories in the flowchart are natural motion, except for the tear-drop orbits, which lead to station-keeping.

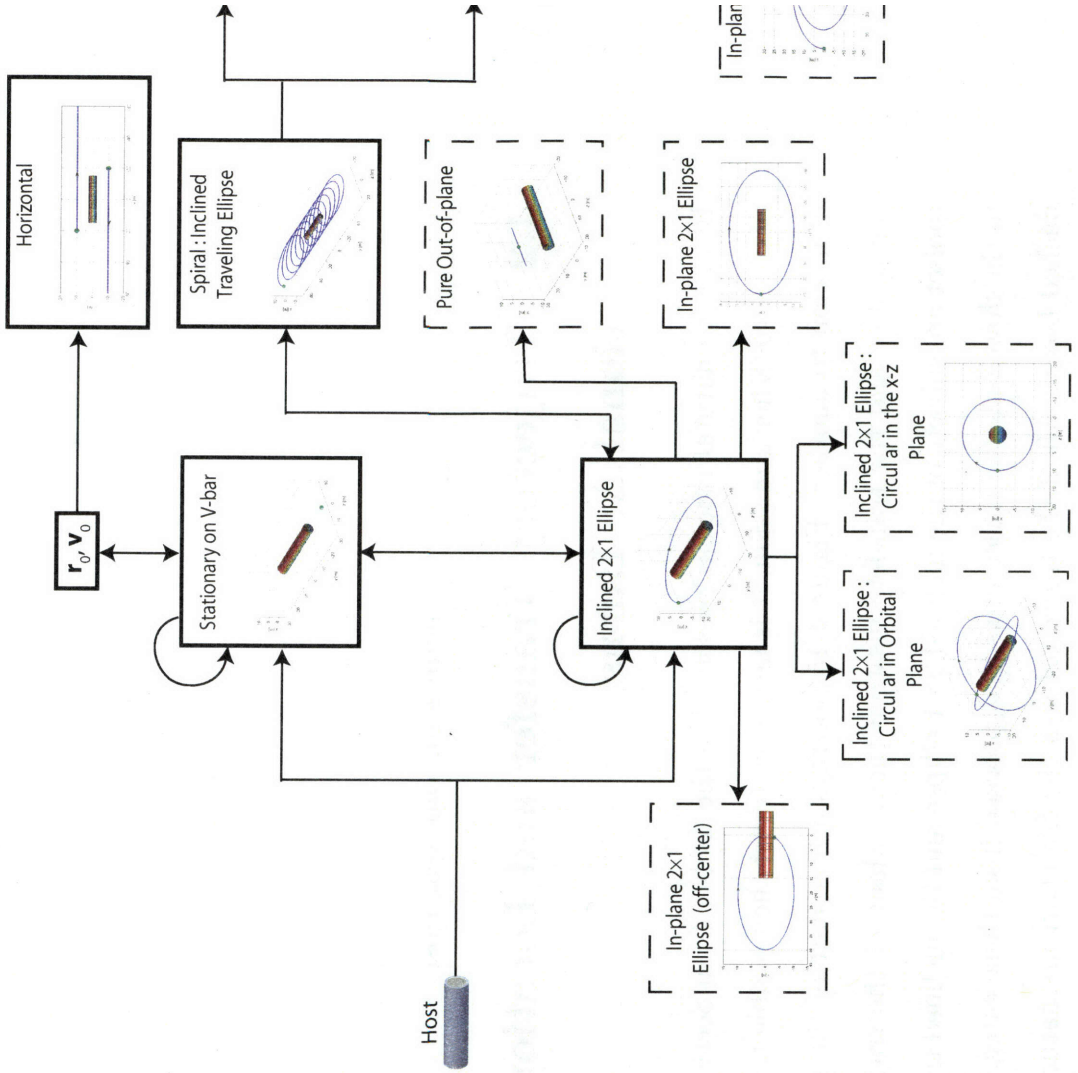

Figure 4-15: Transfer Trajectory Flowchart of Toolset

There are a variety of methods of computing the transfer trajectories to maneuver from one natural relative motion to another. The forced motion method discussed in Section 3.4 can be employed in this case to insert the microinspector into the desired natural motion. However, this method is expensive in terms of fuel usage compared to the use of natural dynamics. Hence, the transfer trajectories for the simulations in this thesis will be computed using the natural relative dynamics described by the *CW* solution. This section presents a description of several of the transfer trajectory computations. Based on these computations, a set of positions, impulse velocities, and times, which describe the natural motions and the transfers, are compiled into an input array that is used by the mission simulation. Figure 4-16 illustrates the general legend for the graphics in this section.

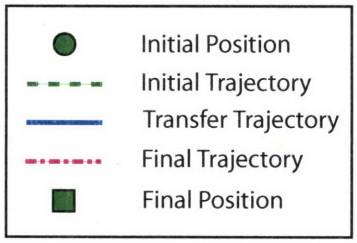

Figure 4-16: Legend for Transfer Trajectory Graphics

4.2.1 V-bar $\Longrightarrow$ V-bar

Table 4.1 describes the variables that are used to compute the transfer trajectory between two positions on the V-bar. The initial relative velocity at $\boldsymbol{r}_i$ is assumed to be zero.

Table 4.1: V-bar $\Longrightarrow$ V-bar: Computational Variables

Variable	Description
$\boldsymbol{r}_i$	Initial position vector (on V-bar)
t_i	Time at $\boldsymbol{r}_i$
$\boldsymbol{r}_f$	Desired position vector (on V-bar)
ω	Orbital rate of host
$\boldsymbol{d}$	Differential acceleration vector
box	Dimensions of box constraint

1. If $\boldsymbol{r}_i = \boldsymbol{r}_f$, then no transfer trajectory is needed.

2. If $\boldsymbol{r}_i \neq \boldsymbol{r}_f$, then the transfer trajectory can be computed using the traveling ellipse formulation of the *CW* solution. The trajectory is a half-segment of an in-plane 2×1 ellipse that connects the two positions. This in-plane 2×1 ellipse is determined by the following traveling ellipse parameters:

$$b = \frac{|\boldsymbol{r}_i - \boldsymbol{r}_f|}{4} \tag{4.2}$$

$$Y_0 = \frac{\boldsymbol{r}_i + \boldsymbol{r}_f}{2} \tag{4.3}$$

The value for the in-plane phase angle, ϕ, is either 0° or 180°, depending on the initial and final positions. All other traveling ellipse parameters for the ellipse are zero. With these parameters, the Δv to start the transfer trajectory can be computed by Eqn 3.9. The desired position on the V-bar is reached after half the orbital period, at which point an equivalent Δv is applied to stop the elliptical motion. Figure 4-17 illustrates this type of transfer trajectory. The circle represents the initial position and the square designates the final desired position on the V-bar.

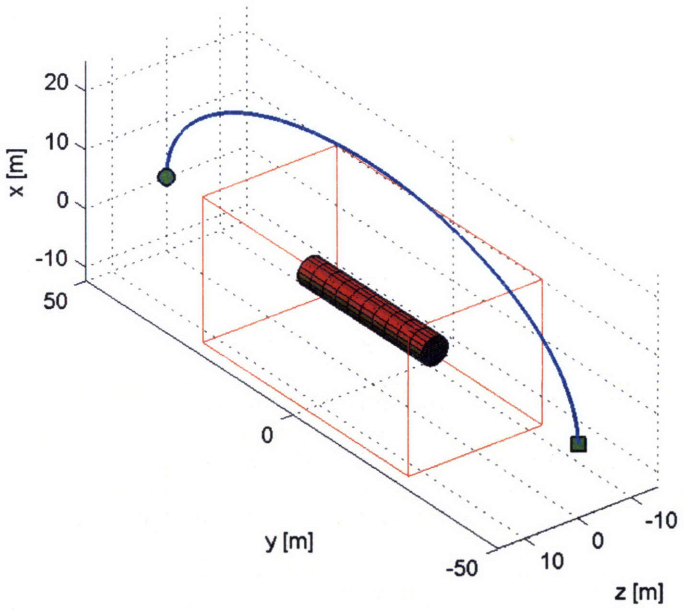

(a) 3D View

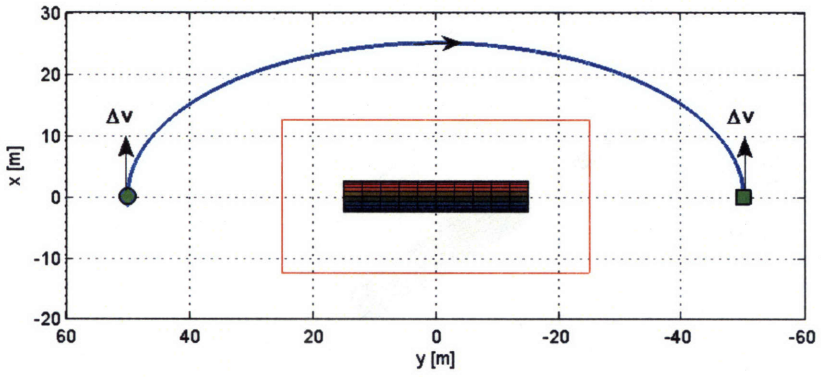

(b) Side View (in-plane)

Figure 4-17: V-bar $\Longleftrightarrow$ V-bar

3. If the transfer trajectory from 2 violates the avoidance constraints, alternative measures need to be taken. The microinspector can be sent to an intermediary position(s) on the V-bar, where the constraints are not violated traveling to this position from the initial position. Additionally, the trajectory from the last intermediary position to the desired position must also observe the avoidance constraints. One way of calculating the intermediary position(s) is by using the dimensions of the constraints. Based on the constraint dimensions, two points can be chosen to form an elliptical transfer trajectory that stays outside the keep-out zone. Section 3.2 explained how to determine values for b and Y_0 given two points on the 2×1 ellipse. The transfer trajectory to go from the initial position to this constraint-avoiding 2×1 ellipse can be calculated according to Eqns 4.2–4.3 from before. Likewise, the transfer trajectory from this intermediary ellipse to the final desired position on the V-bar can also be determined. The Δv's for each segment of the total transfer trajectory can be determined from Eqn 3.9. A transfer trajectory that is computed with the avoidance constraints incorporated is shown in Figure 4-18.

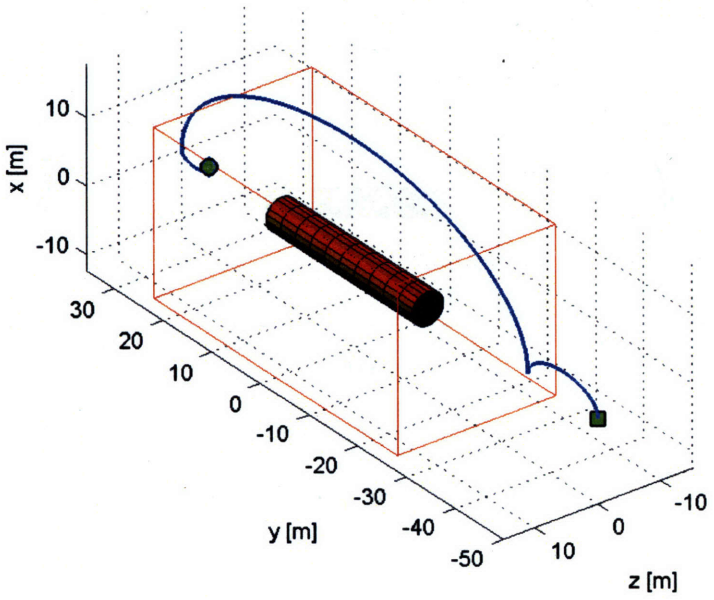

(a) 3D View

Figure 4-18

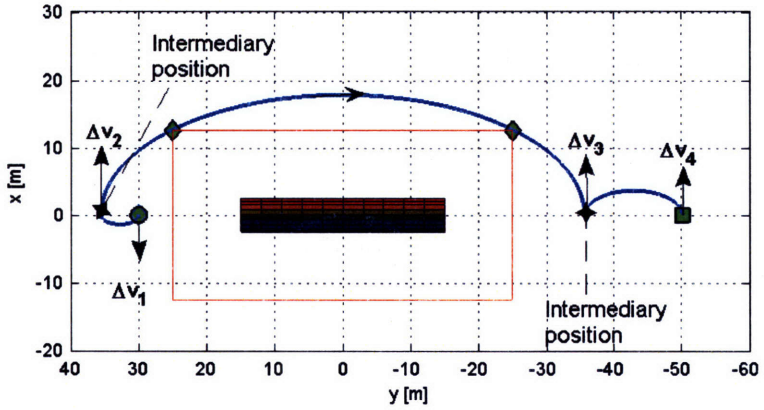

(b) Side View (in-plane)

Figure 4-18: V-bar $\Longleftrightarrow$ V-bar with Avoidance Constraint

4.2.2 V-bar $\Longleftrightarrow$ 2×1 Ellipse

Tables 4.2–4.3 describe the variables that are used to compute the transfer trajectory between a position on the V-bar and a 2×1 ellipse. The relative velocity at the position on the V-bar is assumed to be zero.

Table 4.2: V-bar $\Longrightarrow$ 2×1 Ellipse: Computational Variables

Variable	Description
$\boldsymbol{r}_i$	Initial position vector (on V-bar)
t_i	Time at $\boldsymbol{r}_i$
b	Semiminor axis of desired 2×1 ellipse
c	Out-of-plane component of desired 2×1 ellipse
Y_0	Center of desired 2×1 ellipse on y-axis
θ	$\psi - \phi$ for desired 2×1 ellipse
ω	Orbital rate of host
$\boldsymbol{d}$	Differential acceleration vector
box	Dimensions of box constraint

Table 4.3: 2×1 Ellipse $\Longrightarrow$ V-bar: Computational Variables

Variable	Description
$\boldsymbol{r}_i$	Initial position on 2×1 ellipse
$\boldsymbol{v}_i$	Initial velocity on 2×1 ellipse
t_i	Time at $\boldsymbol{r}_i$
$\boldsymbol{r}_f$	Desired position vector (on V-bar)
ω	Orbital rate of host
$\boldsymbol{d}$	Differential acceleration vector
box	Dimensions of box constraint

1. To traverse from a position on the V-bar to a 2×1 ellipse, first the microinspector is inserted into the in-plane 2×1 ellipse, corresponding to the desired 2×1 ellipse. This in-plane 2×1 ellipse has the same traveling ellipse values as the desired 2×1 ellipse, except $c = 0$. Obviously, if the desired 2×1 ellipse is an in-plane trajectory, then the two elliptical trajectories are equivalent. The method explained in Section 4.2.1 can be utilized to send the microinspector to $\phi = 0°$ or $\phi = 180°$ of the in-plane 2×1 ellipse, which is located on the V-bar. Once that position on the V-bar is reached, an appropriate Δv can be applied to direct the microinspector into the in-plane 2×1 ellipse. If the desired 2×1 ellipse is inclined, then at the location where the in-plane 2×1 ellipse and the inclined 2×1 ellipse intersect, another Δv in the out-of-plane direction can be fired to insert the microinspector into the desired 2×1 ellipse. The Δv's are calculated directly from Eqn 3.9. Figure 4-19 illustrates an example of this transfer and the direction of the impulse velocities for this particular case.

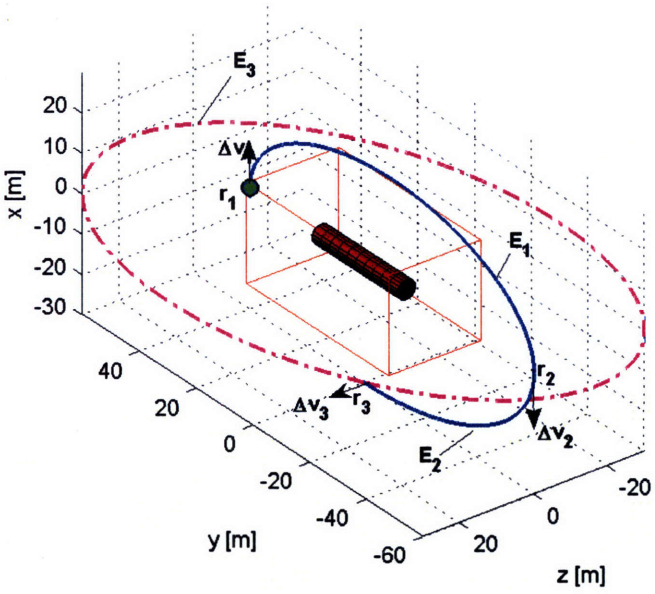

(a) 3D View

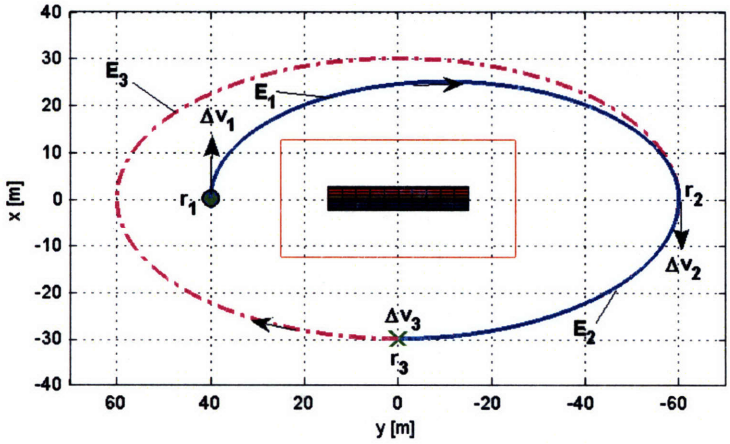

(b) Side View (in-plane)

Figure 4-19: V-bar $\Longleftrightarrow$ 2×1 Ellipse

Because natural relative motion is used to design the transfer trajectories, it is ensured that fuel is conserved. Notice that the transfer trajectory requires a total of three Δv burns. The first impulse velocity, $\Delta \boldsymbol{v}_1$, is applied to transfer from the initial position on the V-bar to the position designated by $\phi_2 = 180°$ of the in-plane 2×1 ellipse, which has the same b and Y_0 as the desired inclined 2×1 ellipse. Calling this corresponding in-plane 2×1 ellipse, E_2, it is noted that this trajectory intersects with the desired inclined 2×1 ellipse, E_3. $\boldsymbol{r}_2$, the position at $\phi_2 = 180°$, can be computed simply by setting $t = 0$, $\phi_2 = 180°$, b and Y_0 values to be the same as for the desired 2×1 ellipse, and all other traveling ellipse parameters to zero in Eqn 3.8. The equation is then given by:

$$\boldsymbol{r}_2 = \begin{bmatrix} b\sin(\phi_2) \\ Y_0 + 2b\cos(\phi_2) \\ 0 \end{bmatrix} \tag{4.4}$$

The traveling ellipse parameters, b_1 and Y_{01} that describe the in-plane 2×1 ellipse that connects $\boldsymbol{r}_i$ and $\boldsymbol{r}_2$ can be computed using Eqn 4.2–4.3. Let this connecting in-plane 2×1 ellipse be denoted by E_1. At $\boldsymbol{r}_i$, the phase angle on E_1 is $\phi_1 = 0°$. Then, $\Delta \boldsymbol{v}_1$ can be computed as follows:

$$\Delta \boldsymbol{v}_1 = \begin{bmatrix} b_1\omega\cos(\omega t_i + \phi_1) \\ 2b_1\omega\sin(\omega t_i + \phi_1) \\ 0 \end{bmatrix} \tag{4.5}$$

$\Delta \boldsymbol{v}_2$ is applied at $\boldsymbol{r}_2$ to insert the microinspector into E_2. To determine the second impulse velocity, the velocity at $\boldsymbol{r}_2$ on E_1, $\boldsymbol{v}_{2p}$, and the desired velocity on E_2, $\boldsymbol{v}_{2a}$, must be known. $\Delta \boldsymbol{v}_2$ is applied after the microinspector has traveled half-way through the previous in-plane 2×1 ellipse at $t_2 = t_i + P/2$. Thus, $\boldsymbol{v}_{2p}$ can be calculated by Eqn 4.6.

$$\boldsymbol{v}_{2p} = \begin{bmatrix} b_1\omega\cos(\omega t_2 + \phi_1) \\ 2b_1\omega\sin(\omega t_2 + \phi_1) \\ 0 \end{bmatrix} \tag{4.6}$$

At $\boldsymbol{r}_2$, the desired velocity, $\boldsymbol{v}_{2a}$, can be calculated by setting $t = 0$ and $\phi_2 = 180°$ for E_2. Eqn 4.7 shows the exact formula.

$$\boldsymbol{v}_{2a} = \begin{bmatrix} b\omega\cos(\phi_2) \\ 2b\omega\sin(\phi_2) \\ 0 \end{bmatrix} \tag{4.7}$$

The second impulse velocity is then given by:

$$\Delta\boldsymbol{v}_2 = \boldsymbol{v}_{2a} - \boldsymbol{v}_{2p} \tag{4.8}$$

Finally, the third impulse velocity is applied at the first location where E_2 and E_3 intersect, denoted by $\boldsymbol{r}_3$. This position is located at either $\phi_3 = 2\pi - \theta$ or $\phi_3 = \pi - \theta$ on E_3. For the example in Figure 4-19, the value for ϕ_3 is the former. The calculation for $\boldsymbol{r}_3$ is given by:

$$\boldsymbol{r}_3 = \begin{bmatrix} b\sin(\phi_3) \\ Y_0 + 2b\cos(\phi_3) \\ 0 \end{bmatrix} \tag{4.9}$$

The time for the microinspector to travel from $\boldsymbol{r}_2$ to $\boldsymbol{r}_3$ can be calculated by:

$$\Delta t_{2-3} = \frac{\phi_3 - \phi_2}{\omega} \tag{4.10}$$

Then, the time at which $\Delta\boldsymbol{v}_3$ is applied is $t_3 = t_2 + \Delta t_{2-3}$. To compute $\Delta\boldsymbol{v}_3$, the velocity at $\boldsymbol{r}_3$ on E_2, $\boldsymbol{v}_{3p}$, and the desired velocity on E_3, $\boldsymbol{v}_{2a}$, must be determined. The out-of-plane phase angle at $\boldsymbol{r}_3$ for E_3 is defined as $\psi_3 = \phi_3 + \theta$. $\boldsymbol{v}_{3p}$ and $\boldsymbol{v}_{2a}$ can be calculated by Eqn 4.11 and Eqn 4.12, respectively.

$$\boldsymbol{v}_{3p} = \begin{bmatrix} b\omega\cos(\omega\Delta t_{2-3} + \phi_2) \\ 2b\omega\sin(\omega\Delta t_{2-3} + \phi_2) \\ 0 \end{bmatrix} \tag{4.11}$$

$$\boldsymbol{v}_{3a} = \begin{bmatrix} b\omega\cos(\phi_3) \\ 2b\omega\sin(\phi_3) \\ c\omega\cos(\psi_3) \end{bmatrix} \tag{4.12}$$

The third and final impulse velocity is then given by:

$$\Delta\boldsymbol{v}_3 = \boldsymbol{v}_{3a} - \boldsymbol{v}_{3p} \tag{4.13}$$

2. If the avoidance constraints are violated for the transfer maneuver described in 1, an intermediary position on the V-bar may be employed, as in Section 4.2.1. From this position, the microinspector can be inserted into the desired 2×1 ellipse, where the path intersects with the in-plane. This transfer takes the path of an in-plane 2×1 ellipse that connects the position on the V-bar to the intersecting point. The intermediary position is chosen such that the microinspector stays outside the keep-out zone designated by the avoidance constraints. Figure 4-20 shows a case where the transfer trajectory is computed to stay outside of the avoidance constraints. All Δv burns can be calculated from Eqn 3.9.

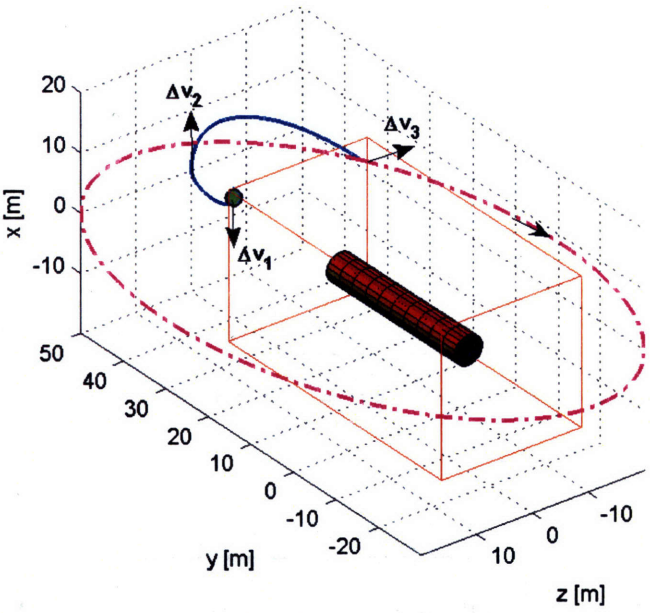

(a) 3D

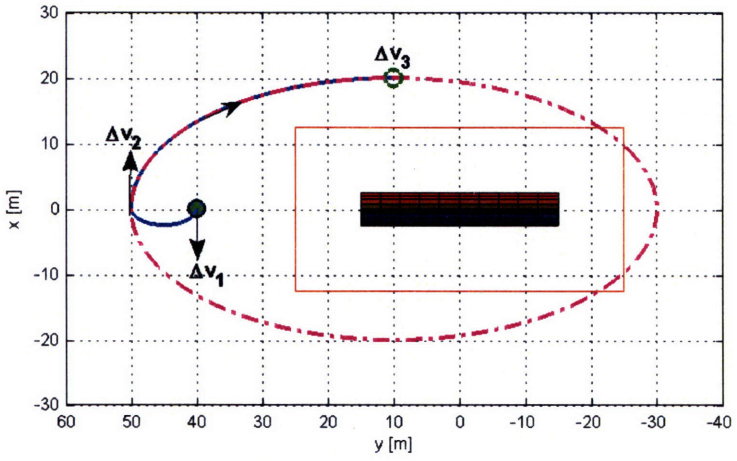

(b) Side View (in-plane)

Figure 4-20: V-bar $\Longleftrightarrow$ 2×1 Ellipse with Avoidance Constraints

The method for computing the transfer trajectories from a 2×1 ellipse to a desired position on the V-bar is just the reverse of the methods outlined in 1 and 2.

4.2.3 V-bar $\Longleftrightarrow$ $\boldsymbol{r}$, $\boldsymbol{v}$

Tables 4.4–4.5 describe the variables that are used to compute the transfer trajectory between a position on the V-bar and a position outside the avoidance constraints with some velocity. The relative velocity at the position on the V-bar is assumed to be zero.

Table 4.4: 2×1 Ellipse $\Longrightarrow$ $\boldsymbol{r}$, $\boldsymbol{v}$: Computational Variables

Variable	Description
$\boldsymbol{r}_i$	Initial position on 2×1 ellipse
t_i	Time at $\boldsymbol{r}_i$
$\boldsymbol{r}_f$	Desired position vector (on V-bar)
$\boldsymbol{v}_f$	Velocity vector at $\boldsymbol{r}_f$
ω	Orbital rate of host
$\boldsymbol{d}$	Differential acceleration vector
box	Dimensions of box constraint

Table 4.5: $\boldsymbol{r}$, $\boldsymbol{v}$ $\Longrightarrow$ V-bar: Computational Variables

Variable	Description
$\boldsymbol{r}_i$	Initial position on 2×1 ellipse
$\boldsymbol{v}_i$	Initial velocity on 2×1 ellipse
t_i	Time at $\boldsymbol{r}_i$
$\boldsymbol{r}_f$	Desired position vector (on V-bar)
ω	Orbital rate of host
$\boldsymbol{d}$	Differential acceleration vector
box	Dimensions of box constraint

1. Utilizing the natural 2×1 ellipse trajectory to transfer from a position on the V-bar to some position with a desired velocity simplifies the computations greatly. First, the microinspector is sent to an intermediary position on the V-bar, using the method described in Section 4.2.1. This intermediary position is computed

such that the microinspector travels for a fourth of the orbital period on the 2×1 ellipse connecting it and the final desired position, without violating the avoidance constraints. Therefore, if the desired z component of $\boldsymbol{r}_f$ is given by z_d, the traveling ellipse out-of-plane component, c, of this connecting 2×1 ellipse is exactly z_d. Once the final position is reached, a Δv is applied to achieve the desired velocity at that position. Figure 4-21 illustrates an example of this transfer trajectory method. This method works as long as the final position is not located in the y-z plane intersecting the origin. Also, close to this plane, the fuel expenditure for the transfer trajectory also becomes quite large.

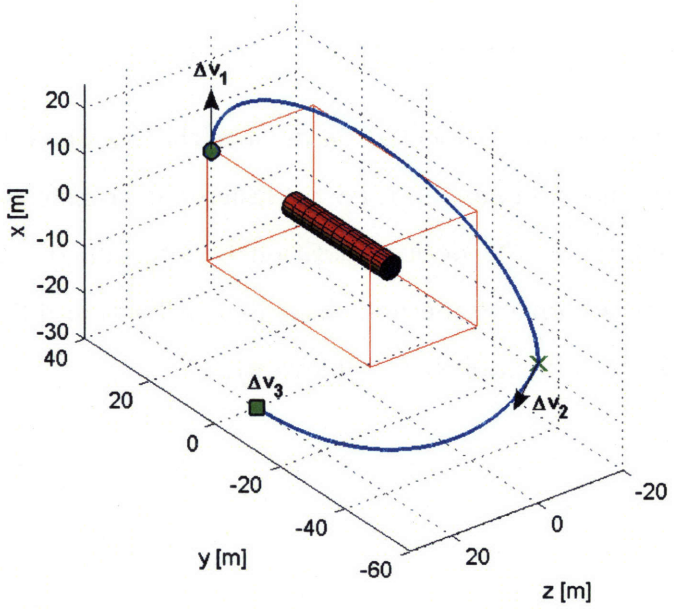

(a) 3D

Figure 4-21

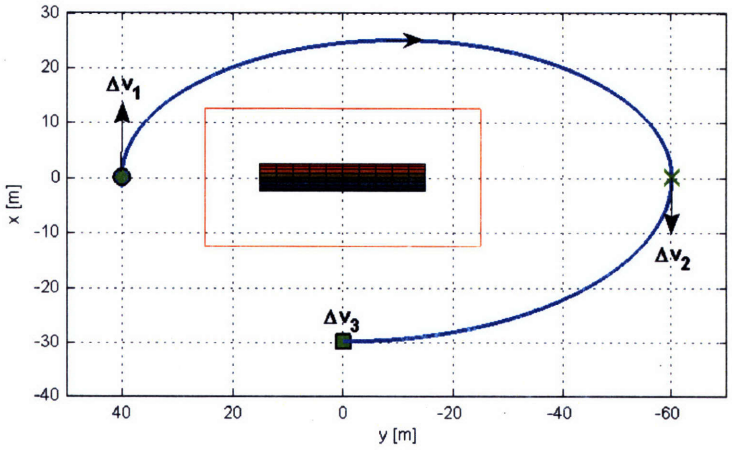

(b) Side View (in-plane)

Figure 4-21: V-bar $\Longleftrightarrow$ $\boldsymbol{r}$, $\boldsymbol{v}$

2. When the final position is located on or near the y-z plane that intersects the origin, another method can be used to design the transfer trajectory. A 2×1 ellipse that intersects the desired position is determined. Then, the transfer trajectory is based on the method described in Section 4.2.2. At the desired position, a Δv burn is applied to achieve $\boldsymbol{v}_f$.

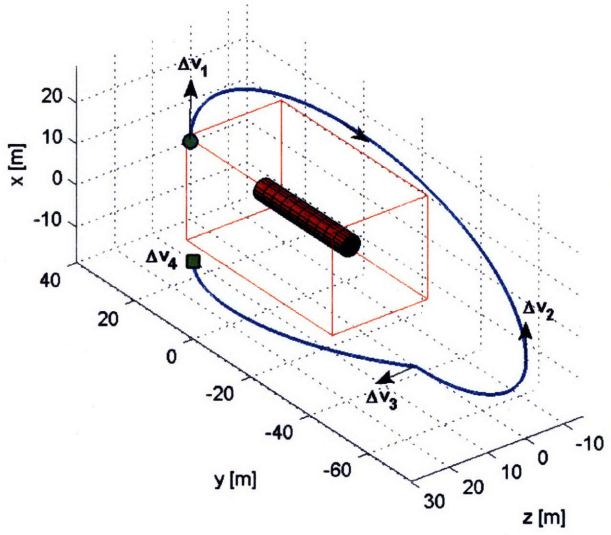

(a) 3D

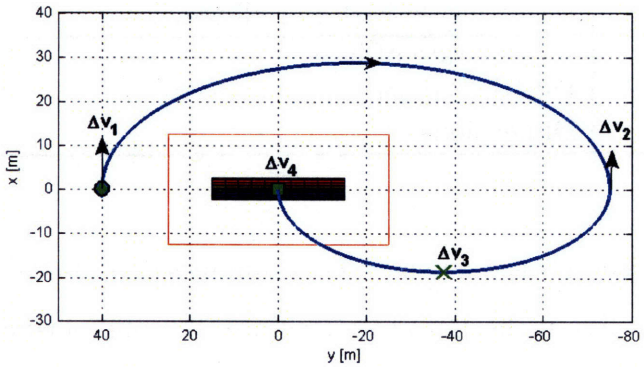

(b) Side View (in-plane)

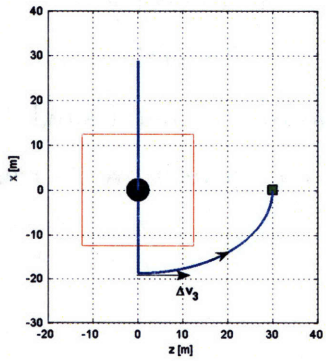

(c) Front View

Figure 4-22: V-bar $\Longleftrightarrow$ $\boldsymbol{r}$, $\boldsymbol{v}$ via Inclined 2×1 Ellipse

The trajectory design method for the reverse transfer is simply the reverse of 1 or 2.

4.2.4 2×1 Ellipse $\Longrightarrow$ 2×1 Ellipse

Table 4.6 outlines the variables needed for designing and computing the transfer trajectory from a 2×1 ellipse to another 2×1 ellipse.

Table 4.6: 2×1 Ellipse $\Longrightarrow$ 2×1 Ellipse: Computational Variables

Variable	Description
$\boldsymbol{r}_i$	Initial position on 2×1 ellipse
$\boldsymbol{v}_i$	Initial velocity on 2×1 ellipse
t_i	Time at $\boldsymbol{r}_i$
b	Semiminor axis of desired 2×1 ellipse
c	Out-of-plane component of desired 2×1 ellipse
Y_0	Center of desired 2×1 ellipse on y-axis
θ	$\psi - \phi$ for desired 2×1 ellipse, for $\phi = 0°$
ω	Orbital rate of host
$\boldsymbol{d}$	Differential acceleration vector
box	Dimensions of box constraint

This transfer trajectory uses much of the techniques described so far for computing transfer trajectories. From the initial 2×1 ellipse, the microinspector is transferred to a position on the V-bar that lies on an in-plane 2×1 ellipse corresponding to the desired final 2×1 ellipse. In essence, this means that the values for b and Y_0 are equal for the desired 2×1 ellipse and the corresponding in-plane 2×1 ellipse. Once the position on the V-bar is reached, the method described in Section 4.2.2 is utilized to travel from the V-bar location to the final desired 2×1 ellipse. Figure 4-23 shows an example of a transfer trajectory between two 2×1 ellipses.

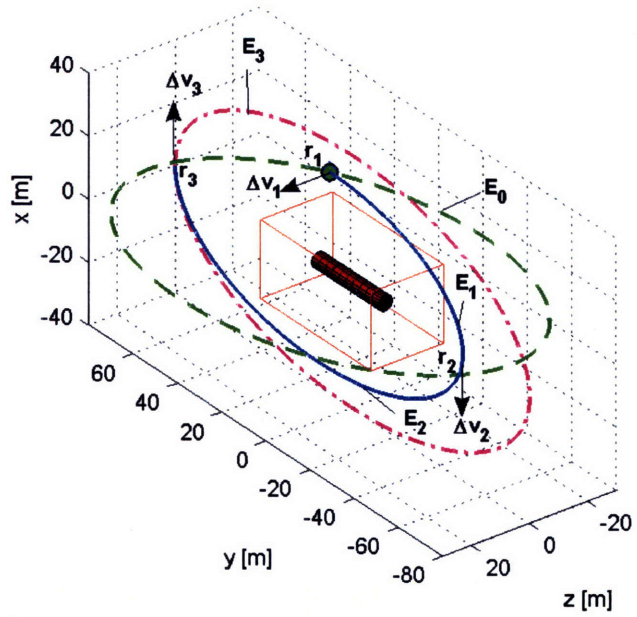

Figure 4-23: 2×1 Ellipse $\Longrightarrow$ 2×1 Ellipse

Initially, the microinspector is in an inclined 2×1 ellipse. Let this trajectory be denoted by E_0. The first impulse velocity, $\Delta \boldsymbol{v}_1$, is applied to transfer from E_0 to a corresponding in-plane trajectory, E_1. The traveling ellipse parameters for E_0 can be determined from $\boldsymbol{r}_i$ and $\boldsymbol{v}_i$. The semiminor axis and center location on the V-bar for E_1 are the same as in E_0. They are designated by the subscript 1 in this example. With the values for these parameters known, the location of the first impulse velocity burn, $\boldsymbol{r}_1$, can be calculated using the *CW* solution. $\boldsymbol{r}_1$ is the location where E_0 and E_1 intersect, which is designated by either $\phi_1 = 2\pi - \theta_0$ or $\phi_1 = \pi - \theta_0$, where θ_0 is the constant θ value for E_0. Recall from Section 3.1.2 that θ is constant for a specific 2×1 ellipse, while ϕ and ψ are not. For the example in Figure 4-23, the value for ϕ_1 is the latter. $\boldsymbol{r}_1$ can be calculated as:

$$\boldsymbol{r}_1 = \begin{bmatrix} b_1 \sin(\phi_1) \\ Y_{01} + 2b_1 \cos(\phi_1) \\ 0 \end{bmatrix} \tag{4.14}$$

$\phi_0 = \phi_1$, since E_1 is the corresponding in-plane 2×1 ellipse to E_0. The velocity at $\boldsymbol{r}_1$ before any burn is conducted is:

$$\boldsymbol{v}_{1p} = \begin{bmatrix} b_1\omega\cos(\phi_1) \\ 2b_1\omega\sin(\phi_1) \\ c_1\omega\cos(\psi_0) \end{bmatrix} \tag{4.15}$$

where, $\psi_0 = \theta_0 + \phi_0$. Thus, the first impulse velocity burn is:

$$\Delta\boldsymbol{v}_1 = \boldsymbol{v}_{1a} - \boldsymbol{v}_{1p} \tag{4.16}$$

The position of the second burn is where the microinspector reaches the V-bar on E_1, which occurs at $\phi_2 = 180°$ in Figure 4-23. If $\Delta\boldsymbol{v}_1$ is applied at t_1, then $\Delta\boldsymbol{v}_2$ is applied at $t_2 = t_1 + \Delta t_{1-2}$. The equation for Δt_{1-2} is given by:

$$\Delta t_{1-2} = \frac{\phi_2 - \phi_1}{\omega} \tag{4.17}$$

Hence, the location of $\Delta\boldsymbol{v}_2$ is:

$$\boldsymbol{r}_2 = \begin{bmatrix} b_1\sin(\omega\Delta t_{1-2} + \phi_1) \\ Y_{01} + 2b_1\cos(\omega\Delta t_{1-2} + \phi_1) \\ 0 \end{bmatrix} \tag{4.18}$$

The velocity at $\boldsymbol{r}_2$ prior to applying a burn is:

$$\boldsymbol{v}_{2p} = \begin{bmatrix} b_1\omega\cos(\omega\Delta t_{1-2} + \phi_1) \\ 2b_1\omega\sin(\omega\Delta t_{1-2} + \phi_1) \\ 0 \end{bmatrix} \tag{4.19}$$

From $\boldsymbol{r}_2$ on the V-bar, the microinspector is transferred to a V-bar position on the final 2×1 ellipse via an in-plane 2×1 ellipse. Let this in-plane 2×1 ellipse be called E_2 and let the desired 2×1 ellipse be denoted by E_3. Notably, this end position on E_2 is designated by ϕ_3. Since this position intersects with E_3, $\boldsymbol{r}_3$ can be computed using the traveling ellipse parameters describing E_3. In Figure 4-23, ϕ at $\boldsymbol{r}_3$ on E_2

and E_3 is equal to $\phi_3 = 0°$. $\boldsymbol{r}_3$ is given by:

$$\boldsymbol{r}_3 = \begin{bmatrix} b\sin(\phi_3) \\ Y_0 + 2b\cos(\phi_3) \\ 0 \end{bmatrix} \tag{4.20}$$

Now, given the values for $\boldsymbol{r}_2$ and $\boldsymbol{r}_3$, b_2 and Y_{02} for E_2 can be determined using Eqns 4.2–4.3. The velocity required at $\boldsymbol{r}_2$ to get the microinspector traveling on E_2 is then given by:

$$\boldsymbol{v}_{2a} = \begin{bmatrix} b_2\omega\cos(\phi_2) \\ 2b_2\omega\sin(\phi_2) \\ 0 \end{bmatrix} \tag{4.21}$$

The second impulse velocity is then:

$$\Delta\boldsymbol{v}_2 = \boldsymbol{v}_{2a} - \boldsymbol{v}_{2p} \tag{4.22}$$

Finally, the third impulse velocity is applied at $\boldsymbol{r}_3$ at time $t_3 = t_2 + \Delta t_{2-3}$. The equation for Δt_{2-3} is given by:

$$\Delta t_{2-3} = \frac{\phi_3 - \phi_2}{\omega} \tag{4.23}$$

The velocity prior to the final burn is:

$$\boldsymbol{v}_{3p} = \begin{bmatrix} b\omega\cos(\omega\Delta t_{2-3} + \phi_2) \\ 2b\omega\sin(\omega\Delta t_{2-3} + \phi_2) \\ 0 \end{bmatrix} \tag{4.24}$$

The velocity required for the microinspector to traverse E_3 is:

$$\boldsymbol{v}_{3a} = \begin{bmatrix} b\omega\cos(\phi_3) \\ 2b\omega\sin(\phi_3) \\ 0 \end{bmatrix} \tag{4.25}$$

The third and final impulse velocity is then given by:

$$\Delta \boldsymbol{v}_3 = \boldsymbol{v}_{3a} - \boldsymbol{v}_{3p} \tag{4.26}$$

If the final 2×1 ellipse is inclined, then a fourth impulse velocity is needed at the intersection of this desired 2×1 ellipse and its in-plane counterpart, much as in Section 4.2.2.

4.2.5 Inclined 2×1 Ellipse $\Longleftrightarrow$ Spiral

Table 4.7 describes the variables that are used to compute the transfer trajectory from a 2×1 ellipse to a spiral trajectory.

Table 4.7: Inclined 2×1 Ellipse $\Longleftrightarrow$ Spiral: Computational Variables

Variable	Description
$\boldsymbol{r}_i$	Initial position on 2×1 ellipse
$\boldsymbol{v}_i$	Initial velocity on 2×1 ellipse
t_i	Time at $\boldsymbol{r}_i$
b	Semiminor axis for desired spiral
c	Out-of-plane component for desired spiral
θ	$\psi - \phi$ for desired spiral
$y = [y_1, y_2]$	y_1: Starting point for center of ellipse, y_2: Ending point for center of ellipse
l	Desired distance between spiral loops
ω	Orbital rate of host
$\boldsymbol{d}$	Differential acceleration vector
box	Dimensions of box constraint

The spiral, as described in Section 4.1.7, is an inclined 2×1 ellipse whose center is deviated along to the R-bar (x-axis). This deviation causes a drift in the original stationary 2×1 ellipse, resulting in a spiral-like trajectory. First the transfer trajectory is computed to traverse from the initial 2×1 ellipse to a stationary 2×1 ellipse with the same traveling ellipse parameter values as for the spiral, except for X_0. Since the 2×1 ellipse is stationary, X_0 must be set to zero. The method discussed in Section 4.2.4 may be utilized to transfer the microsatellite inspector to this 2×1 ellipse.

To begin the spiral motion from the ellipse, a Δv burn may be applied at any point on the elliptical trajectory, parallel to the V-bar. Refer to Appendix B for an explanation on the direction of Δv. A Δv burn in the positive y-direction causes the microinspector to spiral in the negative y-direction. Conversely, with a Δv burn in the negative y-direction, the microinspector will spiral in the positive y-direction. To simplify the calculations, the simulations for this study applies the Δv at either $\phi = 90°$ or $\phi = 270°$. The magnitude of Δv depends on the preferred distance, l, between the spiraling loops.

Figure 4-24 illustrates the Δv burn at $\phi_b = 90°$ on a stationary inclined 2×1 ellipse to start the spiral motion.

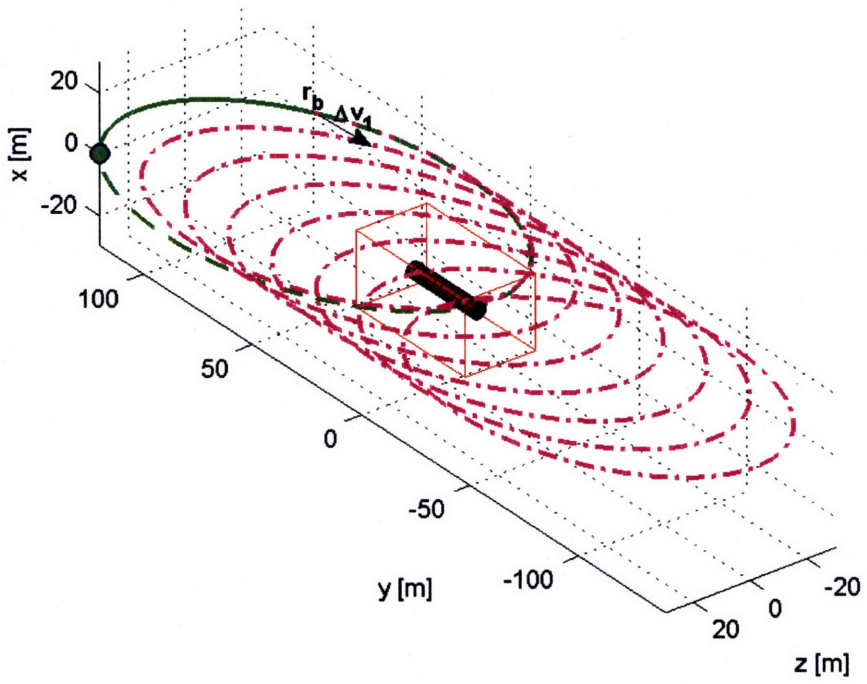

Figure 4-24: 2×1 Ellipse $\Longrightarrow$ Spiral

Y_0 of the stationary ellipse, as well as for the spiral, is set to the specified value for y_1. The direction of the spiral is simply:

$$direction = \text{sign}\,(y_2 - y_1) \tag{4.27}$$

With $\psi_b = \phi_b + \theta$, the location of the burn is given by:

$$\boldsymbol{r}_b = \begin{bmatrix} b\sin(\phi_b) \\ Y_0 + 2b\cos(\phi_b) \\ c\omega\cos(\psi_b) \end{bmatrix} \tag{4.28}$$

Let t_b be the time at which the microinspector reaches $\boldsymbol{r}_b$. The velocity prior to the burn is then:

$$\boldsymbol{v}_{bp} = \begin{bmatrix} b\omega\cos(\omega t_b + \phi_b) \\ 2b\omega\sin(\omega t_b + \phi_b) \\ c\omega\cos(\omega_b + \psi_b) \end{bmatrix} \tag{4.29}$$

The value of X_0 for the desired spiraling motion can be computed analytically from the *CW* solution, with the value for *direction* and the desired value of l. The distance between the traveling ellipses, or the spiral loops, can be determined by computing the difference between the position of a point on the spiral and the position on the spiral one orbital period, P, later. It can be inferred from the *CW* solution that the difference is purely along the V-bar, or y-axis. Since any point on the spiral may be used, the positions at $t = 0$ and $t = P$ can be substituted into the y equation in Eqn 3.8 to find the distance between the spiral loops. Using the known relationship between P and the orbital rate, ω, further simplifies the results.

At $t = 0$,

$$y(0) = Y_0 + 2b\cos(\phi) \tag{4.30}$$

At $t = P$, with $P = \frac{2\pi}{\omega}$,

$$
\begin{aligned}
y(P) &= Y_0 - \frac{3}{2}\omega P X_0 + 2b\cos(\omega P + \phi) \\
&= Y_0 - \frac{3}{2}\omega\left(\frac{2\pi}{\omega}\right)X_0 + 2b\cos\left(\omega\left(\frac{2\pi}{\omega}\right) + \phi\right) \\
&= Y_0 - 3\pi X_0 + 2b\cos(2\pi + \phi) \\
&= Y_0 - 3\pi X_0 + 2b\cos(\phi)
\end{aligned} \tag{4.31}
$$

Then,

$$
\begin{aligned}
\Delta y_P &= y(P) - y(0) \\
&= -3\pi X_0
\end{aligned} \tag{4.32}
$$

Since the desired values for Δy_P is l, substituting l into Eqn 4.32 gives the correct value for X_0:

$$
X_0 = -direction\frac{l}{3\pi} \tag{4.33}
$$

The velocity required for the spiral motion is then:

$$
\boldsymbol{v}_{ba} = \begin{bmatrix} b\omega\cos(\omega t_b + \phi_b) \\ -\frac{3}{2}\omega X_0 + 2b\omega\sin(\omega t_b + \phi_b) \\ c\omega\cos(\omega t_b + \psi_b) \end{bmatrix} \tag{4.34}
$$

Finally, the impulse velocity to transfer into the desired spiral trajectory is computed as:

$$
\Delta\boldsymbol{v}_b = \boldsymbol{v}_{ba} - \boldsymbol{v}_{bp} \tag{4.35}
$$

Comparison between Eqn 4.29 and Eqn 4.34 confirms that the impulse velocity to achieve a spiral trajectory is applied purely along the V-bar. The magnitude — $\frac{3}{2}\omega X_0$ — depends on the specified distance between the spiral loops, l, due to the X_0 factor.

4.3 Estimation of Δv Burns

The position, magnitude, and direction of the Δv burns are not explicitly computed for orbit maintenance and attitude control in the simulation created for this study. Nevertheless, to attain more realistic fuel costs for a microinspector mission, the simulation does include estimations of the fuel used during orbit maintenance due to differential drag, and to spin-up the microsatellite about a body-fixed axis. This section discusses how the Δv estimation is done for both cases.

4.3.1 Orbit Maintenance due to Differential Drag

Section 3.3 introduced the problem of differential drag and the resulting impact on the motion of a microsatellite inspector via the *CW* equations. In particular, the calculation for constant differential drag, based on altitude, the physical specifications of the host and microinspector vehicles, and the respective orientations, were discussed in Section 3.3.2. This constant differential acceleration due to drag may be used to estimate the amount of fuel required per orbital period, by the microinspector. If a_d is the magnitude of the differential drag and P is the orbital period, then the total Δv needed per orbit to overcome the degradation caused by differential drag is given by:

$$\Delta v = a_d P \tag{4.36}$$

The Δv for each burn can be determined by dividing the total Δv by the number of burns per orbit. The direction of each individual burn must be opposite to the direction of the differential drag vector, $\boldsymbol{a_d}$.

The mission simulation in Chapter 5 includes estimates of fuel use for maintenance due to differential drag, based on Eqn 4.36. Using the results from Section 3.3.2, a few of the Δv estimates at different altitudes are given here, when both the microinspector and the host are edge on. At $500\,km$, the magnitude of the differential acceleration due to drag is computed to be $a_d = 9.9\times10^{-8}$. By Eqn 4.36, the Δv required for orbit maintenance is $5.63\times10^{-4}\,m/s$ per orbit. At lower altitudes, the Δv required

will be much larger, but may still be feasible depending on the fuel capacity. For the host and microinspector specifications in this thesis, at an altitude of $200\,km$, $a_d = 4.16\times10^{-5}$. Hence, the Δv required per orbit is $0.22\,m/s$, which is much less than the budgeted total Δv of $15\,m/s$.

4.3.2 Attitude Control System

The equations of motion used in the trajectory and mission simulation for this study are in 3DOF, since the *CW* solution is being utilized. Therefore, the position, velocity, and accelerations are explicitly computed for the microsatellite inspector's orbital (translational) motion. Although the attitude maneuvers are not simulated with any equations of motion, the orientation of the microinspector is included in the simulation as a specified variable. Because the angular rates of the vehicle are not directly computed, the fuel costs associated with attitude control must be estimated. For the simulation in Chapter 5, the attitude control of the microinspector is largely based on the constant angular rate method introduced in Section 3.5. Therefore, an estimate of the Δv required to spin-up the microsatellite about a body-fixed axis is needed.

Let the initial angular velocity of the microinspector about its body-fixed axes be $\boldsymbol{\omega}_0$. Let the desired angular velocity be $\boldsymbol{\omega}_f$. Then, the total time that the gas thrusters are activated to achieve $\Delta\omega = |\boldsymbol{\omega}_f - \boldsymbol{\omega}_0|$, is:

$$\Delta t = \frac{I\Delta\omega}{N_T F r} \tag{4.37}$$

where, I is the moment of inertia about the specified body-fixed axis, N_T is the number of thrusters being used, F is the maximum thrust capacity of the gas thrusters, and r is the distance between the microinspector's center of mass and the thruster.

The average mass flow rate, $\dot{m}_{av}$, for each thruster can be estimated as:

$$\dot{m}_{av} = \frac{F}{I_{sp}g} \tag{4.38}$$

where, I_{sp} is the specific impulse of the propulsion system and g is the acceleration

due to gravity. Then, the mass of the propellant used to reach the desired constant angular rate is:

$$\Delta m = (\dot{m}_{av} \Delta t)\, N_T \tag{4.39}$$

Finally, the Δv required for the spin-up can be calculated by the rocket equation:

$$\Delta v = I_{sp} g \ln \frac{m_0}{m_0 - \Delta m} \tag{4.40}$$

where m_0 is the initial mass of the microinspector and the fuel.

Let $F = 10\,mN$, $I_{sp} = 50\,s$, $I = 0.012\,kg/m^2$, $r = 0.1\,m$, $m_0 = 3.3\,kg$ ($3\,kg$ microinspector and $0.3\,kg$ propellant), and $g = 9.8\,m/s^2$. If the desired spin rate is the same as the orbital rate of the host vehicle at $500\,km$, which is $\omega = 0.0022\,rad/s$, then the required Δv from $\boldsymbol{\omega}_0 = 0\,rad/s$ by Eqns 4.37–4.40 is $8 \times 10^{-5}\,m/s$.

The fuel estimation method presented so far may also be used to estimate the total Δv used during a Sun-nadir pointing scheme. Define a coordinate frame that is fixed to the body of the microinspector. Assume the camera's boresight vector and the normal vector to the solar cells at time t_1 and t_2 are known. Then, the body-fixed unit vector of rotation, $\hat{\boldsymbol{e}}$, and the angle of rotation, θ_e, which describe the attitude motion from t_1 to t_2 can be determined. $\hat{\boldsymbol{e}}$ is also known as the eigenvector of rotation — a parameter of the quaternion representation for the rotation. The body-fixed angular velocity of the microinspector is then given by:

$$\boldsymbol{\omega}_f = \left(\frac{\theta_e}{t_2 - t_1} \right) \hat{\boldsymbol{e}} \tag{4.41}$$

If $\boldsymbol{\omega}_1$ is the angular rate of the microinspector at t_1, then the total change in angular rate is given by $\Delta\omega = |\boldsymbol{\omega}_f - \boldsymbol{\omega}_1|$. Eqns 4.37–4.40 can then be used to calculate the Δv to achieve the body-fixed rotation. Thus, there is a direct correlation between $\Delta\omega$ and Δv. By employing this method at each time-step of the simulation, the fuel expenditure can be estimated, since these calculations represent a bang-bang type controller. It is assumed that the time-step is greater than the Δt computed in Eqn 4.37. The simulation in Chapter 5 also adds margin to this estimate.

Computing $\hat{e}$ and θ_e Using Two Vectors

Let $\hat{\boldsymbol{u}}_1$ and $\hat{\boldsymbol{u}}_2$ be the unit boresight vectors in the inertial frame at t_1 and t_2, respectively. When no constraint on the normal vector to the solar cells exists, there are an infinite number of combinations of $\hat{\boldsymbol{e}}$ and θ_e that will take the boresight vector from $\hat{\boldsymbol{u}}_1$ to $\hat{\boldsymbol{u}}_2$. One simple method to determine a vector $\hat{\boldsymbol{e}}$ is to find a vector that is normal to $\hat{\boldsymbol{u}}_1$ and $\hat{\boldsymbol{u}}_2$. Then, θ_e is the minimum angle between $\hat{\boldsymbol{u}}_1$ and $\hat{\boldsymbol{u}}_2$. This method can be utilized at each time step to determine the overall Δv for attitude control. The equations are given by:

$$\hat{\boldsymbol{e}} = \text{Unit } \{\hat{\boldsymbol{u}}_1 \times \hat{\boldsymbol{u}}_2\} \tag{4.42}$$

$$\theta_e = \cos^{-1}(\hat{\boldsymbol{u}}_1 \cdot \hat{\boldsymbol{u}}_2) \tag{4.43}$$

Eqns 4.42–4.43 give an $\hat{\boldsymbol{e}}$ and θ_e pair that minimizes the path from $\hat{\boldsymbol{u}}_1$ to $\hat{\boldsymbol{u}}_2$. $\hat{\boldsymbol{e}}$ can be transformed to the inspector body-fixed reference frame to determine Δv. The overall Δv for attitude maneuvers with this method is rarely minimum, since only two points on the path is considered per time-step. The simulations in this thesis will employ Eqns 4.42–4.43 to obtain a conservative estimate of the rotational Δv.

Computing $\hat{e}$ and θ_e Using Three Vectors

Section 3.5.4 described the path of the boresight vector orientation in inertial space, when it stays normal to the V-bar during an inclined 2×1 ellipse that is circular in the x-z plane. This path is illustrated in Figure 4-25. The unit boresight vector traces a "figure eight" on the surface of a unit sphere. When the boresight vector is on the top or bottom loop of this "figure eight," it is generally rotating about the axes of rotation shown in the figure. During the "figure eight" path, the axis of rotation is not constant, since the path is not circular. However, the variation is incremental and gradual, which alludes to a small value of total $\Delta\omega$ during these loop phases of the "figure eight". The larger values of $\Delta\omega$ occur when the boresight vector travels through the center of this "figure eight".

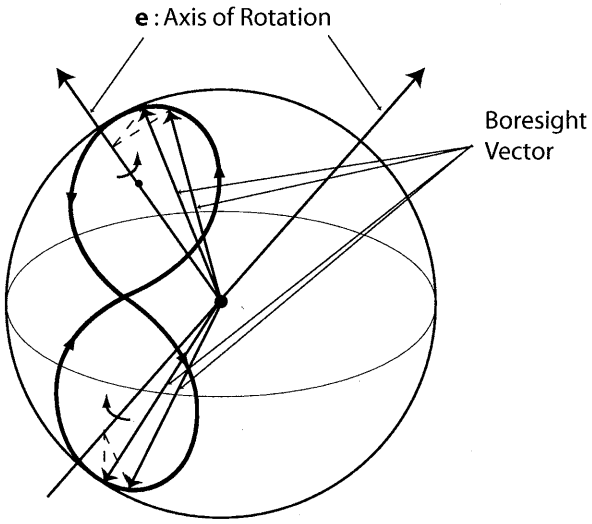

Figure 4-25: Axis of Rotation for Boresight Vector

To compute the axis of rotation at an instant in time (each time-step of a simulation), as in Figure 4-25, three consecutive unit boresight vectors are needed: $\hat{\boldsymbol{u}}_1$, $\hat{\boldsymbol{u}}_2$, and $\hat{\boldsymbol{u}}_2$ at times t_1, t_2, and t_3, respectively. These vectors and the associated angles are illustrated in Figure 4-26.

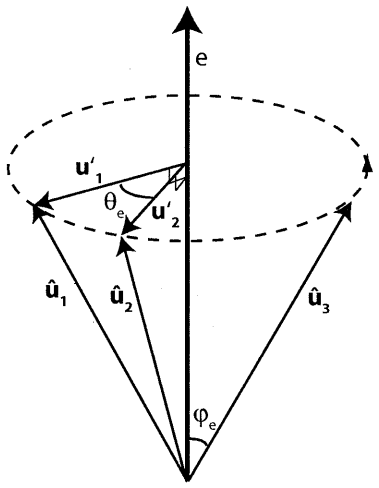

Figure 4-26: Three Vectors to Determine Axis of Rotation

ϕ_e, the angle between the three vectors and the desired $\hat{\boldsymbol{e}}$, is a constant. $\hat{\boldsymbol{e}}$ can be calculated by:

$$\hat{\boldsymbol{e}} = \text{Unit } \{\hat{\boldsymbol{u}}_1 \times \hat{\boldsymbol{u}}_2 + \hat{\boldsymbol{u}}_2 \times \hat{\boldsymbol{u}}_3 + \hat{\boldsymbol{u}}_3 \times \hat{\boldsymbol{u}}_1\} \tag{4.44}$$

Now, ϕ_e can be calculated using the dot product:

$$\phi_e = \cos^{-1}(\hat{\boldsymbol{u}}_1 \cdot \hat{\boldsymbol{e}}) \tag{4.45}$$

With the value for ϕ_e known, $\hat{\boldsymbol{u}}'_1$ and $\hat{\boldsymbol{u}}'_2$ can then be determined as:

$$\boldsymbol{u}'_1 = \hat{\boldsymbol{u}}_1 \sin(\phi_e) \tag{4.46}$$

$$\boldsymbol{u}'_2 = \hat{\boldsymbol{u}}_2 \sin(\phi_e) \tag{4.47}$$

Finally, the angle of rotation θ_e is calculated as the angle between $\boldsymbol{u}'_1$ and $\boldsymbol{u}'_2$:

$$\theta_e = \cos^{-1}\left(\frac{\boldsymbol{u}'_1 \cdot \boldsymbol{u}'_2}{|\boldsymbol{u}'_1|\,|\boldsymbol{u}'_2|}\right) \tag{4.48}$$

The following equation can also be used to determine θ_e:

$$\theta_e = \tan^{-1}\left[\frac{(\hat{\boldsymbol{u}}_1 \times \hat{\boldsymbol{u}}_2) \cdot \hat{\boldsymbol{e}}}{\hat{\boldsymbol{u}}_1 \cdot \hat{\boldsymbol{u}}_2}\right] \tag{4.49}$$

Eqn 4.49 is computationally less intensive than using Eqns 4.45–4.48, when calculating θ_e.

As in the two vector method, $\hat{\boldsymbol{e}}$ can be transformed to the inspector body-fixed reference frame to determine Δv. The computed $\hat{\boldsymbol{e}}$'s vary less for the three vector method than the two vector method. Thus, the total $\Delta\omega$ will be less, which suggests that this new approach will be somewhat more fuel efficient.

4.4 Station-keeping

Station-keeping of the microinspector may be necessary when images of a specific part of the host's surface are required. For LEO missions, the fuel usage for station-

keeping is primarily associated with resisting the effects of differential gravitational acceleration between the host vehicle and the microinspector. The $\Delta \boldsymbol{v}$ burns for station-keeping are not explicitly calculated from the equations of motion, nor are they directly applied to the simulations in this thesis. In order to explicitly calculate the positions and velocity burns for station-keeping, a regulatory control mechanism must be applied, which is beyond the scope of this thesis. Instead, an estimate of the Δv required for the duration of station-keeping is included in the fuel costs for the total mission. The differential gravity can be calculated from the acceleration vector in Eqn 3.4 or from Eqn 3.10, given the desired position for station-keeping in the LVRCS and setting $\boldsymbol{d}$ to zero. The initial velocity components are set to zero. Let $\boldsymbol{a}_g$ be the differential gravity. Then, the Δv required can be estimated by multiplying the continuous acceleration needed to overcome the effects of $\boldsymbol{a}_g$ and the total time at the desired position. The continuous acceleration is simply the opposite of $\boldsymbol{a}_g$. Thus, if Δt is the time at the desired position, the magnitude of Δv is given by:

$$\Delta v = |\Delta \boldsymbol{v}| = \Delta t \, |\boldsymbol{a}_g| \tag{4.50}$$

To simulate station-keeping using the CW equations, a differential acceleration that is equal in magnitude and opposite in direction to the differential gravity is applied as a part of $\boldsymbol{d}$ of Eqn 3.4.

4.5 Baseline Mission

This section presents a baseline microinspector mission concept for a host vehicle in orbit about Earth.

1. Mode 1: Deployment of Inspector from Host Spacecraft

   In mode 1, the microsatellite inspector is deployed from the host vehicle to a stationary position on the V-bar, a specified distance away. During this mode, the microinspector prepares for the inspection process. This may include calibration and testing of the on board sensors.

2. Mode 2: Global Inspection

   In mode 2, the microinspector carries out a global inspection of the host vehicle's surface. Starting from its initial position on the V-bar, the microinspector is dispatched to maneuver autonomously about the host vehicle for the inspection process. The trajectories that make up the global inspection mode are pre-computed to observe all necessary constraints and requirements. The global inspection process entails maneuvering the microinspector and controlling its attitude, such that complete coverage of the host vehicle's surface is achieved through the images taken by the on board camera. Once the global inspection is complete, the microinspector returns to a specified position on the V-bar for further commands.

3. Mode 3: Point Inspection

   In mode 3, the microsatellite inspector maneuvers to a specified position near the host vehicle and is properly oriented for point inspection. The specified position is chosen by ground operators after reviewing the images taken during the global inspection mode. Close-up images of a particular point or points on the host's surface may be desired after the images from the global inspection are assessed. If so, the positions and attitudes of the microinspector to acquire these images are uploaded to the microinspector that is awaiting instructions while on the V-bar. Once the specified position is reached, station-keeping maneuvers are executed until all images are taken. Following the point inspection process, the microinspector returns to the V-bar for further commands.

4. Mode 4: Disposal of Inspector

   In mode 4, the inspection function of the microinspector has been fulfilled, and safe disposal of the vehicle is initiated. The microinspector must not collide with the host vehicle, and in the case of an Earth orbiting mission, should eventually burn up in the Earth's atmosphere. The "disposal" methods include a safe re-docking with the host.

(This Page Intentionally Left Blank)

Chapter 5

Mission Design Simulation Results

In this section, an overview of the mission simulation for the Earth orbiting scenario is given and simulations of the baseline mission at two different altitudes are presented. Based on the figures of merit, the results of the simulation will be discussed and analyzed to check if the requirements from Section 2.2 are met. In this thesis, the figures of merit will be weighted equally. Also, general requirements for the microinspector hardware are recommended based on the results.

5.1 Simulation Overview

The 3DOF baseline mission simulation for a microsatellite inspector is based on the solution to the *CW* equations. The *CW* solution was detailed in Section 3.1. The four microinspector mission modes, which make up the baseline mission, were described in Section 4.5. These modes are summarized below:

1. Mode 1: Deployment of Inspector from Host Spacecraft
2. Mode 2: Global Inspection
3. Mode 3: Point Inspection
4. Mode 4: Disposal of Inspector

The microinspector and host hardware specifications are simulated based on the requirements presented in Section 2.2. The altitude and inclination of the host's orbit about Earth are specified. In the simulation, a set of trajectory and trajectory transfer combinations are employed to accomplish the task laid out by each mode. The trajectories are chosen from the toolset in Section 4.1, subject to the mission design strategies presented in Section 3. The transfers between the trajectories are carried out by the methods described in Section 4.2. For the inspection modes — Mode 2 and Mode 3 — the camera's boresight vector is oriented to point at the host, as described in Section 3.5. The baseline mission simulation presented here does not include any additional maneuvers to recharge the battery upon energy depletion, nor does it employ a sun angle minimizing scheme. The Δv used for orbit maintenance due to differential drag is estimated using Eqn 4.36. The rotational Δv for attitude control is estimated using Eqns 4.37–4.43 in Section 4.3. Finally, point inspection is simulated utilizing the station-keeping method from Section 4.4. In all simulations presented in this thesis, the host spacecraft is placed in the LVRCS so that the length lies along the V-bar. Thus, it is rotating in the inertial reference frame at the orbital rate to maintain a constant LVLH attitude. The simulations of the baseline inspection mission in this section are conducted at LEO.

5.2 Baseline Mission Simulation: 500 km

The hardware specifications for this simulation are based on the microinspector and host spacecraft descriptions from Section 2.2. The following list outlines the design specifications for the baseline mission results presented in this section.

- The host spacecraft is in a circular orbit around Earth at an altitude of 500 km at a 0° inclination.

- Since the minimum allowable distance from the surface during imaging is 10 m, in this simulation, the microinspector stays greater than 10 m from the host's surface, with an additional buffer of 0.1 m, for extra margin. Thus, the minimum

distance to the host's surface is $10.1\,m$ here.

- The geocentric inertial Sun position vector is along the positive X-axis of the geocentric inertial reference frame.
- The spirals are $4\,m$ apart, so that the images have greater than 10 pixels of overlap, laterally.
- The total time for the inspection mission is about $35P$, where $1P = 1.577\,hr$. The time-step for the simulation is $\approx 57\,s$. This does not include the disposal mode.

Mode 1: Deployment of Inspector

Section 4.1.3 described how a segment of the intersecting 2×1 ellipse could be employed to deploy the microinspector to a safe position on the V-bar. This method is utilized in this simulation. The microinspector maneuvers to a position behind the host on the V-bar. When it attains the desired position on the V-bar, an appropriate Δv is applied by the thrusters to stop the motion in the LVRCS. The Δv is determined using the transfer method in Section 4.2.1, while disregarding the keep-out-zone for this mode. Figure 5-1 illustrates the deployment of the microsatellite inspector from the host spacecraft. Sitting on the V-bar allows for some system check-out time.

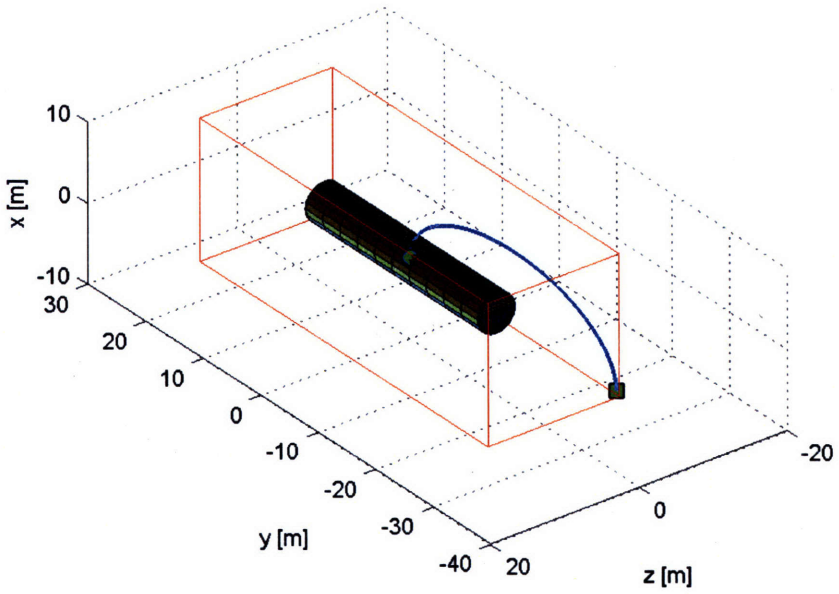

(a) 3D View

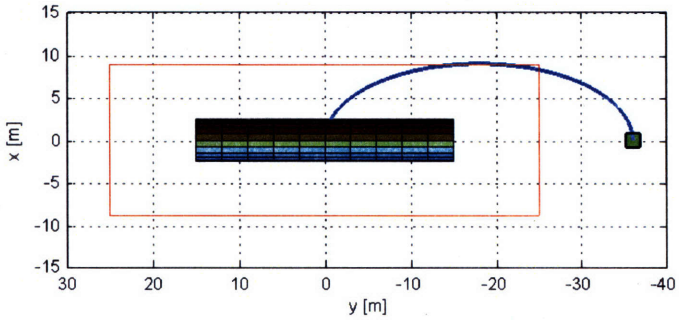

(b) Side View (in-plane)

Figure 5-1: Baseline Mission (500 km Earth Orbit): Mode 1 - Deployment

Mode 2: Global Inspection

A simple and effective method of maneuvering down the length of the V-bar was presented in Section 4.1.7. With the spiral trajectory, the attitude of the microinspector can be controlled such that the boresight vector of the camera on board points normal to the surface of the host, as discussed in Section 3.5.4. Therefore, the global inspection mode in this baseline simulation consists of the transfer trajectory from the microinspector's initial position on the V-bar to the spiraling motion and the transfer trajectory at the end of the spiral to a stationary position on the V-bar. The beginning and end position of the spiral motion is chosen so that the entire length of the host spacecraft is covered. The transfer trajectories are computed by combining the methods presented in Section 4.2.2 and Section 4.2.5. The trajectories for Mode 2 are displayed in Figure 5-2.

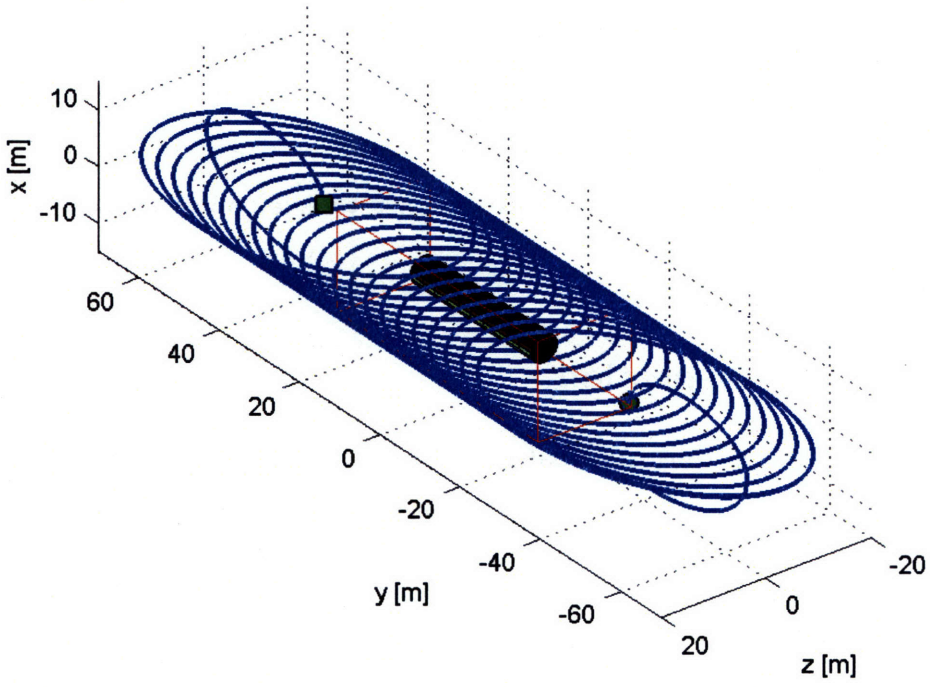

(a) 3D View

Figure 5-2

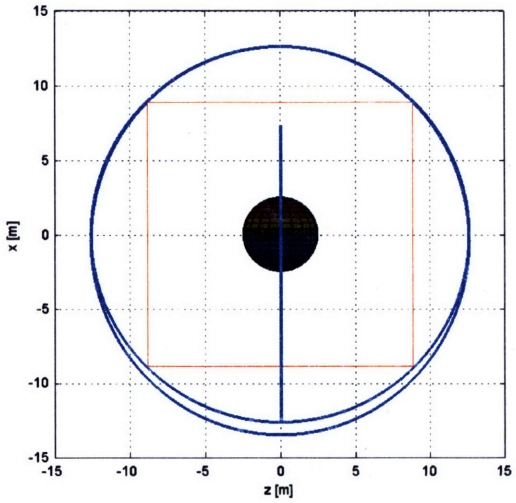

(b) Front View

Figure 5-2: Baseline Mission (500 km Earth Orbit): Mode 2 - Global Inspection

The minimum distance from the microinspector to the host's surface is 10.1 m throughout the spiral trajectory. Although the trajectory in Figure 5-2 allows the total surface of the host to appear in the compilation of the images, there are still periods in which images may not be taken due to a lack of sunlight. In these cases, a flash illuminator must be used unless the host vehicle cooperates and changes its orientation.

Mode 3: Point Inspection

After the images taken during global inspection are reviewed by ground operators, specific areas may then be designated for closer inspection. Based on the host surface location uploaded to the microinspector, the vehicle can compute a trajectory from its initial waiting position on the V-bar to a position and attitude that will give the best possible image resolution, while keeping outside the constraint zone. The transfer trajectory methods from Section 4.2.3 are employed here to simulate the point inspection mode maneuvers. Figure 5-3 depicts these trajectories.

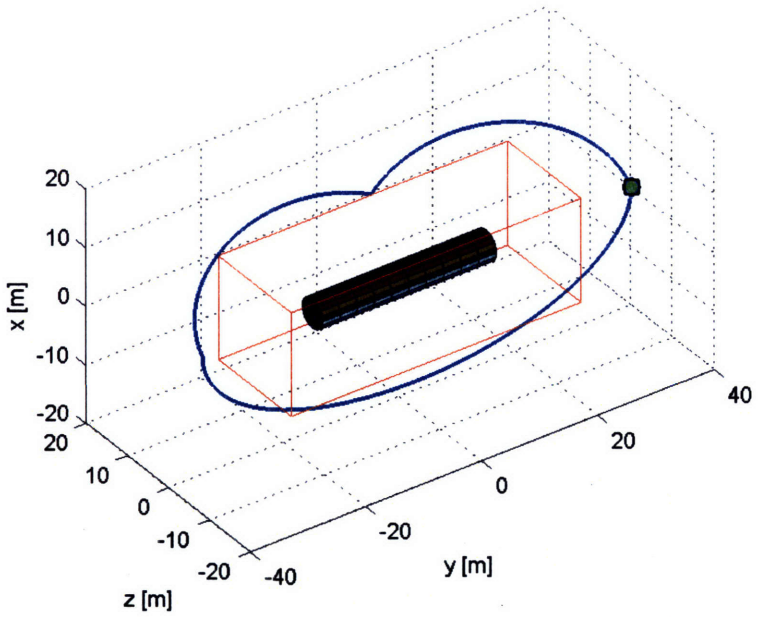

(a) 3D

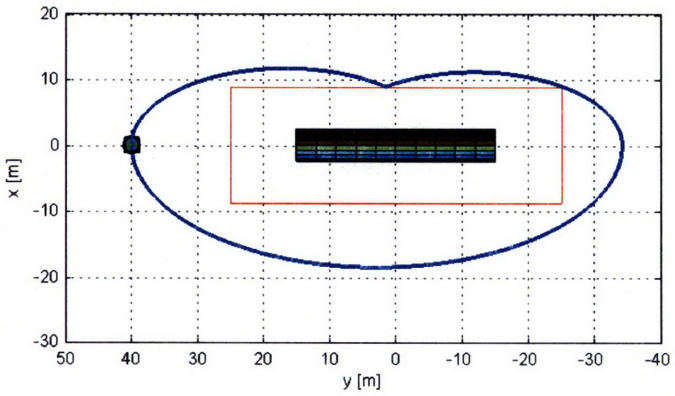

(b) Side View (in-plane)

Figure 5-3: Baseline Mission (500 km Earth Orbit): Mode 3 - Point Inspection

Mode 4: Disposal of Inspector

In the previous modes, the microinspector corrected for the undesirable motion caused by atmospheric drag. At the end of the inspection mission, this motion can be utilized to dispose of the microinspector. From a stationary positive position on the V-bar, a small Δv can be imparted by the microinspector, causing it to move away from the host spacecraft. Appendix B shows the effects of imparting a Δv parallel to the V-bar. Based on those results, in this simulation, a Δv is applied in the negative y-direction to achieve the motion shown in Figure 5-4. The microinspector can be oriented with respect to the host vehicle, such that the differential drag is negative, which causes the altitude of the microinspector to decrease. In Figure 5-4, notice the steady decrease of the deviation along the radial axis (x-axis). In time, the microinspector will naturally burn up in the Earth's atmosphere.

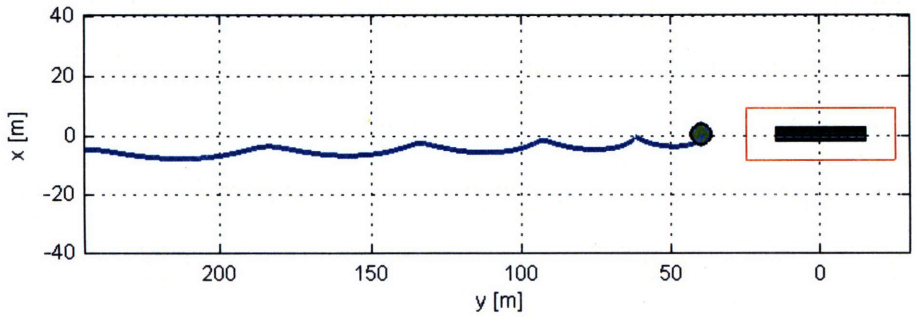

Figure 5-4: Baseline Mission (500 km Earth Orbit): Mode 4 - Disposal of Microinspector

Figures of Merit

The figures of merit from Section 3.7 are used in this section to discuss the quality of the inspection trajectories chosen for the baseline mission simulation at $500\,km$ from the Earth's surface.

The fuel expended during the entire mission for translational motion is much less than the total available Δv of $15\,m/s$, as shown in Figure 5-5a. The translational maneuvers take only about $0.2\,m/s$ in fuel. Table 3.3 shows that the differential drag is a small factor at $500\,km$. Thus, the Δv used for orbit maintenance throughout the mission is also small, which can be seen in Figure 5-5a from the 2^{nd} period to the 24^{rth} period. The estimated rotational Δv is also below the total available fuel, but is much larger than the Δv used for the translation motion. Recall from Section 4.3.2, that the method used to estimate the rotational fuel for this simulation was not the most fuel minimal method. Therefore, the Δv plot in Figure 5-5b is a conservative estimation. Figure 5-5c illustrates the total Δv used, which is a little over half the available $15\,m/s$ of fuel.

Based on the fuel expenditure simulation results, the majority of the propellant is used for the attitude control of the microinspector. In order to lower the fuel costs, the focus must be directed to developing a fuel-optimal attitude control algorithm. Further analysis must be conducted to more accurately estimate the fuel usage for specific attitude control schemes and to understand the coupling dynamics between the orbital and attitude motion.

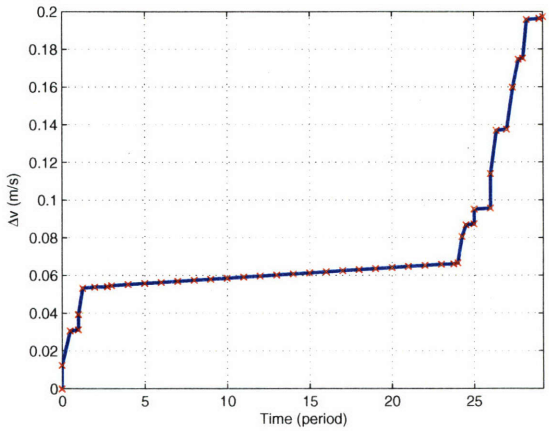

(a) Translation Δv

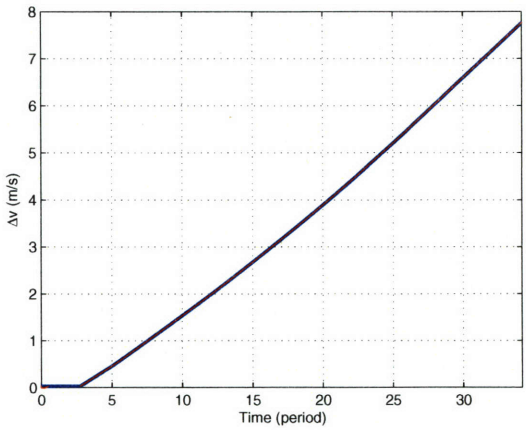

(b) Rotational Δv

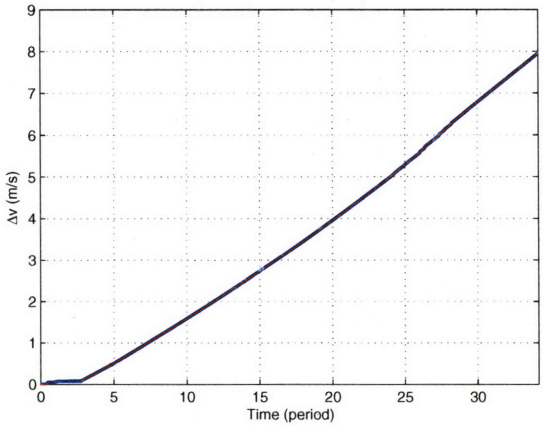

(c) Total Δv

Figure 5-5: Fuel Expenditure: Time vs. Δv

Although the rotational Δv is estimated here, the primary scope for fuel expenditure in this baseline simulation is the translational Δv. At a $500\,km$ altitude, the inspection trajectories in this baseline simulation are found to be excellent on the basis of fuel use.

The numbered labels of the points or segments on the host surface used in the simulation were graphically shown in Figure 3-21. Figure 5-6 illustrates the frequency at which the points on the host surface are viewed. The greater frequency is directly related to the darker shade in this figure. For the point inspection portion of the mission, the microinspector captures images of the host surface segment numbered by *34*, which is viewed 81 times over the total number of time-steps. This figure of merit shows that with the Sun position vector along the positive X-axis in the geocentric inertial frame of reference and the microinspector traveling in a spiral trajectory, the camera on board has more opportunities to image the top portion of the host spacecraft. Therefore, the few opportunities to image the bottom of the host vehicle with natural lighting conditions must not be wasted.

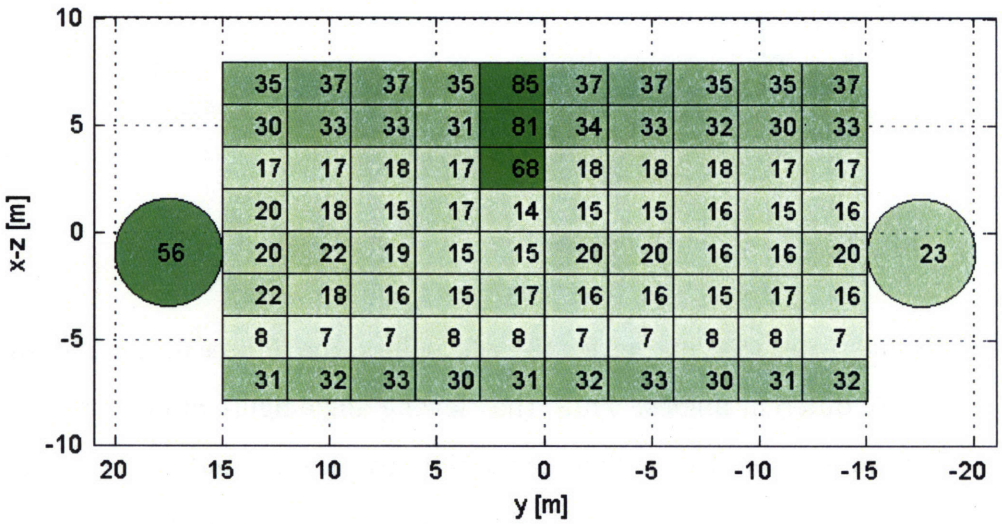

Figure 5-6: Viewing Frequency of Points on Host Surface

Figure 5-7 displays a plot of time vs. the percentage of the host surface covered by the images taken by the microinspector. As the microinspector spirals along the length of the host, the percentage of surface coverage increases gradually until 100 % is reached. This figure of merit shows that the spiral motion proves to be a good choice for an inspection trajectory. The microinspector is given the opportunity to capture images of the entire surface via the spiral trajectory, which utilizes very little fuel, as described in Section 4.2.5. A flash illuminator is not needed in this particular case.

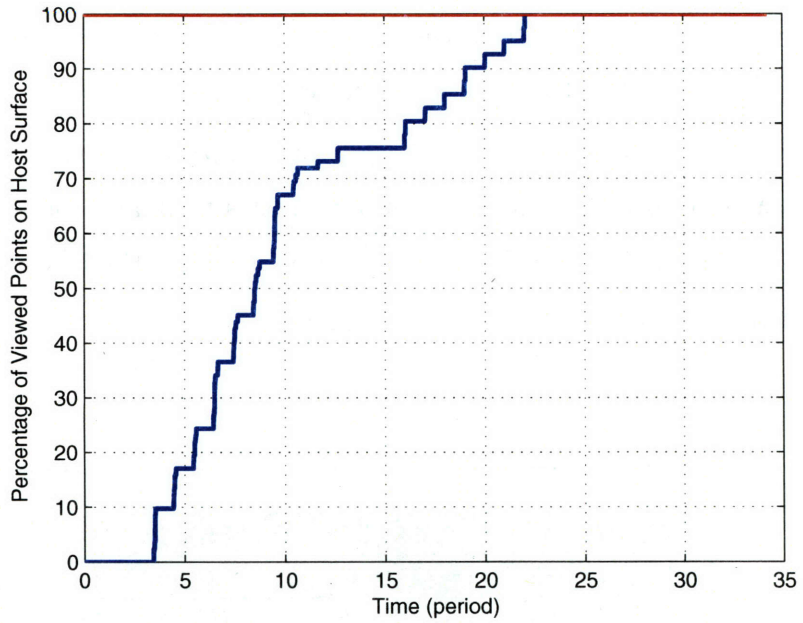

Figure 5-7: Time vs. Percentage of Host Surface Coverage

Figure 5-8 illustrates that except for the end points, the images of the host surface are at a variety of different angles. Thus, the viewing angle figure of merit shows that the trajectories chosen for the baseline simulation give the ground operators a more complete view of any damage done to the host's surface. If images of the end points at different angles are desired, the microinspector can maneuver into an inclined 2×1 ellipse and orient the attitude accordingly.

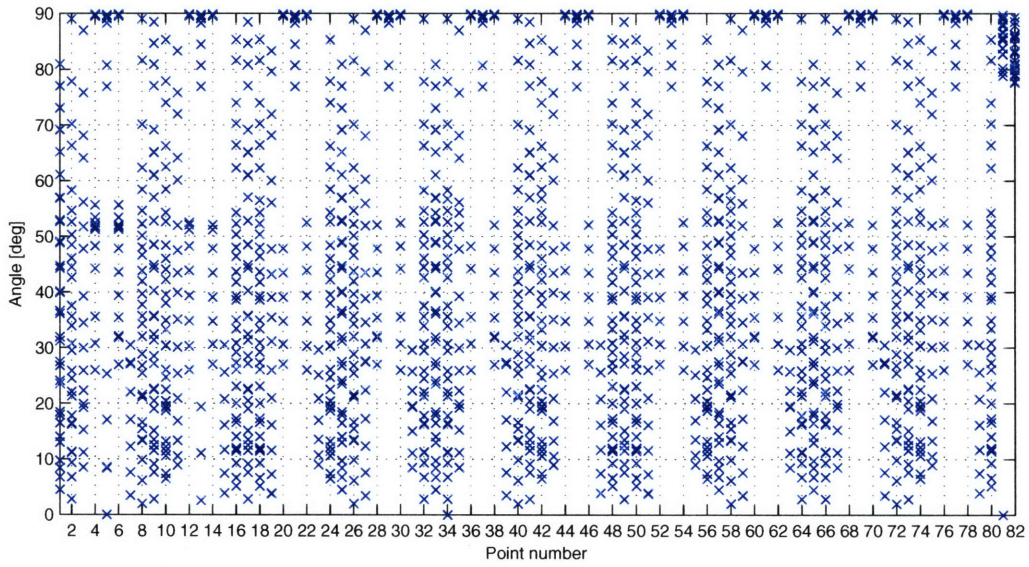

Figure 5-8: Viewing Angles for Points on Host Surface

Figure 5-9a displays the average resolution of the images that are taken throughout the mission. The average resolution of the images taken during the global inspection mode is under $1.1\,cm$, which is slightly above the desired minimum resolution of $1\,cm$. This is shown in Figure 5-9b. However, since this value is an average, the actual resolution of a surface point at the center of the field of view will be less than or equal to $1\,cm$. The average resolution of the images taken during the point inspection mode is $0.9\,cm$. Thus, this figure of merit illustrates that the images taken using the trajectories in this simulation adequately meet the image resolution requirement.

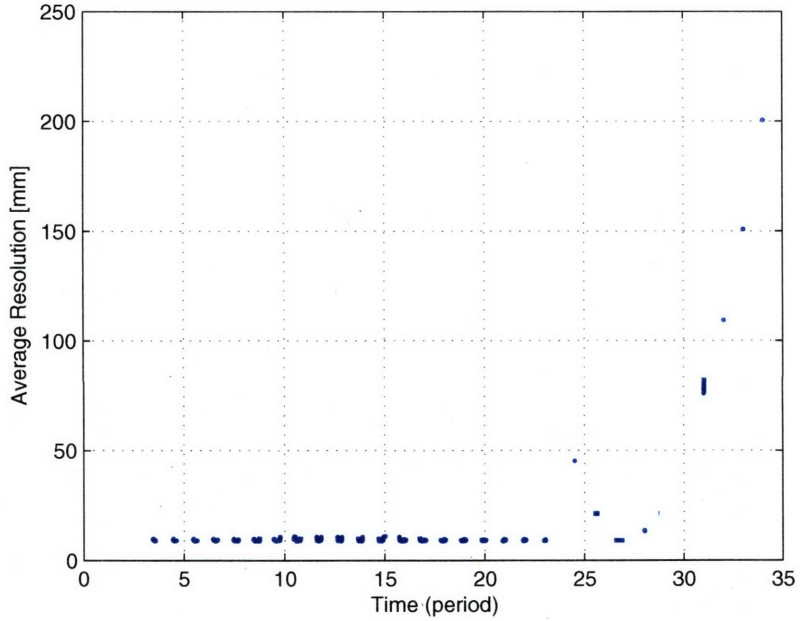

(a) Complete Mission

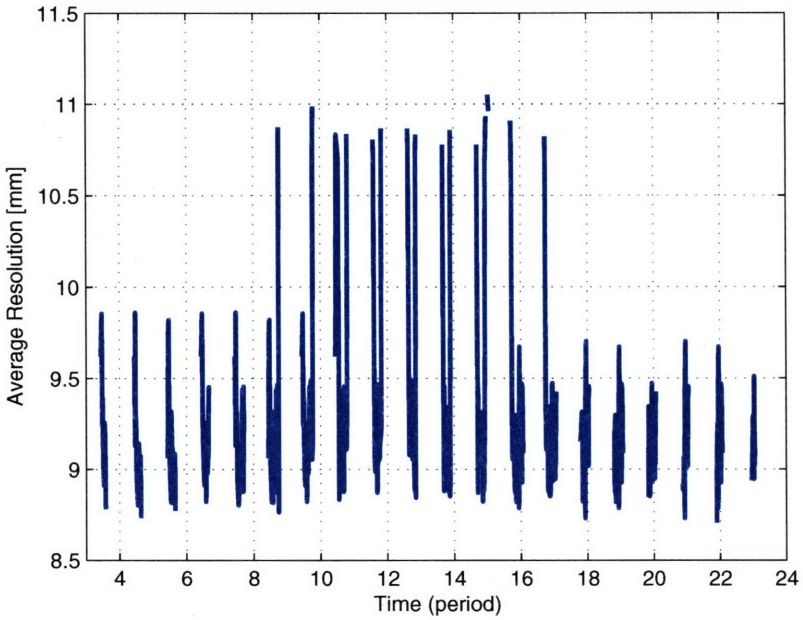

(b) Global Inspection Mode

Figure 5-9: Time vs. Average Resolution

Figure 5-10 illustrates the magnitude of the microinspector's velocity relative to the host spacecraft. The maximum speed during the global inspection mode is about $0.0327\,m/s$. According to Eqn 3.36, the maximum camera exposure time needs to be less than $0.263\,s$ at a distance of $10.1\,m$, if the desired pixel smear is less than one pixel.

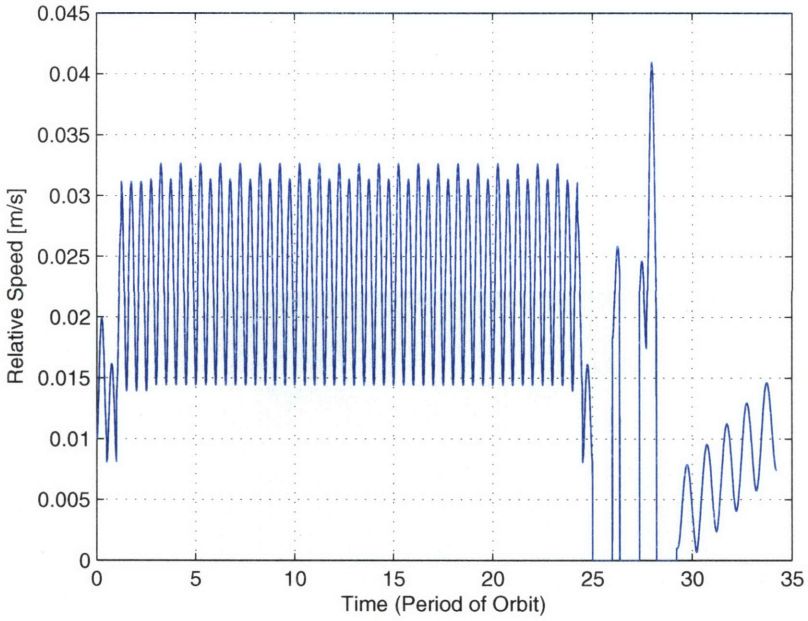

Figure 5-10: Time vs. Relative Velocity Magnitude of Microinspector

Figure 5-11 shows a plot of time vs. the sun angle. During the global inspection mode, the sun angle stays below 90°, which gives continuous Sun exposure to the solar cells. A Sun-nadir pointing algorithm may be utilized with this baseline mission may to further minimize the sun angle. However, the trade-off of such an algorithm is the high cost of fuel.

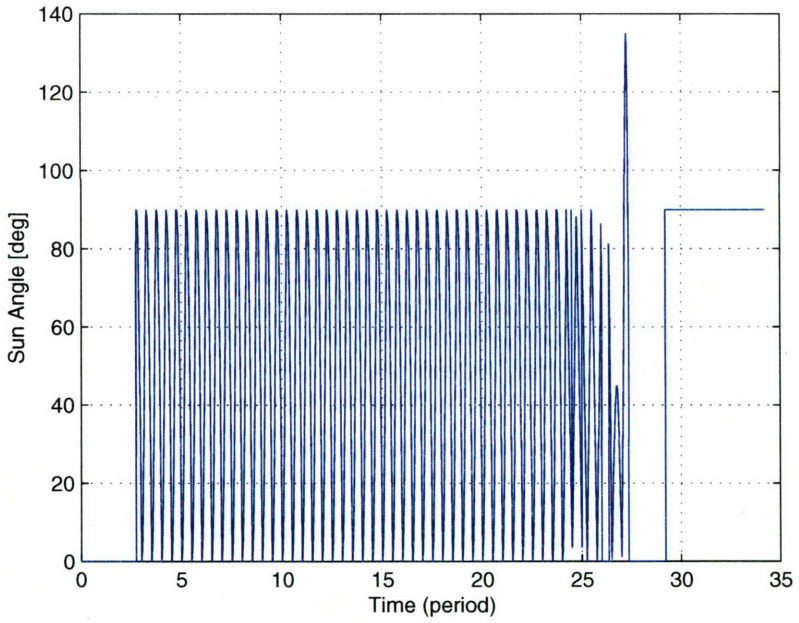

Figure 5-11: Time vs. Sun Angle

Figure 5-12 shows that the battery is drained after about five orbital periods. Thus, this result shows that the microinspector must occasionally stop its inspection process and conduct maneuvers to point at the Sun to recharge the battery. Compared to employing a Sun-nadir pointing algorithm throughout the mission, this method of battery charging increases the time needed to complete the inspection mission. However, it is much more fuel efficient, since the number of attitude maneuvers to point the solar cells toward the Sun is limited, and the fuel used to maintain the appropriate attitude is small. The Sun-nadir pointing algorithm uses much more fuel, because it must maintain the correct boresight vector orientation, while minimizing the sun angle. Without any kind of recharging scheme, the battery reserve is quickly consumed.

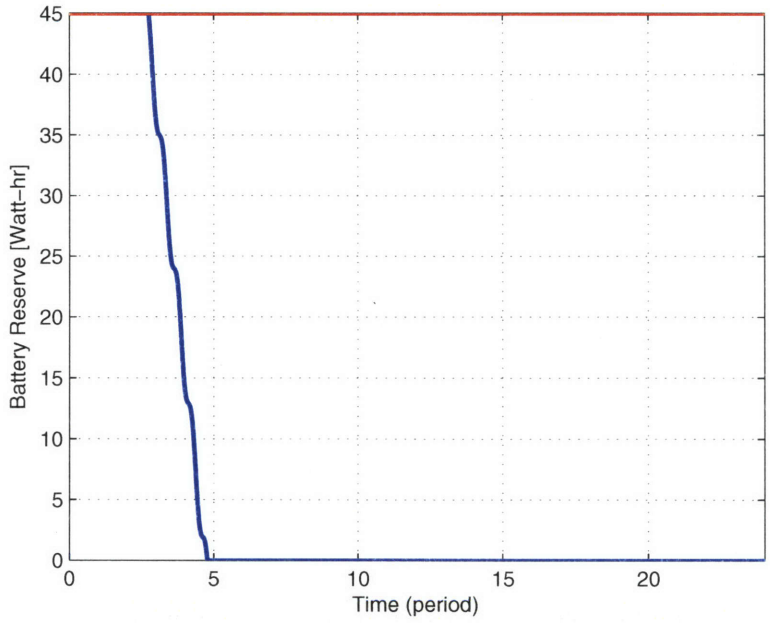

Figure 5-12: Time vs. Battery Usage

In summary, the figures of merit demonstrate that the trajectories chosen for the baseline inspection mission allow for successful inspection of the host spacecraft. The total fuel expenditure is only a little over half the available $15\,m/s$, even with the conservative rotational Δv estimate. The inspector can take images capturing the entire surface of the host by using natural sunlight alone. The image resolution requirement of $< 1\,cm$ can be attained with the $10\,m$ keep-out constraint. The exposure time of the camera must be restricted to $< 0.263\,s$. The battery reserve figure of merit shows that the microinspector must periodically halt the inspection mission and point toward the Sun to recharge the battery.

5.3 Baseline Mission Simulation: 200 km

The baseline mission for a microsatellite inspector simulated at $200\,km$ is presented in this section.

- The host spacecraft is in a circular orbit around Earth at an altitude of $200\,km$ at a 0° inclination.

- The minimum distance from the surface during imaging is $10.1\,m$, similar to the $500\,km$ case.
- The geocentric inertial Sun position vector is along the positive X-axis of the geocentric inertial reference frame.
- The spirals are $4\,m$ apart, so that the images have greater than 10 pixels of overlap, laterally.
- The total time for the inspection mission is about $35P$, where $1P = 1.577\,hr$. The time-step for the simulation is $\approx 53\,s$. This does not include the disposal mode.

The main difference between the results from this simulation at $200\,km$ and the previous simulation at $500\,km$ is the fuel consumption for translational motion. All other results are similar. The fuel expended during the entire mission for translational motion is still less than the total available Δv of $15\,m/s$, as shown in Figure 5-13a. However, the total translational Δv is much larger when compared to Figure 5-5a. This increase in fuel consumption is primarily due to the larger value of differential drag at the lower altitude. The Δv used for orbit maintenance throughout the mission is much greater at the lower altitude. The total rotational Δv estimate is nearly equivalent to the $500\,km$ case, as shown in Figure 5-13b. Figure 5-13c illustrates the total Δv used.

The maximum velocity magnitude during the global inspection mode at the lower altitude is $0.0345\,m/s$, which is slightly greater than the inspection mission at $500\,km$. This translates to a camera exposure time of less than $0.246\,s$ to attain less than one pixel smear.

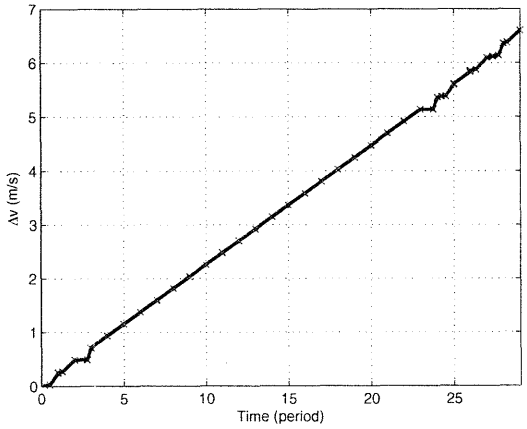

(a) Translation Δv

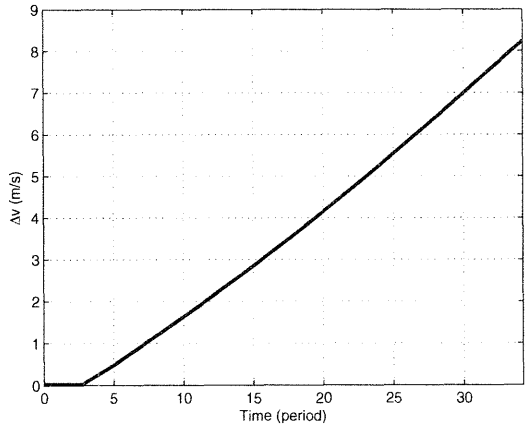

(b) Rotational Δv

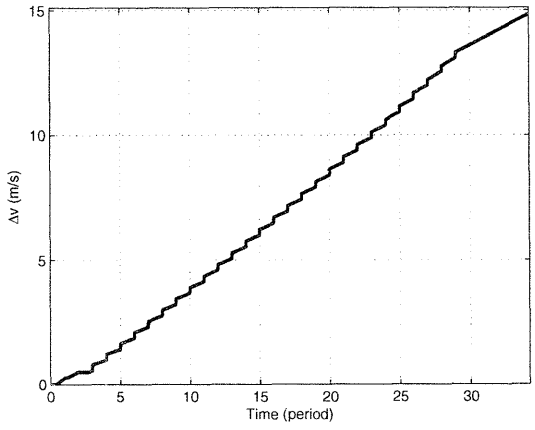

(c) Total Δv

Figure 5-13: Fuel Expenditure: Time vs. Δv

(This Page Intentionally Left Blank)

Chapter 6

Extension to Free Space

In deep space, the main source of disturbance is the gravitational or solar pressure perturbation from the Sun. However, because this source of perturbation is minuscule, it is omitted in the scope of this deep space trajectory study. With this assumption, the achievable motion about the host vehicle is contingent upon the type of trajectories that can be designed using forced motion. Natural motion is available in the deep space case, but highly impractical to use in designing inspection trajectories. Recall from Section 3.1 that the time to make one revolution in a relative closed orbit about the host vehicle is equivalent to the orbital period. In deep space, the host vehicle is essentially orbiting the Sun. A full orbit may take years. Thus, utilizing natural motion for designing trajectories would also take years — an infeasible option for inspection missions. The space environment during orbital transfer trajectories (e.g. Earth to Moon, or near Libration points) can also be considered as a deep space case.

The baseline mission for the orbiting host can be extended to this free space representation. Much like the baseline mission simulation presented in Chapter 5 for the orbiting host case, the camera on board the microinspector can capture a large percentage of the host's surface by maneuvering around the host in circular loop motions along the length. Since the loops must be shaped by forced maneuvers, a circular trajectory can only be achieved by continuous thrusting.

In order to conserve fuel, a polygon shaped trajectory with N_p sides is considered here. The N_p-sided polygon still retains the loop-like motion about the host, which

proved to be advantageous for imaging. Yet, the number of Δv burns is finite, minimizing the overall fuel expenditure. Figure 6-1 displays a segment of an equal sided polygon that could be used in shaping the inspection trajectory. r_p is the radius of the polygon, δq_p is the length of one of the the polygon sides, and θ_p is the angle between the radial lines.

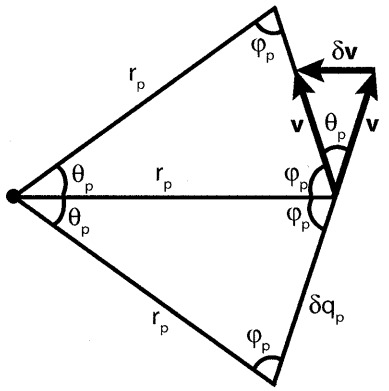

Figure 6-1: Equal-sided Polygon

From Figure 6-1, the length of one polygon side is determined by:

$$\delta q_p = 2r_p \sin\left(\frac{\theta_p}{2}\right) \tag{6.1}$$

Also from the figure, the incremental velocity magnitude to change the direction of the velocity vector, so that it is tangential to the next leg of the polygon, is given by:

$$|\delta \boldsymbol{v}| = \delta v = 2v \sin\left(\frac{\theta_p}{2}\right) \tag{6.2}$$

Let T be the total time for one revolution about the polygon. Given T, N_p, and r_p, the equation for θ_p is:

$$\theta_p = \frac{2\pi}{N_p} \tag{6.3}$$

Then, the total length of the polygon sides is:

$$q_p = 2N_p r_p \sin\left(\frac{\pi}{N_p}\right) \tag{6.4}$$

and the magnitude of the total velocity needed to make a complete revolution about the N_p-sided polygon is given by:

$$|\Delta \boldsymbol{v}| = \Delta v = 2N_p v \sin\left(\frac{\pi}{N_p}\right) \tag{6.5}$$

With q_p and T, the magnitude of the velocity on each leg of the polygon is:

$$|\boldsymbol{v}| = v = \frac{q_p}{T} \tag{6.6}$$

By substituting Eqn 6.6 for v into Eqn 6.5, Δv can be rewritten as:

$$\begin{aligned} \Delta v &= 2N_p \left(\frac{2N_p r_p \sin\left(\frac{\pi}{N_p}\right)}{T} \right) \sin\left(\frac{\pi}{N_p}\right) \\ &= \frac{4r_p}{T} {N_p}^2 \sin^2\left(\frac{\pi}{N_p}\right) \end{aligned} \tag{6.7}$$

Eqn 6.7 is observed to have a limit, which is given by:

$$\lim_{N_p \to \infty} \Delta v = \frac{4\pi^2 r_p}{T} \tag{6.8}$$

The size of the polygon is dictated by r_p. By Eqn 6.7, it is seen that fuel use increases linearly with respect to r_p, given equivalent values for T and N_p. With the same value for T, fuel expenditure can also be expected to increase when the number of sides is increased. However, by Eqn 6.8, a limit is reached as $N_p \to \infty$. This limit is equal to the fuel expended traversing in a circle via continuous thrust.

Figure 6-2 illustrates a simulation of the trajectories generated for global inspection in deep space. Each polygon has $N_p = 6$ sides. The trajectory around the host vehicle has a maximum distance of $r_{max} = 20\,m$ from the y-axis and completes one revolution in $1\,hr$. The total translational Δv to conduct this part of the mission is $1.73\,m/s$. The Δv at each corner of the polygon to complete a revolution in $1\,hr$ has a magnitude of $0.034\,m/s$.

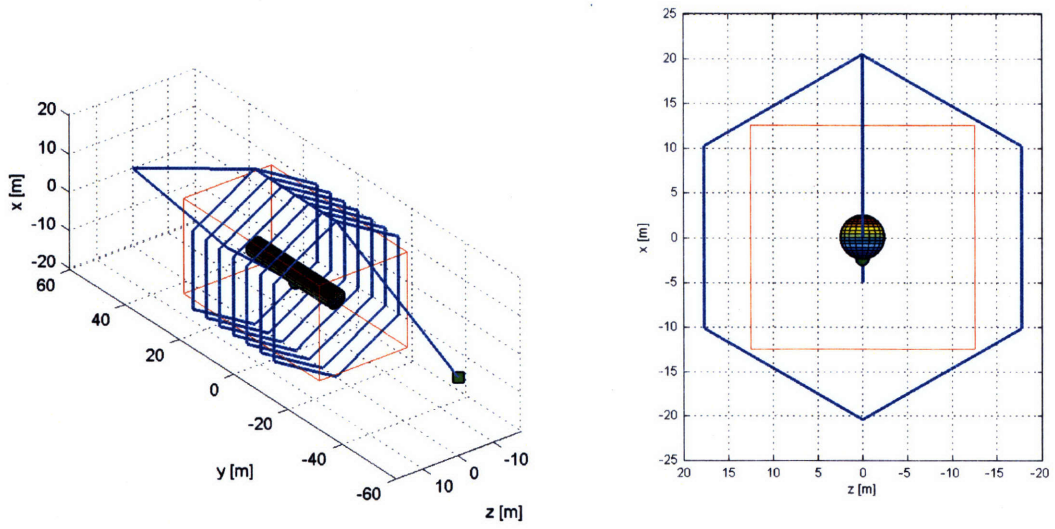

(a) 3D

(b) x-z View

Figure 6-2: Deep Space Case 1: $N_p = 6$, $r_{max} = 20\,m$, 1 revolution in $1\,hr$.

Figure 6-3 displays the global inspection mission when the number of sides of the polygons is increased to ten. The trajectory around the host vehicle still has a maximum distance of $r_{max} = 20\,m$ from the y-axis, and completes one revolution in $1\,hr$. The total translational Δv to complete this part of the mission is $1.88\,m/s$. As expected, the fuel expenditure has increased with the larger number of sides. Changing N_p from six to ten results in a $0.15\,m/s$ increase in fuel expenditure. The Δv burn at each corner of the polygon to complete a revolution in $1\,hr$ takes $0.021\,m/s$.

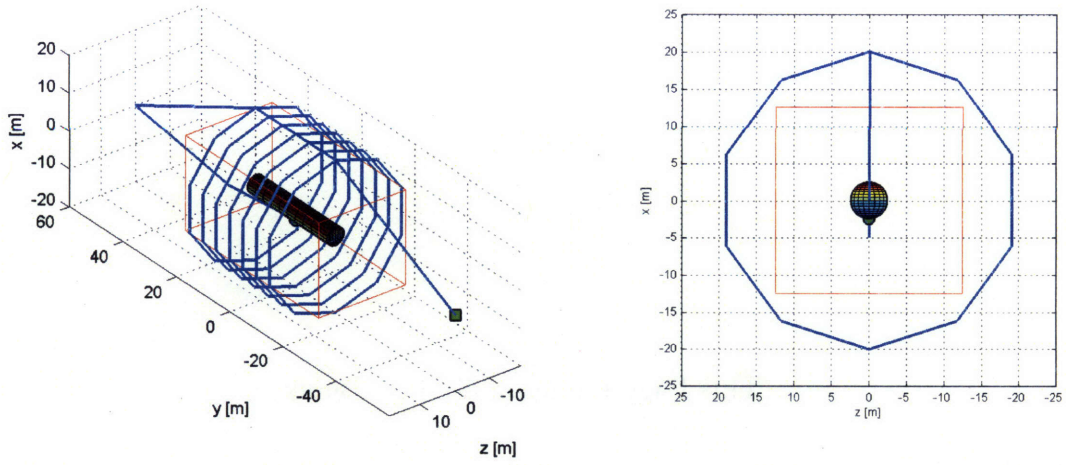

(a) 3D

(b) x-z View

Figure 6-3: Deep Space Case 2: $N_p = 10$, $r_{max} = 20\,m$, 1 revolution in $1\,hr$.

The same figures of merit used to characterize the baseline mission in Chapter 5 may also be utilized to rate the inspection quality of the deep space microinspector mission.

(This Page Intentionally Left Blank)

Chapter 7

Conclusions

This chapter summarizes the results of the trajectory and mission study conducted for a microsatellite inspector.

7.1 Thesis Summary

A trajectory analysis for the mission design of a microsatellite inspector vehicle was conducted and presented in this thesis. The study covered two mission scenarios — Earth orbiting and deep space. For the orbiting case, a natural motion trajectory for inspection of the host spacecraft was primarily designed utilizing the solution to the *CW* equations. The key factors affecting an inspection mission were discussed and detailed in this thesis. The relative motion space was first explored via the *CW* solution. From this analysis, a toolset of trajectories that would potentially be useful for vehicle inspection was developed. The methods, used in this thesis, for calculating the transfer motion between these trajectories were also based on the *CW* solution.

A baseline mission design concept for a microinspector was presented, which consisted of a deployment mode, a global inspection mode, a point inspection mode, and a disposal mode. The 3DOF simulation of the baseline mission was based on the trajectory toolset and transfer methods. The altitude and inclination of the host spacecraft's orbit about Earth had to be specified for the simulation. The attitude of the microinspector was not simulated; however, the fuel usage by the attitude control

system was estimated by assuming an angular position bang-bang controller. Factors that could be used to score the successfulness of an inspection mission were also outlined. These figures of merit were used to show the effectiveness of the chosen baseline inspection mission. The hardware requirements and constraints employed in the simulation were based on JPL's microinspector design.

Simulations of the baseline inspection mission were conducted for LEO at altitudes of $500\,km$ and $200\,km$. The main conclusion for these scenarios was that the attitude motion consumed considerably more fuel than the translational motion at altitudes higher than $200\,km$. The total available Δv of $15\,m/s$ was found to be more than adequate for the entire mission at both altitudes. In order to accurately estimate the fuel expenditure for attitude control, it is recommended that a six-degree-of-freedom simulation of the microinspector's orbital motion and attitude be developed, with fuel optimizing attitude control techniques. It was determined that to complete the inspection mission, the microinspector needs to periodically take time out of its inspection tasks and recharge the batteries by pointing at the Sun. The simulated baseline mission was able to attain image resolutions that were less than or equal to the desired maximum resolution of $1\,cm$, during the global inspection and point inspection mode. The minimum distance avoidance constraint of $10\,m$ was not violated in achieving this imaging goal. The maximum relative velocity magnitude for both the $500\,km$ and $200\,km$ altitude cases in the baseline mission simulation showed that the camera exposure time should be less than $0.5\,s$ to achieve less than one pixel smear.

In the deep space scenario, the natural motion dynamics were found to be too slow to be useful. Forced motion was employed to design the trajectories for this case. Because the spiraling motion – which was employed in the Earth orbiting scenario – proved to be advantageous for capturing images of the complete surface of the host, a similar concept was used in the deep space scenario. An N_p-sided polygon was utilized to mimic the looping motion about the host vehicle. Given a constant revolution time, it was shown that an increase in the number of sides correlated directly with an increase in fuel expenditure. As N approaches infinity, the shape of

the polygon approaches a circle. The Δv amount also approaches the total Δv for continuous thrusting in a circle about the host vehicle. The global inspection concept utilizing the polygon method of trajectory design was shown in this thesis.

7.2 Future Work

In this thesis, the attitude of the microinspector was not explicitly simulated. In order to better understand the coupling effects between the orbital and attitude dynamics, the author recommends a full six-degree-of-freedom simulation be developed and analyzed, using the baseline inspection mission presented in this thesis. A Sun-nadir angular position controller can be specifically implemented to accurately estimate the fuel costs and battery usage.

Additionally, a trades-analysis on the different microinspector hardware specifications for the baseline mission is needed. Depending on the microinspector's design, the trajectories for an inspection mission may vary drastically from the baseline mission discussed in this thesis. The baseline mission simulation must also be conducted for host vehicles at higher altitudes, to test the effectiveness of the inspection trajectories.

From the results of the baseline mission simulation, it was concluded that the rotational Δv for attitude control was the main source of fuel consumption in Earth orbiting scenarios at altitudes $> 200\,km$. Since a continuous Sun-nadir pointing scheme requires complicated attitude maneuvers, this translates directly to high fuel consumption. This continuous charging method may not even be necessary depending on the capacity of the battery. Thus, there is an obvious need for a trade study between continuous charging via the Sun-nadir pointing algorithm and periodically taking time out from the inspection mission to point the solar cells at the Sun.

Only a cylindrical-shaped model of a host spacecraft was used in the baseline mission simulation. Further studies need to be conducted utilizing a range of different host spacecraft models. Another important case to be examined is if the host spacecraft is rotating or tumbling in the LVRCS.

The different spacecraft models and hardware specifications will affect the value for differential drag. The constant differential drag assumption is no longer valid when the attitude of the host spacecraft and microinspector are continuously changing in the LVRCS. Thus, a model of the differential drag that accounts for these changing values is needed.

The simulations in this thesis only used the box keep-out zone in developing the trajectories. There are many other keep-out zone models that can be implemented with the simulations, such as a spherical or cylindrical model keep-out zone. These avoidance constraints can be integrated with the trajectory designs from this thesis. For irregularly shaped host vehicles, more attention needs to be given to avoiding the keep-out zone during transfer planning.

The baseline mission simulation presented here can be extended to other planet orbiting scenarios. The gravitational, solar, and atmospheric disturbances may differ significantly from the Earth orbiting case, which directly affects fuel expenditure, battery usage, and imaging. Furthermore, the deep space mission concept presented in this thesis needs to be simulated, as in the Earth orbiting case. The same figures of merit can be applied to describe the quality of the inspection mission designed for the host in consideration.

Each figure of merit needs to be assigned a weighting factor, when rating the inspection mission. The weighting factor depends on the type of host vehicle, as well as the goals of the mission. A study on how to develop the weighting factors must be carried out in order to determine the best inspection mission for a particular host vehicle.

Appendix A

Characterization of all Closed Relative Orbits

If X_0 is zero, then the relative motion appears to stay stationary in the LVRCS. This stationary relative motion will be referred to as a *closed relative orbit* throughout this thesis. All closed relative orbits have a period equal to the orbital period of the host vehicle. This fact is readily supported by the *CW* solution. Given the value of the semiminor axis, b, a 2×1 elliptical cylinder, whose length is in the z-axis, can be defined. The closed relative orbits that can be achieved may be described by plane slices through this 2×1 elliptical cylinder and the desired Y_0, as illustrated conceptually in Figure A-1. Consequently, the closed relative orbit cannot expressly be in the x-z or y-z plane in the LVRCF.

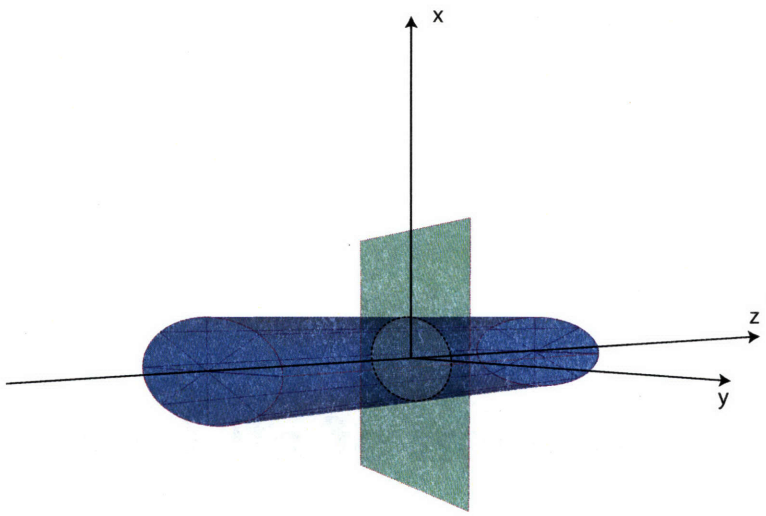

Figure A-1: Plane Slice through 2×1 Elliptical Cylinder

Each closed relative orbit can be characterized by its normal vector, which is parallel to the "angular momentum" direction of the relative motion. Two angles, α and β, can be used to define this unit normal vector. Thus, all closed relative orbits can also be characterized by these two angles alone. The normal vector and the two angles are measured from the center of the closed relative orbits. Figure A-2 shows a diagram of a 2×1 elliptical cylinder, a unit normal vector, and a graphical depiction of the α and β angles.

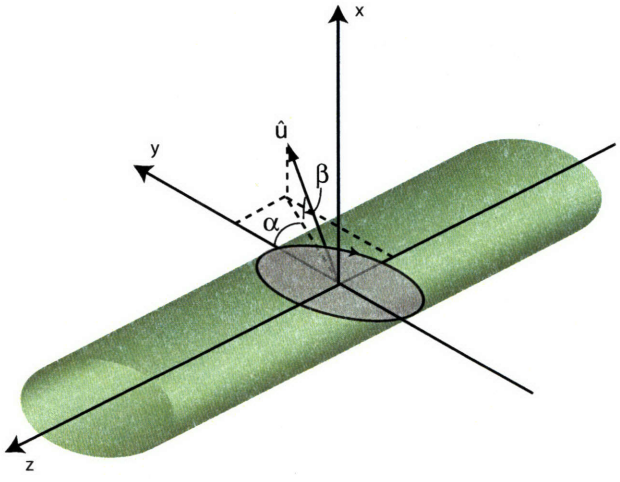

Figure A-2: Characterization of Closed Relative Orbits

To correlate the α and β angles with the parameters of the traveling ellipse formulation of the *CW* solution, notice that the equation for the relative orbit's angular momentum vector may be employed in place of the unit normal vector. Recalling the equations for $\boldsymbol{r}$ and $\boldsymbol{v}$ from Eqn 3.8 and Eqn 3.9, the traveling ellipse formula for the initial position, $\boldsymbol{r}_0$, and velocity, $\boldsymbol{v}_0$, for a closed relative orbit may be obtained by setting $t = 0$ and $X_0 = 0$. Simplifying further, Y_0 is set to zero, since the two angles are measured from the center of the closed orbit, and the differential accelerations are set to zero. Applying this set of values gives the following formula for $\boldsymbol{r}_0$ and $\boldsymbol{v}_0$:

$$\boldsymbol{r}_0 = \begin{bmatrix} x_0 \\ y_0 \\ z_0 \end{bmatrix} = \begin{bmatrix} b\sin(\phi) \\ 2b\cos(\phi) \\ c\sin(\psi) \end{bmatrix} \tag{A.1}$$

$$\boldsymbol{v}_0 = \begin{bmatrix} \dot{x}_0 \\ \dot{y}_0 \\ \dot{z}_0 \end{bmatrix} = \begin{bmatrix} b\omega\cos(\phi) \\ -2b\omega\sin(\phi) \\ c\omega\cos(\psi) \end{bmatrix} \tag{A.2}$$

The angular momentum vector, $\boldsymbol{h}$, at $t = 0$ is given by:

$$\begin{aligned} \boldsymbol{h} = \boldsymbol{r}_0 \times \boldsymbol{v}_0 &= \begin{vmatrix} \hat{i} & \hat{j} & \hat{k} \\ b\sin(\phi) & 2b\cos(\phi) & c\sin(\psi) \\ b\omega\cos(\phi) & 2b\omega\sin(\phi) & c\omega\cos(\psi) \end{vmatrix} \\ &= \begin{bmatrix} 2bc\omega\cos(\phi-\psi) \\ -bc\omega\sin(\phi-\psi) \\ -2b^2\omega \end{bmatrix} \\ &= \begin{bmatrix} h_x \\ h_y \\ h_z \end{bmatrix} \end{aligned} \tag{A.3}$$

The α and β angles characterizing this closed relative orbit can be determined geometrically from the angular momentum terms in Eqn A.3.

$$\tan(\alpha) = -\frac{h_z}{h_y} = \frac{-2b^2\omega}{-bc\omega\sin(\phi-\psi)} = \frac{2b}{c\sin(\phi-\psi)} \tag{A.4}$$

$$\begin{aligned}\tan(\beta) &= \frac{h_x}{\sqrt{h_y^2+h_z^2}} \\ &= \frac{2bc\omega\cos(\phi-\psi)}{\sqrt{(-bc\omega\sin(\phi-\psi))^2+(-2b^2\omega)^2}} \\ &= \frac{2c\cos(\phi-\psi)}{\sqrt{c^2\sin^2(\phi-\psi)+4b^2}}\end{aligned} \tag{A.5}$$

From Eqn A.4 and Eqn A.5, equations that correlate the α and β angles with $(\phi-\psi)$ and c can be found:

$$\tan(\phi-\psi) = 2\frac{\cos(\alpha)}{\tan(\beta)} \tag{A.6}$$

$$c = \frac{b}{\sin(\alpha)}\sqrt{\tan^2(\beta)+4\cos^2(\alpha)} \tag{A.7}$$

Therefore, if the unit normal of the desired closed loop, or the desired α and β angles are known, the constraint for ϕ and ψ, and the out-of-plane amplitude c can be calculated for a chosen b and vice versa.

By inspection and also as an outcome of Eqn A.6–A.7, there exists some constraints on the α and β angles, shown in Eqn A.8–A.9.

$$\alpha \neq 0, \pi \tag{A.8}$$

$$\beta \neq 0, \pm\frac{\pi}{2} \tag{A.9}$$

Appendix B

Relationship Between *CW* Solution Parameters and Orbital Elements

The *CW* solution is based on a host vehicle that is in a circular orbit about the planet. If the secondary vehicle's orbit is in the same orbital plane as the host, then the orbital elements describing this orbit can easily be related to the *CW* solution parameters. A full description of the orbital elements can be found in Chapter 3 of Battin's *An Introduction to the Mathematics and Methods of Astrodynamics* [19]. Given the semiminor axis of a 2×1 elliptical relative orbit, b', and the radius of the host's circular orbit, r_h, the orbital elements of the microinspector's orbit about the planet can be determined. The computation of a few of these orbital elements relating to the traveling ellipse parameters is discussed in this section. Table B.1 gives a description of these orbital elements.

Table B.1: Description of Orbital Elements

Parameter	Description
a	Semimajor axis of microinspector's orbit
b	Semiminor axis of microinspector's orbit
e	Eccentricity of microinspector's orbit
r_p	Pericenter radius
r_a	Apocenter radius
r_h	Radius of host's circular orbit

Figure B-1 shows the orbits of the host and microinspector about the Earth. The microinspector's orbit correlates to a 2×1 ellipse in the LVRCS. The size of the orbits is exaggerated in the figure to elucidate the parameter descriptions.

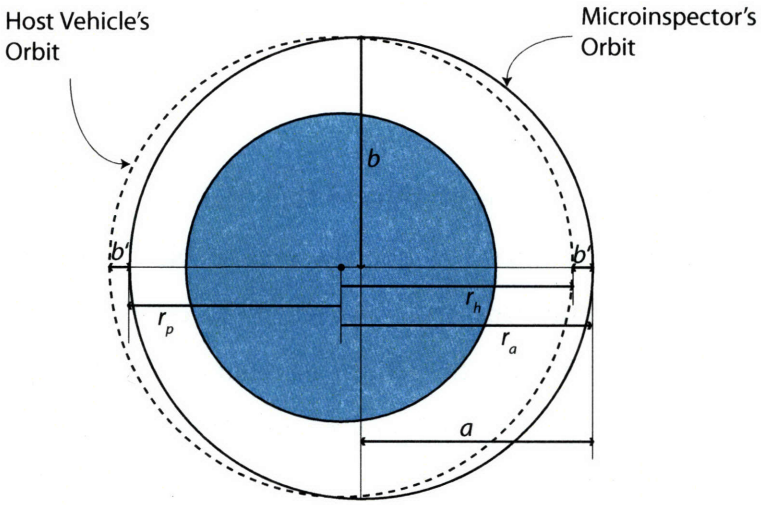

Figure B-1: Secondary Vehicle's Orbital Elements

As shown in Figure B-1, the relationship between the 2×1 ellipse's semiminor axis, b', and the radius of the the host orbit's circular orbit, r_h, to the pericenter radius, r_p, and apocenter radius, r_a, is given by:

$$r_p = r_h - b' \tag{B.1}$$

$$r_a = r_h + b' \tag{B.2}$$

The formulas relating r_p and r_a to the orbit's semimajor axis, a, and semiminor axis, b are given by:

$$a = \frac{1}{2}(r_p + r_a) \tag{B.3}$$

$$b = \sqrt{r_p r_a} \tag{B.4}$$

Substituting Eqn B.1–B.2 into Eqn B.3 and Eqn B.4,

$$\begin{aligned} a &= \frac{1}{2}(r_p + r_a) \\ &= \frac{1}{2}(r_h - b' + r_h + b') \\ &= r_h \end{aligned} \tag{B.5}$$

and

$$\begin{aligned} b &= \sqrt{r_p r_a} \\ &= \sqrt{(r_h - b')(r_h + b')} \\ &= \sqrt{r_h^2 - b'^2} \end{aligned} \tag{B.6}$$

Also, from the formula relating b, a, and the eccentricity, e, shown by Eqn B.7, a relationship between b, b', and r_h can be found.

$$b^2 = \left| a^2 \left(1 - e^2\right) \right| \tag{B.7}$$

Substituting the results of Eqn B.5–B.6 into Eqn B.7, the following relation is found:

$$e^2 = 1 - \frac{b^2}{a^2} = \frac{b'^2}{r_h^2} \tag{B.8}$$

The period of an elliptical orbit about a planet may be obtained by applying

Kepler's second law, which gives the time required for the radius vector to sweep over the entire enclosed area. The equation for the period is given by:

$$P = 2\pi\sqrt{\frac{a^3}{\mu}} \tag{B.9}$$

where μ is the gravitational parameter of the planet.

Since the semimajor axis of the microinspector's orbit is equal to the radius length of the host's circular orbit, by Eqn B.5, the orbital period is the same for the host and the microinspector. Thus, all closed relative orbits of the microinspector about the host has the same period as the orbital period of the host and microinspector.

The magnitude of the velocity at any given point on the orbit can be determined from the *energy integral*, sometimes called the *vis-viva integral*, which is given by Eqn B.10.

$$v^2 = \mu\left(\frac{2}{r} - \frac{1}{a}\right) \tag{B.10}$$

The vis-viva integral reveals the relationship between the velocity magnitude and the semimajor axis, a. In Section 3.1.2, it was stated that for a traveling ellipse, the secondary vehicle appears to move forward or backward in relation to the host vehicle because its velocity is greater than or less than that of the host, respectively. This statement is validated by Eqn B.10. a is the same for both orbits by Eqn B.5. If r for the microinspector's orbit is greater than r_h, then the magnitude of the velocity will be less. Thus, the microinspector will move backward relative to the host vehicle due to the lesser velocity. Conversely, if r is less than r_h, then the velocity magnitude will be greater. Hence, the microinspector moves faster than the host vehicle, appearing to move forward.

In Figure B-2, the velocity vectors of the host and microinspector are illustrated in the LVRCS, where the host is centered at the origin. $\boldsymbol{r_h}$ is the position vector from the Earth to the host vehicle in the geocentric reference frame. $\boldsymbol{\omega}$ is the orbital velocity of the host. $\boldsymbol{v_h}$ is the velocity vector of the host and $\boldsymbol{v_i}$ is the velocity vector of the microinspector, both in the geocentric reference frame. $\Delta\boldsymbol{v_i}$ is the velocity

vector of the microinspector in the LVRCS.

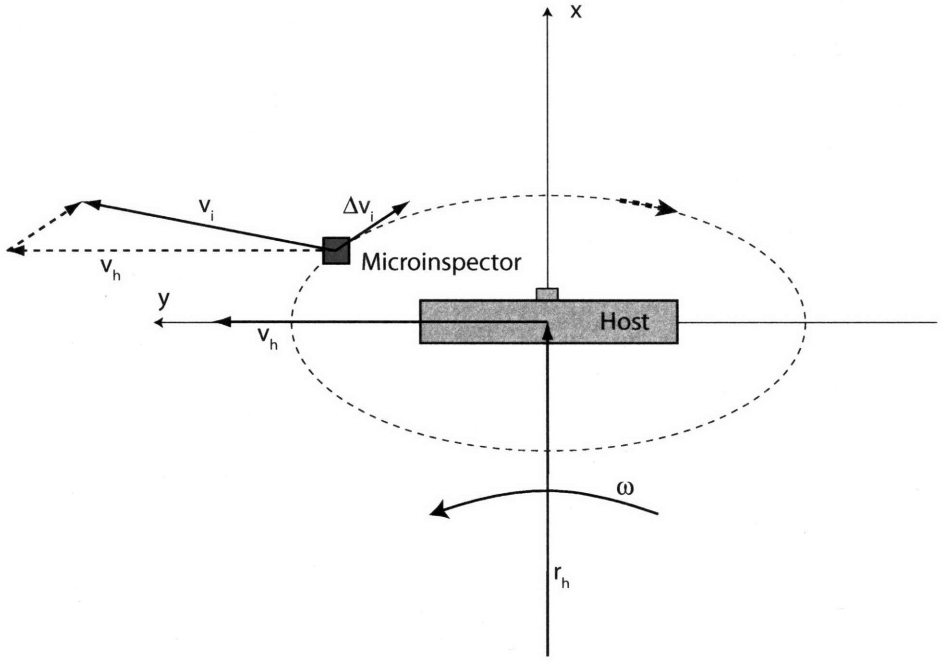

Figure B-2: Velocity of Host and Inspector in LVRCS

The host vehicle's velocity vector is given by:

$$\boldsymbol{v}_h = \boldsymbol{\omega} \times \boldsymbol{r}_h \tag{B.11}$$

One can also interpret the host's velocity as the velocity of the origin of the LVRCS. Therefore, the microinspector's total velocity, $\boldsymbol{v}_i$, is just the sum of the host's velocity (velocity of the origin of the LVRCS) and the velocity of the microinspector relative to the host vehicle.

Let $\boldsymbol{v}_i = [v_x, v_y, v_z]$. Then, from Figure B-2, we see that v_y will primarily be composed of v_h. In the 2×1 ellipse, this is the largest factor in the microinspector's total velocity, which implies that $v_y >> v_x, v_z, \Delta v$. The calculations below show the magnitude of the microinspector's total velocity after Δv is applied separately along the x-axis and y-axis in the LVRCS. For Δv applied along the x-axis,

$$v = \sqrt{(v_x + \Delta v)^2 + {v_y}^2 + {v_z}^2} = \sqrt{{v_x}^2 + 2v_x\Delta v + \Delta v^2 + {v_y}^2 + {v_z}^2} \tag{B.12}$$

For Δv applied along the y-axis,

$$v = \sqrt{{v_x}^2 + (v_y + \Delta v)^2 + {v_z}^2} = \sqrt{{v_x}^2 + {v_y}^2 + 2v_y\Delta v + \Delta v^2 + {v_z}^2} \tag{B.13}$$

Comparing the two results, it is apparent that the magnitude of the total velocity is optimally changed when Δv is applied parallel to the V-bar, since $2v_y\Delta v >> 2v_x\Delta v$. Directing Δv in any other direction decreases the variation in magnitude. Thus, to conserve fuel when changing the forwards or backwards motion of the microinspector in relation to the host, the impulse velocity, Δv, must be applied parallel to the V-bar (y-axis) in the LVRCS. Applying Δv in the manner will effectively change the semimajor axis, a, and consequently the period, determined from Eqn B.9. More specifically, applying Δv in the positive y-direction increases a, and the 2×1 ellipse travels in the negative y-direction. Applying Δv in the negative y-direction decreases a, and the 2×1 ellipse travels in the positive y direction. Figure B-3–B-4 illustrate these findings. Figure B-3 shows the resulting motion when Δv =0.01 m/s is applied when $\phi = 0°$ on the 2×1 ellipse. Figure B-4 shows the resulting motion when Δv =0.01 m/s is applied when $\phi = 90°$ on the 2×1 ellipse. The 2×1 ellipse about the host vehicle has a semiminor axis of 20 m.

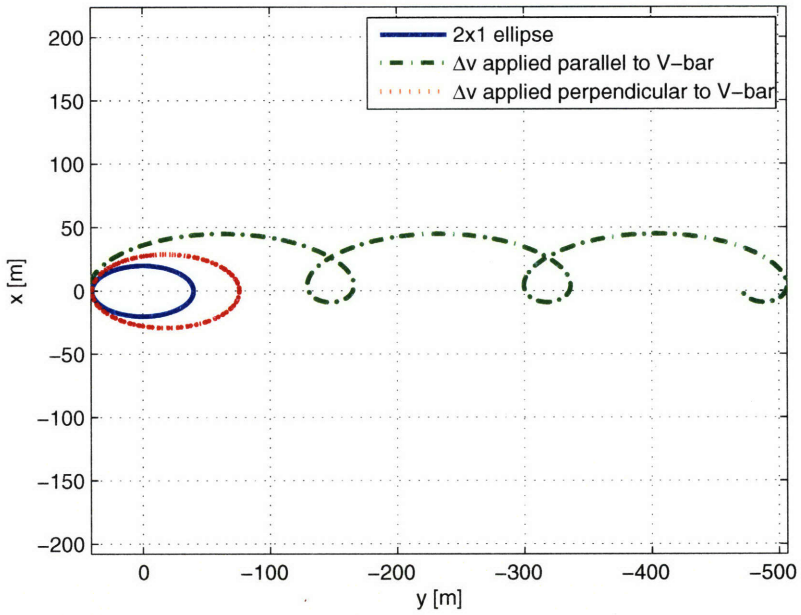

Figure B-3: Δv applied when $\phi = 0°$

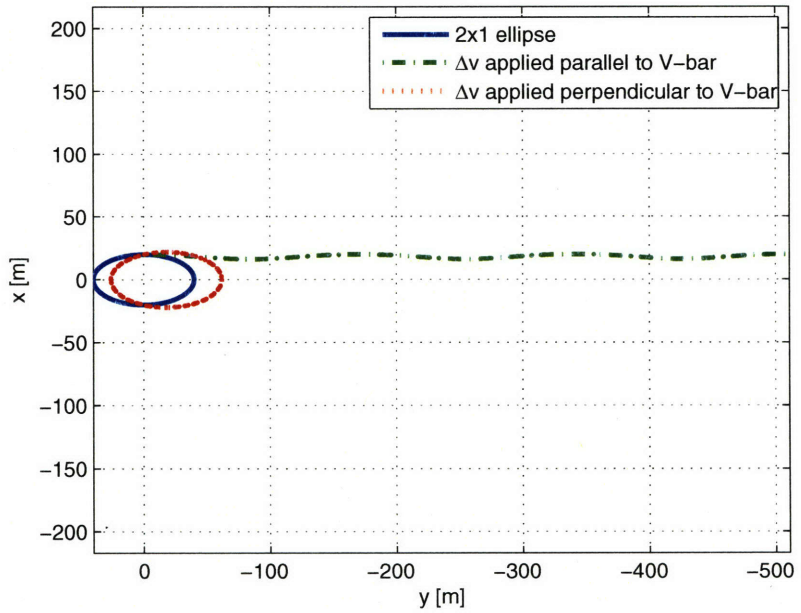

Figure B-4: Δv applied when $\phi = 90°$

For both figures, when Δv is applied in the positive y-direction, the semimajor axis, a, and the period of the microinspector's orbit about Earth are increased, causing the microinspector to appear as if it is moving behind the host in the LVRCS. When Δv is applied in the positive x-direction, a and the period are also increased in this case, but by a significantly smaller amount. X_0 is not changed for this particular orbit because the relative initial velocity on the y-axis ($\dot{y}_0$) is unchanged. However, Y_0 and b' are changed due to the difference in initial velocity along the x-axis ($\dot{x}_0$). Refer to Eqn 3.11 for descriptions of the traveling ellipse parameters[‡].

[‡]Note that b in Eqn 3.11 is the same as b' used here. b is used for the semiminor axis of the microinspector's orbit about the Earth in this section.

Appendix C

Acronyms

ISS – International Space Station

CEV – Crew Exploration Vehicle

GN&C – Guidance, Navigation, and Control

SSC – Surrey Space Centre

SSTL – Surrey Satellite Technology Limited

SNAP-1 – Surrey Nanosatellite Applications Platform

AFRL – Air Force Research Laboratory

JPL – Jet Propulsion Laboratory

Mini-AERcam – Miniature Autonomous Extravehicular Robotic Camera

JSC – NASA Johnson Space Center

LEO – Low Earth Orbit

CW – Clohessy-Wiltshire

IMU – Inertial Measurement Unit

ACS – Attitude Control System

LVLH – Local-vertical Local-horizontal

LVRCS – Local-vertical Rotating Coordinate System

SOC – State of Charge

FOV – Field of View

(This Page Intentionally Left Blank)

Bibliography

[1] S. E. Fredrickson, L. W. Abbott, S. Duran, J. D. Jochim, J. W. Studak, J. D. Wagenknecht, and N. M. Williams, "Mini AERCam: Development of a Free Flying Nanosatellite Inspection Robot," in *Space Systems Technology and Operations*, ser. SPIE, vol. 5088, Orlando, FL, Apr. 24, 2003, pp. 97–111.

[2] J. G. Macke, D. P. Miller, M. A. Swartwout, K. J. Bennett, and W. D. Smart, "Deployable Inspector Spacecraft for Distributed Field Measurements," in *22nd AIAA International Communications Satellite Systems Conference and Exhibit 2004*, Monterey, CA, May 9-12, 2004, paper AIAA 2004-3152.

[3] A. Jacobovits and T. W. Vaneck, "AeroAstro's Escort - A Microsatellite for On-Orbit Inspection of Space Assets," in *17th Annual AIAA/USU Conference on Small Satellites*, Logan, UT, 2003.

[4] C. Underwood, G. Richardson, and J. Savignol, "SNAP-1: A Low Cost Modular COTS-based Nano-satellite – Design, Construction, Launch and Eearly Operations Phase," in *15th AIAA/USU Conference on Small Satellites*, Logan, UT, Aug.13-16, 2001.

[5] W. H. Steyn and Y. Hashida, "In-orbit Attitude Performance of the 3-axis Stabilised SNAP-1 Nanosatellite," in *15th AIAA/USU Conference on Small Satellites*, Logan, UT, Aug.13-16, 2001.

[6] D. Gibbon and C. Underwood, "Low Cost Butane Propulsion Systems for Small Spacecraft," in *15th AIAA/USU Conference on Small Satellites*, Logan, UT, Aug.13-16, 2001.

[7] R. Lancaster and C. Underwood, "SNAP-1 Machine Vision System," in *AIAA/USU Annual Conference on Small Satellites, 12th*, Logan, UT, Aug.21-24, 2000.

[8] "XSS-10 Microsatellite Flight Demonstration Program," *AFRL Technology Horizons*, vol. 5, pp. 10–12, Dec. 2004.

[9] "XSS-10 Micro Satellite," http://www.vs.afrl.af.mil/, Feb. 2005, date of Access: Mar 16, 2006.

[10] "XSS-11 Micro Satellite," http://www.vs.afrl.af.mil/, Dec. 2005, date of Access: Mar 16, 2006.

[11] J. Mueller, H. Goldberg, and L. Alkalai, "Micro-Inspector Spacecraft for Space Exploration Missions and Beyond," in *Space Technology & Applications International Forum*, Albequerque, NM, Feb.14, 2006.

[12] S. E. Fredrickson, S. Duran, and J. D. Mitchell, "Mini AERCam Inspection Robot for Human Space Missions," in *Space 2004 Conference and Exhibit*, San Diego, CA, Sept.28-30, 2004, paper AIAA Paper 2004-5843, pp. 1–9.

[13] "Space Systems Labs: CUSat Satellite Project," http://cusat.cornell.edu/, date of Access: Mar 17, 2006.

[14] M. Swartwout, J. Macke, K. Bennett, and W. Smart, "The Bandit: An Automated Vision-Navigated Inspector Spacecraft," in *17th Annual AIAA/USU Conference on Small Satellites*, Logan, UT, 2003.

[15] A. Richards, T. Schouwenaars, J. P. How, and E. Feron, "Spacecraft Trajectory Planning with Avoidance Constraints Using Mixed-Integer Linear Programming," *Journal of Guidance, Control, and Dynamics*, vol. 25, no. 4, pp. 755–764, July 2002.

[16] W. H. Clohessy and R. S. Wiltshire, "Terminal Guidance System for Satellite Rendezvous," *Journal of the Aerospace Sciences*, vol. 27, no. 9, pp. 653–658, 1960.

[17] D. A. Vallado, *Fundamentals of Astrodynamics and Applications*, 2nd ed. El Segundo, CA: Microcosm Press, 2001.

[18] S. W. Shepperd, "Constant Covariance in Local Vertical Coordinates for Near-Circular Orbits," *Journal of Guidance, Control, and Dynamics*, vol. 14, no. 6, pp. 1318–1322, Nov.–Dec. 1991.

[19] R. H. Battin, *An Introduction to the Mathematics and Methods of Astrodynamics*, revised ed. Reston, VA: AIAA, 1999.